Clusters and the Theory of the Cosmic Web

R. van de Weygaert[1] and J. R. Bond[2]

[1] Kapteyn Astronomical Institute, University of Groningen, P.O. Box 800, 9700 AV Groningen, The Netherlands
weygaert@astro.rug.nl
[2] Canadian Institute for Theoretical Astrophysics, University of Toronto, Toronto, ON M5S 3H8, Canada
bond@cita.utoronto.ca

1 Outline: The Cosmic Web

The spatial cosmic matter distribution on scales from a few to more than a hundred Megaparsecs has emerged over the past 30 years through ever more ambitious redshift survey campaigns. From the first hints of superclustering in the seventies to the progressively larger and more detailed three-dimensional maps of interconnected large scale structure that emerged in the eighties, nineties and especially post-2000, we now have a clear paradigm: galaxies and mass exist in a wispy weblike spatial arrangement consisting of dense compact clusters, elongated filaments, and sheetlike walls, amidst large near-empty void regions, with similar patterns existing at higher redshift, albeit over smaller scales. The hierarchical nature of this mass distribution, marked by substructure over a wide range of scales and densities, has been clearly demonstrated. The large scale structure morphology is indeed that of a *Cosmic Web* Bond et al. [18].

Complex macroscopic patterns in nature arise from the action of basic, often even simple, physical forces and processes. In many physical systems, the spatial organization of matter is one of the most readily observable manifestations of the nonlinear collective actions forming and moulding them. The richly structured morphologies are a rich source of information on the physical forces at work and the conditions under which the systems evolved. In many branches of science the study of geometric patterns has therefore developed into a major industry for exploring and uncovering the underlying physics (see e.g., Balbus & Hawley [5]).

The vast Megaparsec cosmic web is one of the most striking examples of complex geometric patterns found in nature, and certainly the largest in terms of sheer size. Computer simulations show the observed cellular patterns can arise naturally through gravitational instability e.g., [62], with the emergent structure growing from tiny density perturbations and the accompanying tiny

R. van de Weygaert and J. R. Bond: *Clusters and the Theory of the Cosmic Web*, Lect. Notes Phys. **740**, 335–407 (2008)
DOI 10.1007/978-1-4020-6941-3_10

velocity perturbations generated in the primordial Universe. Supported by an impressive body of evidence, primarily those of temperature fluctuations in the cosmic microwave background e.g., [9, 45, 78, 79], the character of the primordial random density and velocity perturbation field is that of a *homogeneous and isotropic spatial Gaussian process*. Such fields of primordial Gaussian perturbations in the gravitational potential are a natural product of an early inflationary phase of our Universe.

The early linear phase of pure Gaussian density and velocity perturbations has been understood in great depth. This knowledge has been exploited extensively to extract from CMB data probing the linear regime half a dozen cosmological parameters. Notwithstanding these successes, the more advanced phases of cosmic structure formation are still in need of substantially better understanding. Observables of the mildly nonlinear regime also offer a wealth of information, probing a stage when individually distinct features start to emerge. The anisotropic filamentary and planar structures, the characteristic large underdense void regions and the hierarchical clustering of matter marking the weblike spatial geometry of the Megaparsec matter distribution are typical manifestations of weak to moderate nonlinearity. The existence of the intriguing foamlike network representative of this early nonlinear phase of evolution was revealed by major campaigns to map the galaxy distribution on Megaparsec scales while ever larger computer N-body simulations demonstrated that such matter distributions are indeed typical manifestations of gravitational instability.

The theoretical understanding of the nature of the emergent web is now reasonably well developed, but the development of quantitatively accurate analytic approximations is impeded by the lack of symmetries, strong nonlocal influences, and the hierarchical nature of the gravitational clustering process, with many spatial scales simultaneously relevant. Computer simulations are relied upon to provide the quantitative basis. However, analytic descriptions provide the physical insight into the complex interplay of emerging structures. An area that is still developing is the morphological analysis of the observed and simulated patterns that develop.

This first lecture notes develops the theoretical framework for our understanding of the Cosmic Web. We outline the various formalisms that have been developed to describe the hierarchical nature, the anisotropic geometry of its elements, the intrinsic and intimate relationship with clusters of galaxies, and the predominance of filaments consisting of galaxies, largely in groups, connecting the clusters. Even though we concentrate on the analytical framework, we also describe and illustrate the related generic situations on the basis of computer simulations of cosmic structure formation.

In the accompanying second set of lecture notes (Van de Weygaert & Bond, 2008), we give an overview of Cosmic Web observations. We focus on the morphology of the Cosmic Web and the role of voids within establishing this fundamental aspect of the Megaparsec Universe.

2 Cosmic Structure Formation: From Primordial Quantum Noise to the Cosmic Web

The weakly nonlinear *Cosmic Web* comprises features on scales of tens of Megaparsecs, in which large structures have not lost memory of the nearly homogeneous primordial state from which they formed, and provide a direct link to early Universe physics.

In our exploration of the cosmic web and the development of appropriate tools towards the analysis of its structure, morphology and dynamics we start from the the assumption that the cosmic web is traced by a population of discrete objects, either galaxies in the real observational world or particles in that of computer simulations. Even though individual dynamically relaxed galaxies were the most notable features historically, followed by collapsed clusters, the deepest large potential wells in the universe, we will pursue the view that filaments are basic elements of the cosmic web. Most matter assembles along the filaments, providing channels along which mass is transported towards the highest density knots within the network, the clusters of galaxies. Likewise we will emphasize the crucial role of the voids – the large underdense and expanding regions occupying most of space – in the spatial organization of the various structural elements in the cosmic web. A goal is the construction of the continuous density and velocity fields from the initial condtions, or the reconstruction of these from data, retaining the geometry and morphology of the weblike structures in all its detail.

2.1 Gravitational Instability

In the gravitational instability scenario, e.g., [62], cosmic structure grows from primordial density and velocity perturbations. It has long been assumed that the initial fluctuations were those of a *homogeneous and isotropic spatial Gaussian process*. There is good evidence for this, most notably from the cosmic microwave background. Zero point quantum noise is ubiquitous, and in particular will exist in any fields present in the early universe. In an early period of cosmic acceleration, these fluctuations and the accompanying perturbations in geometrical curvature freeze out as the universe inflates, providing the Gaussian proto-web for growth after matter is created and cosmic deceleration begins. Here we establish the nomenclature and notation for the initial gravitational potential and density fields. For the study of the developing cosmic web at late times, we can ignore relativistic photons and neutrinos, and focus on gas, dark matter and dark energy.

The formation and molding of structure is fully described by three equations, the *continuity equation*, expressing mass conservation, the *Euler equation* for accelerations driven by the gravitational force for dark matter and gas, and pressure forces for the gas, and the *Poisson–Newton equation* relating the gravitational potential to the density.

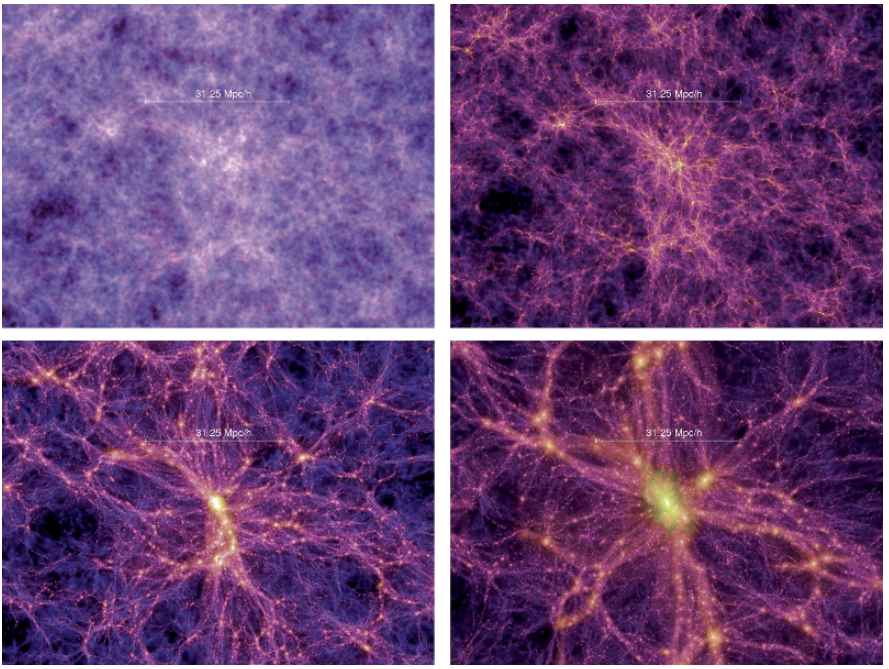

Fig. 1. The Cosmic Web in a box: a set of each four time slices from the Millennium simulation of the ΛCDM model. The frames show the projected (dark) matter distribution in slices of thickness $15\,\mathrm{h}^{-1}\,\mathrm{Mpc}$, extracted at $z = 8.55, z = 5.72, z = 1.39$ and $z = 0$. These redshifts correspond to cosmic times of 600 Myr, 1 Gyr, 4.7 Gyr and 13.6 Gyr after the Big Bang. The set of four frames have a size $31.25\,\mathrm{h}^{-1}\,\mathrm{Mpc}$ zooms in on the central cluster. The evolving mass distribution reveals the major characteristics of gravitational clustering: the formation of an intricate filamentary web, the hierarchical buildup of ever more massive mass concentrations and the evacuation of large underdense voids. Image courtesy of Springel & Virgo consortium, also see Springel et al. [80]

A general density fluctuation field for a component of the universe with respect to its cosmic background mass density $\rho_{\rm u}$ is defined by

$$\delta(\mathbf{r}, t) \;=\; \frac{\rho(\mathbf{r}) - \rho_{\rm u}}{\rho_{\rm u}}\,. \tag{1}$$

Here $\mathbf{r}$ is comoving position, with the average expansion factor $a(t)$ of the universe taken out. Although there are fluctuations in photons, neutrinos, dark energy, etc., we focus here on only those contributions to the mass which can cluster once the relativistic particle contribution has become small, valid for redshifts below 100 or so. A non-zero $\delta(\mathbf{r}, t)$ generates a corresponding total peculiar gravitational acceleration $\mathbf{g}(\mathbf{r})$ which at any cosmic position $\mathbf{r}$ can be written as the integrated effect of the peculiar gravitational attraction exerted by all matter fluctuations throughout the Universe,

$$\mathbf{g}(\mathbf{r},t) \;=\; -4\pi G\bar{\rho}_m(t)a(t)\int \mathrm{d}\mathbf{r}'\,\delta(\mathbf{r}',t)\,\frac{(\mathbf{r}-\mathbf{r}')}{|\mathbf{r}-\mathbf{r}'|^3}\;. \tag{2}$$

Here $\bar{\rho}_m(t)$ is the mean density of the mass in the universe which can cluster (dark matter and baryons). The cosmological density parameter $\Omega_m(t)$ is defined by $\rho_{\rm u}$, via the relation $\Omega_m H^2 = (8\pi G/3)\bar{\rho_m}$ in terms of the Hubble parameter H.[1] The relation between the density field and gravitational potential Φ is established through the Poisson–Newton equation,

$$\nabla^2\Phi = 4\pi G\bar{\rho}_m(t)a(t)^2\;\delta(\mathbf{r},t). \tag{3}$$

The peculiar gravitational acceleration is related to $\Phi(\mathbf{r},t)$ through $\mathbf{g} = -\nabla\Phi/a$.

The gravitational perturbations $\mathbf{g}$ induce corresponding perturbations to the matter flows, best expressed in terms peculiar velocities $\mathbf{v}$ rather than total velocities $\mathbf{u}$ which include the average Hubble expansion:

$$\mathbf{u}(\mathbf{r},t) \;=\; \frac{\mathrm{d}a(t)\mathbf{r}}{\mathrm{d}t} \;=\; H(t)\,a(t)\mathbf{r} \;+\; \mathbf{v}(\mathbf{r},t)\,. \tag{4}$$

The equation of motion for these velocity perturbations from the Hubble expansion is a recasting of the *Euler equation*:

$$\frac{\partial\mathbf{v}}{\partial t} \;+\; \frac{\dot{a}}{a}\mathbf{v} \;+\; \frac{1}{a}\,(\mathbf{v}\cdot\nabla)\mathbf{v} \;=\; -\frac{1}{a}\,\nabla\Phi\,. \tag{5}$$

This is appropriate for a pressureless medium. For gas, an additional $-\frac{1}{\rho a}\,\nabla p$ appears, along with possible viscosity and other gasdynamical forces. The mass conservation is expressed by the *Continuity equation*:

$$\frac{\partial\delta}{\partial t} \;+\; \frac{1}{a}\,\nabla\cdot(1+\delta)\mathbf{v} = 0\,. \tag{6}$$

In slightly overdense regions around density peaks, the excess gravitational attraction slows down the expansion relative to the mean, while underdense regions expand more rapidly. When a positive density fluctuation becomes sufficiently overdense it can come to a halt, turn around and start to contract. As long as pressure forces do not counteract the infall, the overdensity will grow without bound, assembling more and more matter by accretion from the surroundings, ultimately fully collapsing in a gravitationally bound and

[1] There are other contributions to the density, such as relativistic particles and dark energy which either have negligible energy density or do not effectively cluster and so do not contribute to the local peculiar gravitational acceleration, but of course do contribute to the mean acceleration value, $-(4\pi G/3)(\bar{\rho}+3\bar{p})a\mathbf{x}$, where p is the total pressure. It is conventional to parameterize the mean dark energy pressure by $p_{\rm de} = w\rho_{\rm de}$. For the cosmological constant, $w = -1$. Any $w > -1/3$ will give an accelerating term, whereas zero or positive pressure terms appropriate for dark matter and baryons give a deceleration contribution.

virialized object. By contrast the underdense regions around density minima expand relative to the background, forming deep voids. Of course, negative δ's cannot become too negative, constrained to be $\delta > -1$, so the void structure is fundamentally different than the cluster structure.

In this way the primordial overdensity field evolves into the collapsed-peak/void structure we observe, with their precise nature of the collapsed objects, dwarf galaxies, galaxies, groups, clusters, and determined by the scale, mass and surroundings of the initial fluctuation.

2.2 Primordial Origins: Gaussian Noise

There are both physical and statistical arguments in favour of the assumption that the primordial density field in the Universe was a stochastic Gaussian random field. These were applied before the observational evidence emerged for this hypothesis.

For over 25 years, the leading paradigm for explaining the large scale smoothness of the universe has been the inflation hypothesis, in which the very early Universe went through an accelerated expansion driven by an effective scalar field dominating the mass-energy. During an extremely rapid nearly exponential (nearly de Sitter) phase the Universe could have expanded by at least $\sim e^{60}$ within a time measured in Planck time units of 10^{-43} s, the details depending upon the specific particle physics realization of the inflation phenomenon. The inflation ends when preheating occurs, namely when the coherent inflaton field begins to decelerate and can then decay into particles. The density and velocity perturbations that finally evolved into the macroscopic cosmic structures in the observable Universe were generated during this phase as quantum zero point fluctuations in the inflaton, with associated small-amplitude curvature fluctuations since the inflaton carries the dominant source of mass-energy. Most inflation models, even radically different ones, predict similar properties for the fluctuations: adiabatic or curvature, Gaussian and nearly scale-invariant (see Sect. 2.2). The Gaussian nature of the perturbations is a simple consequence of the ground state harmonic oscillator wave function for the fluctuations (the zero point oscillations). Field interactions do generate calculable small deviations from Gaussianity, but except in quite contrived cases these are too tiny to effectively nullify the Gaussian hypothesis. Similarly radical deviations can exist from the simple near-scale-invariance in rather baroque models, but now these are quite constrained by the observation of near-scale-invariance in the cosmic microwave background data.

But even if inflation is not invoked, there was an argument from the *Central Limit Theorem* that Gaussian could still arise if the density field $\delta(\mathbf{x})$ is a superposition of independent stochastic processes, each with their own (non-Gaussian) probability distribution. The Fourier components $\hat{\delta}(\mathbf{k})$ are defined by

$$\delta(\mathbf{x}) \;=\; \int \frac{\mathrm{d}\mathbf{k}}{(2\pi)^3}\; \hat{\delta}(\mathbf{k})\, e^{-i\mathbf{k}\cdot\mathbf{x}}, \tag{7}$$

where $\mathbf{x}$ is comoving position and $\mathbf{k}$ is comoving wavenumber, will be independent, with random phases. There have been models in which Gaussianity does not follow, in situations where the primordial structure is created in phase transitions, e.g. associated with topological entities such as cosmic strings and domain walls.

Gaussian Random Fields

The statistical nature of a random field $f(\mathbf{x})$ is defined by its set of N-point joint probabilities. For a Gaussian random field, this takes the simple form:

$$\mathcal{P}_N \;=\; \frac{\exp\left[-\frac{1}{2}\sum_{i=1}^{N}\sum_{j=1}^{N} f_i\,(\mathsf{M}^{-1})_{ij}\,f_j\right]}{[(2\pi)^N\,(\det \mathsf{M})]^{1/2}} \prod_{i=1}^{N} \mathrm{d}f_i \tag{8}$$

where $\mathcal{P}_N$ is the probability that the field f has values in the range $f(\mathbf{x}_j)$ to $f(\mathbf{x}_j) + \mathrm{d}f(\mathbf{x}_j)$ for each of the $j = 1, \ldots, N$ (with N an arbitrary integer and $\mathbf{x}_1, \mathbf{x}_2, \ldots, \mathbf{x}_N$ arbitrary locations in the field). (We have assumed zero mean in this expression, as would be the case for $\delta, \mathbf{g}$ and $\mathbf{v}$.)

The matrix M^{-1} is the inverse of the $N \times N$ covariance matrix M,

$$M_{ij} \;\equiv\; \langle f(\mathbf{x}_i) f(\mathbf{x}_j)\rangle \;=\; \xi(\mathbf{x}_i - \mathbf{x}_j)\;, \tag{9}$$

in which the brackets $\langle \ldots \rangle$ denote an ensemble average over the probability distribution. In effect, M is the generalization of the variance σ^2 in a one-dimensional normal distribution. The equation above shows that a Gaussian distribution is fully specified by the matrix M, whose elements consist of specific values of the autocorrelation function $\xi(r)$, the Fourier transform of the power spectrum $P_f(k)$ of the fluctuations $f(\mathbf{r})$,

$$\xi(\mathbf{r}) \;=\; \xi(|\mathbf{r}|) \;=\; \int \frac{\mathrm{d}\mathbf{k}}{(2\pi)^3}\; P_f(k) \mathrm{e}^{-\mathrm{i}\mathbf{k}\cdot\mathbf{r}}\,. \tag{10}$$

Notice that the identity of $\xi(\mathbf{r})$ and $\xi(|\mathbf{r}|)$ is assumed, not required. A homogeneous and isotropic Gaussian random field f is statistically fully characterized by the power spectrum $P_f(k)$.

Power Spectrum of Density Fluctuations

The main agent for formation of structure in the Universe is a gravitationally dominant dark matter constituent of the Universe. Within the currently most viable cosmology, often called *Concordance Cosmology*, the dark matter is taken to be Cold Dark Matter: a species of non-baryonic, dissipationless

and collisionless matter whose thermal properties are marked by their non-relativistic peculiar velocity (cold) at the time of radiation-matter equality. The popular candidate for this, for which a number of ambitious experiments in deep mines are in place to directly detect it through its very weak non-gravitational interactions, is the lightest supersymmetric partner of ordinary fermions, e.g. the neutralino, a scalar field partner of the neutrino, the photino, the fermionic partner of the photon, or some linear combination of other partners.

The primordial spectrum $P_p(k)$ of density perturbations in the CDM spectrum directly follows from the post-inflation form of the graviational potential fluctuations through the Poisson–Newton relation, $\delta_\rho(k) = -k^2\Phi(k)/(4\pi G\bar{\rho}a^2)$. Scale-invariant means that there is equal power per decade in the gravitational potential fluctuations, $\langle|\Phi(k)|^2\rangle d^3k/(2\pi)^3 \sim k^{n-1}d\ln k$ is $\propto d\ln k$, where n is a power law index measuring deviation from the scale-invariant unity. The corresponding form for the initial density power spectrum is $P^i_\rho(k) \equiv \langle|\delta(k)|^2\rangle \propto k^n$. Current CMB data supports an index n close to the scale-invariant unity, but slightly deviating from it, $n \approx 0.96 \pm 0.02$ Kuo et al. [45] and Spergel et al. [79]. This nearly scale invariant nature is a natural outcome of large classes of inflationary models. The expectation is that there are at least logarithmic deviations from s constant n, and it possible to get more radical deviations, as expressed by the running of the index, $\mathrm{d}n/d\ln k \neq 0$. (There are hints of running from CMB observations, -0.06 ± 0.03 without gravity wave perturbations Kuo et al. [45], -0.04 ± 0.03 with them included Bond et al. [20].) Even before inflation theory or the data focussed attention on n nearly one, the scale-invariance was considered a natural property to assume to avoid a power spectrum with large rises either at large wavenumbers ($n > 1$) or small wavenumbers ($n > 1$), since δ could otherwise exceed unity and nonlinear collapsed structures (e.g. primordial black holes) could form in the ultra-early universe. Thus $n = 1$ was recognized as a possibility from the early seventies, defining the Harrison–Zel'dovich–Peebles spectrum.

During acceleration Ha increases and what has often been called the instantaneous horizon over which signals can propagate in a Hubble time, $(Ha)^{-1}$ decreases, and wave structure with $k/Ha < 1$ can no longer communicate, the fluctuations freeze out at their inflationary values. Once preheating occurs and radiation and matter some to dominate the energy density, the universe decelerates, Ha decreases and frozen-in perturbation patterns can respond to forces associated with their gradients once k goes above Ha. The combination of gravity and the opposing radiation pressure cause these sub-horizon fluctuations in radiation and baryon density to respond as sound waves. Meanwhile, positive fluctuations in the cold dark matter have no pressure forces and can grow, however they must do so in an expanding environment dominated by radiation which impedes the rate of growth of δ (called Hubble drag). It is only after the dynamics of cosmic expansion becomes dominated by matter following the *matter-radiation equality*, at $z_{\rm eq} \approx 3450$, when CDM density perturbations can grow rapidly, impeded only by its own Hubble

drag to grow at a power law rate $\propto t^{2/3}$ rather than exponentially. The evolutionary history of fluctuations of a wavenumber k then depends upon whether k exceeds Ha in the radiation or matter dominated phase. This is encapsulated in the power spectrum transfer function $T(k)$, defined by the deviation from the primordial power spectrum shape, $P_{\rm CDM}(k) \propto k^n T^2(k)$. Corresponding to the redshift $z_{\rm eq}$ is a characteristic wavenumber scale, $k_{\rm Heq} = Ha(z_{\rm eq})$. For a CDM model with vary small baryon content, the transfer function is a unique function of $k/k_{\rm Heq}$.

From the early 1980s, much effort has gone into computing the transfer functions in terms of the material content of the universe, varying amounts of dark matter, massive neutrinos, baryons, relativistic matter, dark energy, etc. An example of a much-used numerical fitting formula for the CDM class of models which is accurate for low baryon density parameters Ω_b is that given by Bardeen et al. [6],

$$P_{\rm CDM}(k) \propto \frac{k^n}{[1+3.89q+(16.1q)^2+(5.46q)^3+(6.71q)^4]^{1/2}} \times \frac{[\ln(1+2.34q)]^2}{(2.34q)^2}\,,$$

$$q = k/\Gamma\,, \quad \Gamma = \Omega_{m,0} h \exp\left\{-\Omega_b - \frac{\Omega_b}{\Omega_{m,0}}\right\}$$

where $k = 2\pi/\lambda$ is the wavenumber in units of $\mathrm{h\,Mpc^{-1}}$ and Γ the shape parameter. It is indeed a function of $k/k_{\rm Heq}$, with $k_{\rm Heq} \sim 5\Gamma \mathrm{h\,Mpc^{-1}}$ in the $\Omega_b \to 0$ limit. The Ω_b dependencs approximately accounts for the effect of baryons in the transfer function Sugiyama [81], although superposed upon such a T is an oscillation associated with the acoustic oscillations that the baryon-photon fluid participates in, unlike the CDM.

The corresponding *effective* power spectrum slope $n_{\rm eff}(k)$ of the Cold Dark Matter spectrum,

$$n_{\rm eff}(k) \equiv \frac{d\ln P(k)}{d\ln k} \tag{11}$$

drops from the primordial value value $n_{\rm eff} = n$ in the large scale limit $k \downarrow 0$ to $n_{\rm eff} \approx= -3 + (n-1)$ modulo logarithmic corrections at high $k \to \infty$, a direct consequence of the large Hubble drag from radiation, hence slow growth that the high k fluctuations experience. The density power spectrum per e-folding in wavenumber is

$$\mathcal{P}_\rho(k) = \mathrm{d}\sigma_\rho^2/d\ln k \equiv \langle|\delta(k)|^2\rangle k^3/(2\pi^2) \propto k^{n+3}\,.$$

The power progressively drops from small scales to large, defining the hierarchical nature of the power spectrum. (The integrated *rms* density fluctuations up to scale k, $\sigma_\rho(k)$, implicitly defined by (12) is by definition monotonic.)

2.3 Structure Growth

The time evolution of the density perturbation field $\delta(\mathbf{x}, t)$ can be inferred from the solution to the three fluid equations. Generally, $|\delta|$ grows with time.

When a cosmic structure reaches virial equilibrium, as in galaxies or clusters, the physical density is constant, but the overdensity relative to the declining $\bar{\rho}_{\rm CDM} \propto a^{-3}$ background still rises. Once the radiation energy density falls off after $z_{\rm eq}$, there is still a long period of growth in the linear regime, defined by density perturbations with $\delta \ll 1$ and velocity perturbations with $(vt_{\rm exp}/d)^2 \ll 1$ (with d the coherence length of the perturbation). For the early phases of growth, it is useful to expand the perturbations in spatial eigenmodes of our three evolution equations. These are simply plane waves, and the Fourier-transformed equations depend only upon k for small δ (mode–mode $k - k'$ couplings occur through the nonlinear $\delta\mathbf{v}$ and $\mathbf{v}\cdot\nabla\mathbf{v}$ terms). The three evolution equations reduce to a single *linearized equation for the growth of density perturbations* $\delta(\mathbf{x}, t)$ e.g.,

$$\frac{\partial^2\delta}{\partial t^2} \,+\, 2\frac{\dot{a}}{a}\,\frac{\partial\delta}{\partial t} \;=\; \frac{3}{2}\Omega_{m0}H_0^2\,\frac{1}{a^3}\,\delta \tag{12}$$

The general solution to this second order partial differential equation is the sum of a universal growing mode solution $D_1(t)$ and a a decaying mode solution $D_2(t)$,

$$\delta(\mathbf{x}, t) \;=\; D_1(t)\,\Delta_1(\mathbf{x}) \,+\, D_2(t)\,\Delta_2(\mathbf{x}) \tag{13}$$

Because the decaying mode is quickly rendered insignificant in comparison to the growing mode for practical purposes it is usually sufficient to concentrate solely on the growing mode solution.

The density growth factor $D(t)$ is dependent upon the cosmological background: in different FRW Universes the growth of structure will proceed differently. In a matter-dominated FRW Universe $D(t)$ can be solved fully analytically, for more general situations the linear growth factor needs to be evaluated numerically. Ignoring the contribution by radiation, the *linear growth factor* $D(t)$ in a Friedmann-Robertson-Walker Universe containing only matter and a cosmological constant Λ (or equivalent dark energy component), with current density parameters $\Omega_{m,0}$ and $\Omega_{\Lambda,0}$, may be computed from the integral (see Heath [33], Peebles [62], Hamilton [32], Lahav & Suto [49])

$$D(t) \;=\; D(t, \Omega_{m,0}, \Omega_{\Lambda,0}) \;=\; \frac{5\,\Omega_{m,0}H_0^2}{2}\,H(a)\int_0^a \frac{{\rm d}a'}{a'^3H^3(a')}\,, \tag{14}$$

where the linear density growth factor is normalized to unity at the present epoch, $D(t_0) = 1$. For pure matter-dominated Universes, $\Omega_\Lambda = 0$, one may derive analytical expressions for $D(t)$ (see Peebles [62]). For $\Omega_m = 1$ and no mean curvature, $D = a$. For the general situation including a non-zero cosmological constant, $\Omega_\Lambda \neq 0$, the following fitting formula provides a sufficiently accurate approximation for most purposes [49],

$$D(t) \approx a(t)\,\frac{5\Omega(t)}{2}\,\frac{1}{\Omega(t)^{4/7} - \Omega_\Lambda(t) + [1+\Omega_m(t)/2][1+\Omega_\Lambda(t)/70]}\,, \quad (15)$$

in which $\Omega(t) = \Omega_m(t) + \Omega_\Lambda(t)$.

The accompanying growing mode linear velocity perturbations $\mathbf{v}(t)$ are linearly proportional to the generating peculiar gravitational acceleration $\mathbf{g}(t)$,

$$\mathbf{v} = \frac{2\,f}{3H\Omega}\,\mathbf{g}\,.$$

The deviation from Einstein de Sitter $D = a$ growth is described by the *dimensionless linear velocity growth factor* $f = f(\Omega_m, \Omega_\Lambda)$ encoding how D runs with respect to a:

$$\begin{aligned} f(\Omega_m, \Omega_\Lambda) &\equiv \frac{a}{D}\frac{\mathrm{d}D}{\mathrm{d}a} \\ &= -1 - \frac{\Omega_m}{2} + \Omega_\Lambda + \frac{5\Omega_m}{2}\frac{a}{D}\,, \end{aligned} \quad (16)$$

with the implied growth $D_v(t)$ of linear velocity perturbations given by

$$D_v(t) = a\,D\,H\,f(\Omega_m, \Omega_\Lambda)\,. \quad (17)$$

For a matter-dominated Universe with $\Omega_m \lesssim 1$ Peebles [62] found the famous approximation,

$$f(\Omega_m) \approx \Omega_m^{0.6}\,. \quad (18)$$

An extension of this approximation for a Universe with both matter and a cosmological constant Λ was given by Lahav et al. [48],

$$f(\Omega_m, \Omega_\Lambda) \approx \Omega_m^{0.6} + \frac{\Omega_\Lambda}{70}\left(1 + \frac{\Omega_m}{2}\right) \quad (19)$$

This form clearly shows that the velocity growth being is mainly determined by the matter density Ω_m and is only (very) weakly dependent on the cosmological constant. The latter is to be expected since perturbations in dark energy are expected to damp when k exceeds Ha rather than grow.

Current estimates of the material content of the Universe for tilted ΛCDM models from CMB and large scale structure data are $\Omega_{m,0} \approx 0.27 \pm 0.03$, $\Omega_{\Lambda,0} \approx 0.73 \pm 0.03$ and $\Omega_b \sim 0.045$ [45]. The dark matter to baryon ratio is ~ 5, small enough for acoustic oscillations to be evident in the transfer function, and this effect has now been observed in galaxy redshift surveys. At early times any matter-dominated FRW Universe evolves as the expansion factor $a(t)$, $D(t) = a(t) \propto t^{2/3}$, as in an Einstein-de Sitter Universe (defined by $\Omega_m(a) = \Omega_{m,0} = 1$, $\Omega_\Lambda = 0$).

In the Λ-dominated cosmology favored by current cosmological observations, the universe makes the transition from deceleration to acceleration at

$$a_{m\Lambda} \approx \left(\frac{\Omega_{m,0}}{2\Omega_{\Lambda,0}}\right)^{1/3} . \tag{20}$$

The vacuum energy density associated with the cosmological constant dominates over the mass density of matter at $2^{1/3}a_{m\Lambda}$, hence the Hubble parameter is Λ-dominated and Hubble drag slows the subsequent growth of fluctuations. With $\Omega_{m,0} \approx 0.27$ and $\Omega_{\Lambda,0} \approx 0.73$, this gives $z_{m\Lambda} \approx 0.7$. This freezing out of growth occurs for linear structures on large scales. In nonlinear high-density regions, the local gravity is strong enough for the evolution of structure to continue. As a result, no larger scale weblike patterns will emerge after the Universe gets into exponential expansion, yet within the confines of the existing Cosmic Web structures and objects will continue to evolve as clumps of matter collapse and merge into ever more pronounced and compact halos and features (see Sect. 2.4).

A nice illustration of the evolution is in Fig. 2, showing how the large scale Universe changes in a ΛCDM model from $z = 8$ until the present-day, in a box of size $65\,\mathrm{h}^{-1}$ Mpc. The time proceeds along the length of the two strips, the lateral direction is taken along the length of the box. The developing structure along the two strips shows the emergence of the Megaparsec Cosmic Web out of the nearly uniform and early Universe. Along the lefthand frame time runs from $z \approx 8$ (bottom) until (top) and in the righthand frame from $z \approx 4$ at the bottom to the present-day at $z = 0$ (upper righthand frame).

The cosmic mass distribution is marked by cellular patterns whose characteristic size grows is continuously growing and becomes ever more pronounced up to $z \approx 1.5 - 2$ (centre righthand frame). Clearly recognizable, particular in the lefthand frame, is the hierarchical buildup of the weblike patterns. Both filaments and voids are seen to merge with surrounding peers into ever larger specimen of these features.

Later, as a consequence of the accelerated expansion of the Universe the large scale structure begins to slow at $z \approx 1.5 - 2.0$. As a result the overall spatial distribution of matter remains basically unchanged. Within the existing structures the nonlinear evolution does indeed continue: filaments and clusters remain overdense regions in which gravity continues to mould the clustering and configuration of matter. It results in a continuing sharpening of the weblike features in the Megaparsec universe.

2.4 Nonlinear Clustering

Once the gravitational clustering process has progressed beyond the initial linear growth phase we see the emergence of complex patterns and structures in the density field. Highly illustrative of the intricacies of the structure formation process is that of the state-of-the-art N-body computer simulation,

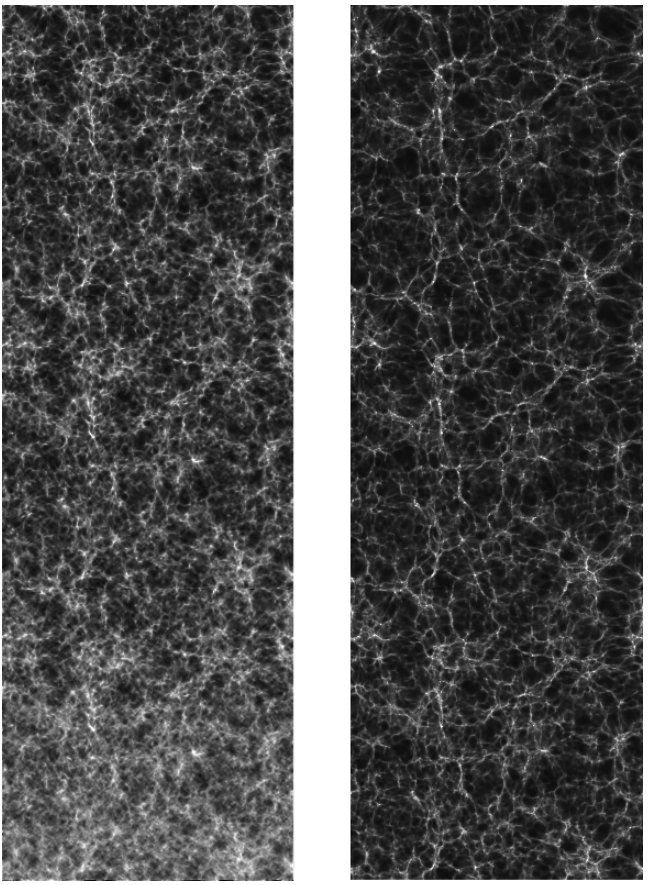

Fig. 2. The development of the large scale Universe from $z = 8$, after the end of the Dark Ages, until the present-day in a timeline proceeding along two strips. The timeline runs from lower lefthand frame (end Dark Ages, $z = 8$) until $z \approx 4$ (*top of lefthand frame*), resuming the latter at the bottom of the righthand frame and running on to the present-day at $z = 0$ at the upper righthand of that frame. The cosmic mass distribution is marked by cellular patterns whose characteristic size grows continuously and becomes ever more pronounced up to $z \approx 1.5 - 2$ (*centre righthand frame*). As a consequence of the accelerated expansion of the Universe the large scale structure freezes at that point: the overall distribution of matter remains basically unchanged, except for the sharpening of the features as a result of the continuing nonlinear evolution within these features. Image courtesy of Aragón-Calvo, also see Aragón-Calvo [1]

the Millennium simulation by Springel et al. [80]. Figure 1 shows two sets of each four time frames out of this massive 10^{10} particle simulation of a ΛCDM matter distribution in a $500\,\mathrm{h}^{-1}\,\mathrm{Mpc}$ box. The time frames correspond to redshifts $z = 8.55$, $z = 5.72$, $z = 1.39$ and $z = 0$ (i.e. at epochs 600 Myr, 1 Gyr,

4.7 Gyr and 13.6 Gyr after the Big Bang). The earliest time frame is close to the epoch when the first dwarf galaxies formed. Current estimates show that the characteristic redshift for reionization of the gaseous IGM by radiation from the first stars, when the so-called *Dark Ages* ended, is at $z_{reh} = 11.4 \pm 2.5$ [45]. (Even with 10 billion particles, the web-like structure that actually exists at $z = 8.55$ is not evident since the waves that have formed it cannot be included in such a simulation.) The first set of frames contains the Dark Matter particle distribution in a $15\,\mathrm{h}^{-1}\,\mathrm{Mpc}$ thick slice of a $125\,\mathrm{h}^{-1}\,\mathrm{Mpc}$ region centered on the central massive cluster of the simulation. The second set zooms and illuminates the details of the emergence of the central cluster in a $31.25\,\mathrm{h}^{-1}\,\mathrm{Mpc}$ sized region.

The first set provides a beautiful picture of the unfolding Cosmic Web, starting from a field of mildly undulating density fluctations towards that of a pronounced and intricate filigree of filamentary features, dented by dense compact clumps at the nodes of the network. The second set of frames depict the evolution of the matter distribution surrounding the central highly dense and compact cluster. In meticulous detail it shows the formation of the filamentary network connecting into the cluster which are the transport channels for matter to flow into the cluster. Clearly visible as well is the hierarchical nature in which not only the cluster builds up but also the filamentary network. At first consisting of a multitude of small scale edges, they quickly merge into a few massive elongated channels. Equally interesting to see is the fact that the dark matter distribution is far from homogeneous: a myriad of tiny dense clumps indicate the presence of the dark halos in which galaxies – or groups of galaxies – will or have formed.

Large N-body simulations like the Millennium simulation and the many others currently available all reveal a few "universal" characteristics of the (mildly) nonlinear cosmic matter distribution. Three key characteristics of the Megaparsec universe stand out:

- Hierarchical clustering
- Anisotropic & Weblike spatial geometry
- Voids

These basic elements exist at all redshifts, but differ in scale, in fact with a growing *nonlinear wavenumber* $k_{NL}(z)$ characterizing the onset of moderate nonlinearity. The linearly-evolving integrated power spectrum defined by (12), $\sigma^2_{\rho L}(k,z) = D^2(z)\sigma^2_{\rho L}(k,0)$ as a function of redshift. If linear growth were to prevail, formal nonlinearity would occur when $\delta(k,z) \sim 1$, namely at $k = k_{NL}(z)$, where $\sigma_{\rho L}(k_{NL}(z),0) \equiv D^{-1}(z)$. Monotonicity of $\sigma_{\rho L}$ guarantees $k_{NL}(z)$ increases with decreasing redshift. The cosmic web pattern is developed from waves in a band of wavenumbers just below $k_{NL}(z)$, hence the web-like patterns seen in simulations look somewhat similar at differing redshifts, except the overall scale changes with increasing k_{NL}. (The relevant

web-band in $\sigma_{\rho L}$ for the weak to moderate nonlinearity relevant to the web pattern turns out to be about 0.2–0.7 [18, 19], with higher values associated with collapsed density peaks). Because $\Delta\sigma_{\rho L}/\sigma_{\rho L} \propto (n_{\rm eff}+3)\Delta \ln k$ in terms of the effective index of the power spectrum $n_{\rm eff}$, the wavenumber band $\Delta \ln k$ associated with $\sigma_{\rho L}/\sigma_{\rho L} \approx 1/2$ is considerably wider for the flattened spectra associated with higher redshif: that is more waves belong to the web-band around k_{NL}, and the filaments tend to be fatter (more ribbon-like) than at lower redshift [19].

The challenge for any viable analysis tool is to trace, highlight and measure each of the morphological elements of the cosmic web. Ideally it should be able to do so without resorting to user-defined parameters or functions, and without affecting any of the other essential characteristics.

3 Hierarchical Structure Formation

In a simple Einstein-deSitter models of spherical overdense perturbations, when the linear $\delta_L = 1.05$, the flow changes from outward, albeit increasingly lagging the cosmic Hubble flow, to infall, toward complete collapse and virialization by $\delta_L = f_c \approx 1.7$. If so, a typical 2-sigma density peak associated with a scale k will collapsed at $\sigma_{\rho L} \approx f_c/2 \sim 0.8$, the (much) rarer 3-sigma density peaks at $\sigma_{\rho L} \approx 0.6$, hence the collapsed structure band is associated with $\sigma_{\rho L} \gtrsim 0.7$ which defined the upper bound of the web pattern $\sigma_{\rho L}$ described in the last section. A rough relation of characteristic wave number to mass of the collapsed object is $M = (4\pi/3)\bar{\rho}_{\rm m}(2a/k)^3 \approx 10^{12}\Omega_{\rm m}(2k^{-1}/{\rm Mpc})^3\,{\rm M}_\odot$ [17].

Thus, as k_{NL} sweeps down from high redshift, it leaves in its wake first stars which reionize the universe formed in tiny dwarf galaxies with $2k^{-1} \sim 10\,{\rm kpc}$, dwarf galaxies with $2k^{-1} \sim 100\,{\rm kpc}$, large Milky Way like galaxies with $2k^{-1} \sim$ Mpc to rare large clusters with $2k^{-1} \sim 10\,{\rm Mpc}$. The web associated with sligthly lower k's is formed from the front end of the k_{NL}-wake. These features of (zero-dimension) objects embedded in structures of a larger dimension (one-dimensional filaments, two-dimensional sheets) at a lower density is clearly evident in Fig. 3, with the larger encompassing perturbations gradually evolving through the merging and accretion of smaller scale clumps, a process illustrated in Fig. 4.

Aptly described by the concept of *merger tree* (see e.g., Kauffmann & White [42], Lacey & Cole [46]), the precise path that an encompassing perturbation follows towards final collapse and virialization may be highly diverse.

3.1 Hierarchical Structures

Extended features still in the process of collapsing, or collapsed objects which have not yet fully virialized, often contain a large amount of smaller scale substructure at higher density which materialized at an earlier epoch. This

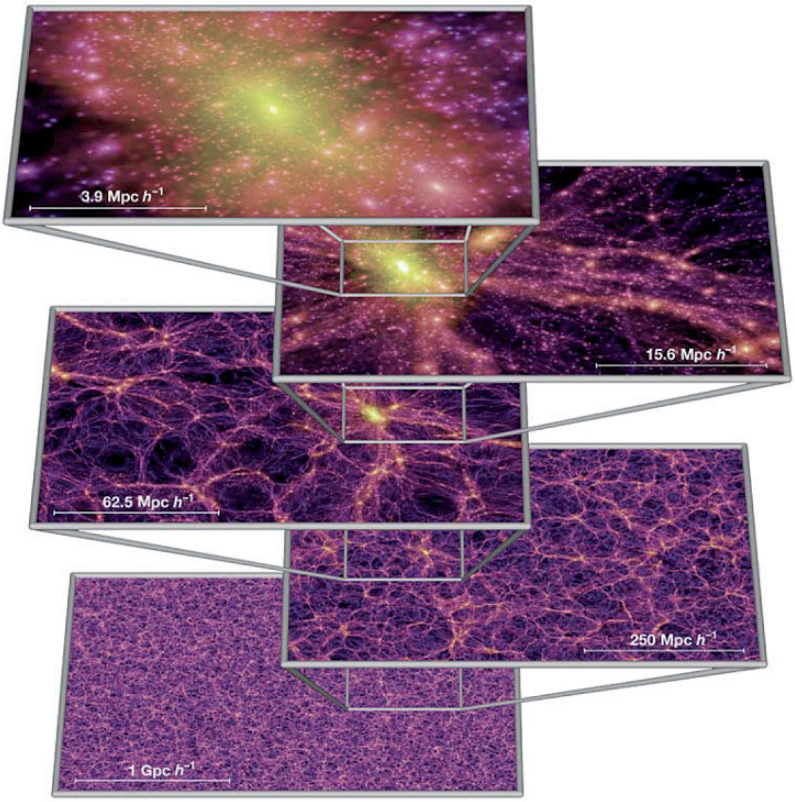

Fig. 3. The hierarchical Cosmic Web: over a wide range of spatial and mass scales structures and features are embedded within structures of a larger effective dimension and a lower density. The image shows how structures in the Millennium simulation are mutually related: at five successive zooms it focusses on a very dense and compact massive cluster at the intersection of a high number of filamentary extensions. Image courtesy of Springel & Virgo consortium, also see Springel et al. [80]. Reproduced with permission of Nature

substructure is a clear manifestation of the hierarchical development of structure in the Universe. This hierarchy of embedded structures is illustrated in Fig. 3, which shows five slices through the Millennium simulation [80], from bottom to top representing successive zoom-ins onto a very dense and compact massive cluster.

Observationally we can recognize traces of the hierarchical formation process in the galaxy distribution on Megaparsec scales. The large unrelaxed filamentary and wall-like superclusters contain various rich clusters of galaxies as well as a plethora of smaller galaxy groups, each of which has a higher density than the average supercluster density. Zooming in on even smaller

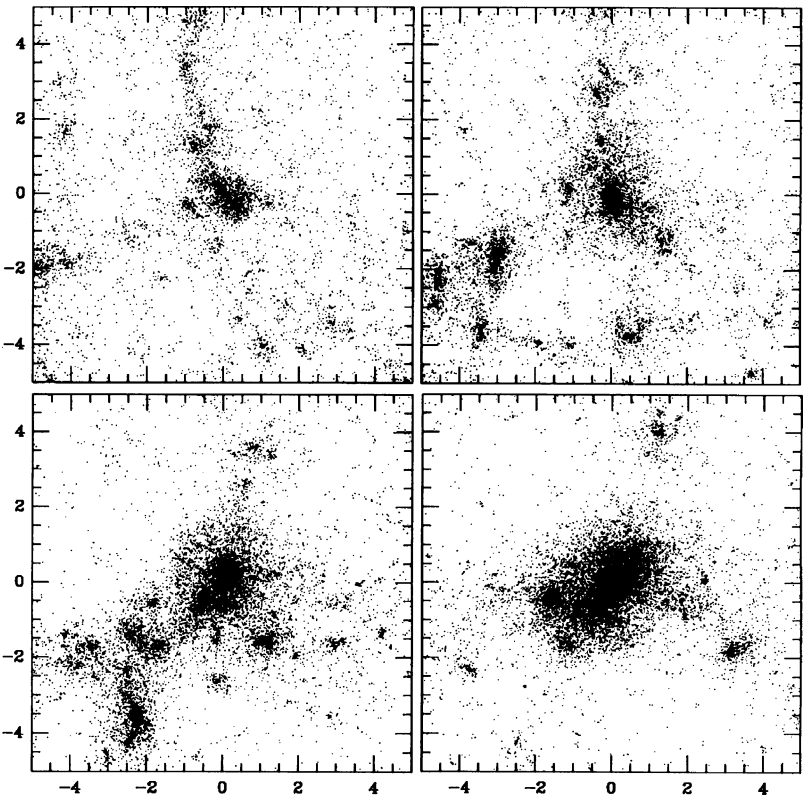

Fig. 4. Illustration of the hierarchical formation of a cluster sized halo. From: van Haarlem & van de Weygaert [83]. Reproduced by permission of the AAS

scales, within groups large galaxies themselves are usually accompanied by a number of smaller satellites and dwarf galaxies. The imprint of hierarchical clustering may also be found in fully collapsed structures, such as clusters and even the halos of galaxies. Even when studying the hot X-ray emitting intracluster gas, more evenly distributed than the galaxies, the majority of clusters appears to display some measure of substructure (e.g. Schücker et al. [71]). Even the Coma cluster appears to be marked by a heavy infalling group [59]. Also galaxies bear the marks of their hierarchical formation. The most visible manifestation concerns the presence of streams in their dark halos, remnants of infalling dwarf galaxies (e.g. Helmi & White [34], Freeman & Bland-Hawthorn [29]).

3.2 Mass Scale Fluctuations

We now generalize the integrated *rms* power $\sigma_{\rho L}(k, z)$ to *rms* fluctuations associated with general filters $W(kR)$ [6]:

$$\sigma_W^2(R) \;=\; \int d\ln k\; |\hat{W}(kR)|^2\; d\sigma_{\rho L}^2(k)/d\ln k\,. \tag{21}$$

For example, if the density field is smoothed with a tophat or Gaussian filter, then $\hat{W}(x)$ is

$$\hat{W}(\mathbf{x}) \quad \rightarrow \quad \begin{cases} \hat{W}_{\rm TH} = \;\; \dfrac{3}{x^3}\,(\sin x - x\cos x) & \text{Tophat} \\ \hat{W}_{\rm G} \;= \exp(-x^2/2) & \text{Gaussian} \end{cases}$$

respectively. The Fourier transforms of the filters define smoothing functions W in real space,

$$\begin{cases} W_{\rm TH}(\mathbf{r}) \;=\; \vartheta(R_{\rm TH}-r)/V_{\rm TH}\,, & V_{\rm TH} = 4\pi R^3/3 \\ \\ W_{\rm G}(\mathbf{r}) \;=\; \exp(-r^2/2R_{\rm G}^2)/V_{\rm G}\,, & V_{\rm G} = (2\pi)^{3/2}R^3 \end{cases}$$

Here, $\vartheta(x)$ is the Heaviside function, unity if $x \geq 0$ zero if $x < 0$. The smoothing filter that defines $\sigma_{\rho L}^2(k_R)$ is called the "sharp k-space" filter, simply a top hat in k-space, $\hat{W} = \vartheta(1 - kR_k)$, where $R_k = 1/k_R$. Its Fourier transform is $W(\mathbf{r}) = \hat{W}_{\rm TH}(rk_R)/V_{\rm k}$, with $V_{\rm k} = (4\pi/3)k_R^{-3}/(2\pi)^3$.

The nature of top hat smoothing is clear: around each point $\mathbf{r}$, we volume-average the field over a spherical region of radius R around it. There is a clear mass assignment we can make, $M_{\rm TH} = \bar{\rho}_m a^3 V_{\rm TH}$. For the other filters, the relation between the scale R and an appropriate mass is trickier. The obvious values, $\bar{\rho}_m a^3 V_{\rm G}$ and $\bar{\rho}_m a^3 V_{\rm k}$ turn out not to be applicable to objects.

From the discussion about the nonlinear wavenumber above, it should be clear that $\sigma_{\rho L}(k)$ defines a clock whose ticks march out the development of the hierarchy. Indeed Bond et al. [16] showed that the square,

$$S \;\equiv\; \sigma_{\rho L}^2 \tag{22}$$

is the most appropriate. A convenient way to define a filter-independent mass is to determine the "trajectory" $R_{\rm TH}(S)$ by inverting $S = \sigma_{\rm TH}^2(R_{\rm TH})$ and using $M_{\rm TH}$ for every filter. The trajectories $R_{\rm k}(S)$ and $R_{\rm G}(S)$ then define functional relations $R_{\rm k}(M_{\rm TH})$ and $R_{\rm G}(M_{\rm TH})$ among filter scales. There are more sophisticated ways of defining the mass relations among filters using profiles around density field peaks, but this approach gives similar answers. It turns out that the inversion for Gaussian and sharp-k space gives $R_{\rm TH}/R_{\rm G} \approx 2$, with a similar result $R_{\rm TH}/R \approx 2$.

3.3 Collapse and Virialization: Density Barriers

The correspondence between mass and filter scale, $M \propto R^3$, suggests that if one wishes to model (proto)objects of mass M one should study the initial

density fluctuation field when it is smoothed on (comoving) spatial scale $R \propto M^{1/3}$, with the exact coefficient depending on filter choice (22):

$$\delta(\mathbf{r}, t|R) \;=\; \int \mathrm{d}\mathbf{r}'\, \delta(\mathbf{r}', t)\, W((\mathbf{r} - \mathbf{r}')/R)\,. \tag{23}$$

For the pure power-law spectra $P(k) \;\propto k^{n_{\rm eff}}$ the fluctuations S on a mass scale M scale as

$$S(M) \propto \; M^{-(n_{\rm eff}+3)/3}\;. \tag{24}$$

The monotonocity of $S(M)$ with M is generally valid, even with the $n_{\rm eff}(k)$ we have seen arise in ΛCDM and other theories. The Cold Dark Matter spectrum (11) has $n_{\rm eff}(k_{\rm gal}) \approx -2$ on galaxy scales and $n_{\rm eff}(k_{\rm cls}) \approx -1.3$ on clusters scales.

Spherical Haloes: Collapse & Virialization

We now review the extremely instructive nonlinear evolution of a spherically symmetric density peak, which turns around and collapses, with complete collapse to a point predicted to occur when the linearly-extrapolated (primordial) density, $\delta_L(r, t|R) \;=\; D(t)/D(t_i)\delta_L(r, t_i|R)$ (12, 13), reaches a critical density excess f_c [30]. No singularity in fact develops, rather shells of mass pass through the origin and oscillate relative to each other finally settling down to a virial equilibrium in which kinetic and gravitational forces are balanced. In more realistic 3D collapses the inevitable non-spherical perturbations enhance the approach to virialization. Thus we can identify smoothed linear overdensities f_{ta}, f_{vir} as well as f_c, as well their nonlinear overdensity counterparts, $\delta_{NL,ta}$, $\delta_{NL,vir}$ as well as $\delta_{NL,c} = \infty$: The collapse and subsequent virialization of a spherical and isolated overdensity is solely dependent on such a critical – and universal – threshold level f_c, and independent of the mass scale M. The same holds true for its decoupling from the Hubble expansion and turnaround. The corresponding characteristic density thresholds for turnaround f_{ta}, collapse f_c and virialization f_{vir} can be derived from the spherical model.

The critical value for an Einstein-de Sitter $\Omega_m = 1$ Universe has the well-known value derived by Gunn & Gott [30],

$$f_c \;=\; \frac{3}{20}\,(12\pi)^{2/3} \;\simeq\; 1.686\,, \tag{25}$$

while the corresponding critical nonlinear virialization value is given by

$$\frac{\rho_{vir}}{\rho_u} \;=\; 18\pi^2 \;\simeq\; 178.0\,. \tag{26}$$

Similar values can be easily derived for turnaround: the linear turnaround threshold value $f_{\rm ta} = 1.08$, while the nonlinear turnaround density values is $\delta_{NL,ta} = 5.55$.

For a general FRW Universe with $\Omega_{m,0} \neq 1$ and/or $\Omega_{\Lambda,0} \neq 0$ the values depend upon the cosmic epoch at which turnaround, collapse or virialization of the density perturbation takes place, i.e., it is a function of the values of Ω_m and Ω_Λ at the corresponding cosmic epoch. For open cosmologies with $\Lambda = 0$ solutions to the problem were computed by Lacey & Cole [46]. Lahave et al. [48] adressed the issue for FRW universes with a cosmological constant $\Lambda \neq 0$, while Eke et al. [27] computed the explicit solutions for flat $\Omega_m + \Omega_\Lambda = 1$ FRW universes. The general expressions for these situations were summarized by Kitayama & Suto [43]. The case for Dark Energy models with $w \neq -1$ were assessed by Percival (2005). While the linear collapse threshold value f_c does depend somewhat on the cosmological background, the values for plausible cosmologies are only marginally different from those for an Einstein-de Sitter Universe. As may be seen in Fig. 5 the values for f_c in generic-open matter-dominated cosmologies or flat cosmologies with a cosmological constant Λ turn out to have only a weak dependence on $\Omega_{m,0}$: in an open $\Omega_{m,0} = 0.1$ Universe $f_{c,0} \approx 1.615$. We note that the nonlinear virialization threshold $\delta_{NL,vir}$ displays a considerably stronger variation as a function of cosmology.

Useful fitting formulae for the linear spherical model collapse value $\delta_{NL,c}$ were obtained by Bryan & Norman [22] for $\Omega_\Lambda = 0$ FRW universes and for flat Universes:

$$\begin{cases} \delta_{NL,c} = 18\pi^2 + 82(\Omega_m - 1) - 39(\Omega_m - 1)^2 & \Omega_m + \Omega_\Lambda = 1 \\ \delta_{NL,c} = 18\pi^2 + 60(\Omega_m - 1) - 32(\Omega_m - 1)^2 & \Omega_\Lambda = 0 \end{cases} \tag{27}$$

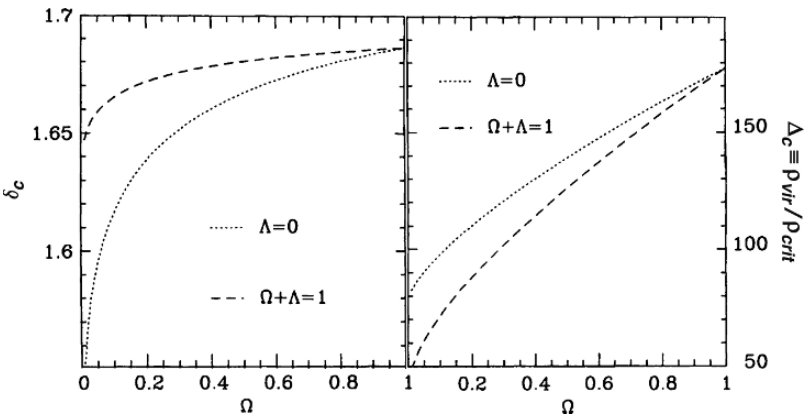

Fig. 5. Left frame: Critical threshold for collapse, f_c, as a function of Ω_m, in the spherical collapse model. Results are plotted for open models with $\Lambda = 0$ (*dotted line*) and flat models with $\Omega_m + \Omega_\Lambda = 1$ (*dashed line*). Righthand panel: the (nonlinear) virial density of collapsed objects in units of critical density. From Eke et al. [27]. Image courtesy of Vincent Eke

Spherical Collapse and Primordial Density Field

Given the primordial density field $\delta_L(\mathbf{x}, t)$, linearly interpolated to the present epoch, at any one cosmic epoch t (redshift z) one may identify the peaks that have condensed into collapsed objects by tracing the regions for whom the filtered primordial density excess

$$\delta_L(\mathbf{x}, t|R) \; > \; \frac{f_c(z)}{D(z)} \; \equiv \; f_{sc}(z)\,, \tag{28}$$

where the index sc refers to "spherical collapse". For a Gaussian random field, the statisistical distribution of $\delta_L(\mathbf{r}, t|R)$, is

$$P(\delta_L)\,\mathrm{d}\delta_L \; = \; \exp[-\delta_L^2(\mathbf{r}, t|R)/2S(R,t)]\,\mathrm{d}\delta_L/\sqrt{2\pi S(R,t)} = \exp[-\nu^2/2]\,\mathrm{d}\nu/\sqrt{2\pi}\,,$$
$$\nu = \delta_L(\mathbf{r}, t|R)/\sigma_W(R,t)\,, \quad S(R,t) = \sigma_W^2(R,t)\,. \tag{29}$$

The number of σ is ν, which is a Gaussian random deviate (i.e., is distributed as the unit-variance normal). The threshold on scale M is therefore achieved when the height ν in σ units is

$$\nu(M) \; = \; \frac{f_c}{\sigma_W(M)}\,. \tag{30}$$

High mass objects are very rare because $\sigma_W(M)$ is at low, hence $\nu(M)$ is high.

Collapse and Halo Shape

While the above is based upon spherical collapse, in realistic circumstances primordial density perturbations will never be spherical, nor isolated [6]. In Bond & Myers [17], Sheth & Tormen [76], the dependence upon the shape of the density peak as well as on the tidal influences of the surrounding matter fluctuations were worked out (see Sect. 4.5 for a detailed description of anisotropic ellipsoidal collapse).

In a spherical collapse, the evolution of the outer radius depends only upon the average interior properties of the perturbation, and does not depend upon what the external matter is doing. Non-spherical perturbations such as ellipsoids of course collapse anisotropically. An ellipsoidal overdensity will first collapse along its shortest axis, subsequently along its medium axis and finally along its longest axis. However, the evolution of the outer shell depends upon the details of the interior distribution and on the exterior through the tidal forces acting upon the shell so it is not as clean a case as spherical collapse. There has been a long history of using homogeneous ellipsoids to model anisotropic collapses. Isolated ellipsoids were considered by Icke [38], White & Silk [88]; Peebles [62]. The extension to a cosmological setting where the exterior tidal forces were accurately included formulating it by its relation to the linear deformation tensor of the interior was made by Bond & Myers [17].

This paper showed the collapse along the shortest axis will occur more rapidly than the collapse of comparable spherical peak, that of the medium axis will not differ too much from the spherical value while full collapse along all three axes will be slower than that of its spherical equivalent. This was applied to filtered density peaks by Bond & Myers [17], who determined the critical density threshold $f_{\rm c}$ for complete collapse as a function of the linear tidal field environment or deformation described below, and to random filtered-field points by Sheth et al. [75].

Similar considerations concerning the effect of the non-spherical collapse of density peaks on the mass function of bound objects had been followed in a number of other studies. Monaco [56, 57, 58], Audit et al. [4] and Lee & Shandarin [51] studied models in which the initial (Zel'dovich) deformation tensor was used to find estimates of the collapse time. However, when following the nonlinear evolution of the same configuration by means of a corresponding (homogeneous) ellipsoidal collapse model Bond & Myers [17]; Eisenstein & Loeb [26] found marked differences. Figure 13 in Sect. 4.4 shows a telling comparison between the corresponding collapse time estimates for all three axes of a density peak.

The collapse of a spherical peak depends only upon the density, which is the trace of the deformation tensor, hence $f_c = f_{sc}$ is constant. For a non-spherical peak, the deformation tensor has an anisotopic part as well, with two (normalized) eigenvalues, the ellipticity e and its prolateness p and the collapse threshold depends upon these values, $f_{\rm ec}(e,p)$ [6, 17]. An impression of the sensitivity to e and p of the collapse time $a_{\rm c}(e,p)$ and corresponding collapse threshold $f_{\rm ec}(e,p)$ may be obtained from Fig. 6, which depicts these for an ellipsoidal perturbation in an Einstein-de Sitter Universe. For an ellipsoidal overdensity with the same initial overdensity δ_i the symbols show the expansion factor when the longest axis of the ellipsoid collapses and virializes, as a function of e and p. The axis on the right shows the associated critical overdensity required for collapse. At a given e, the large, medium and small circles show the relation at $p = 0$, $|p| \leq e/2$ and $|p| \geq e/2$, respectively. The solid curve and dashed curves depict the analytical relation specified in Sheth et al. [75] for $p = 0$ and $|p| = e/2$. The time required to collapse increases monotonically as p decreases. The top axis shows the related mass scale $\sigma(m)$ when identified with the value of e as the corresponding most probable value for p=0 (see Sheth et al. [75]).

The main conclusion is that for ellipsoidal collapse the density threshold f_{ec} becomes a "moving barrier", dependent on the ellipticity e and/or the mass scale $\sigma(m)$. On the basis of such ellipsoidal dynamics calculations and normalized by means of N-body simulations, Sheth & Tormen [76] found that the density collapse barrier may be reasonably accurate approximated by the expression

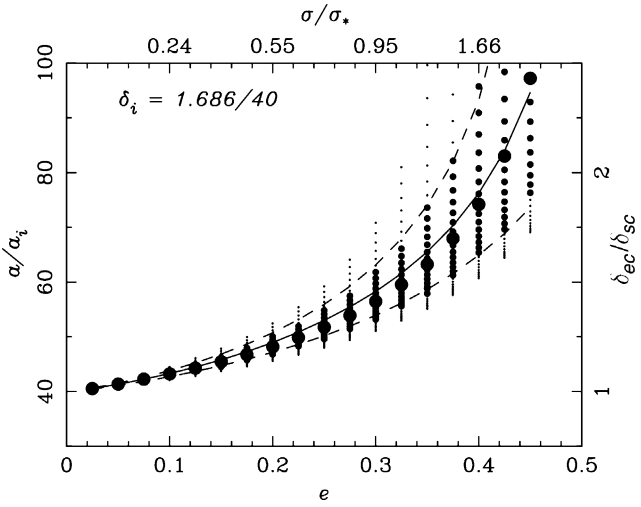

Fig. 6. Evolution of an ellipsoidal perturbation in an Einstein-de Sitter universe. Symbols show the expansion factor when the longest axis collapses and virializes as a function of initial e and p with the same initial overdensity δ_i. The circles correspond to different values of p (see text). The time required to collapse increases monotonically as p decreases. **Right axis:** associated collapse overdensity required for collapse. **Top axis:** estimate of mass resolution $\sigma(m)$ based on the corresponding most probable ellipticity e. From Sheth et al. [75]. Image courtesy of Sheth

$$f_{ec}(\sigma, z) \approx f_{sc}(z) \left\{1 + \beta \left[\frac{f_{sc}^2(z)}{\sigma^2(M)}\right]^{-\alpha}\right\} = f_{sc}(z) \left\{1 + \beta\, \nu(M, z)^{-\alpha}\right\} \tag{31}$$

with $\beta \approx 0.485$ and $\alpha \approx 0.615$. Figure 7 shows a few examples of moving barriers for a slightly different context. In this expression, $f_{\rm sc}(z)$ is the critical overdensity required for spherical collapse at a redshift z and $\sigma(M)$ the rms initial density fluctuation smoothed on a mass scale M, both linearly extrapolated to the present epoch. The parameters β and α are determined by ellipsoidal collapse: strictly speaking $\alpha = 0$ and $\beta = 0$ for spherical collapse, yielding the correct asymptotic value $f_{ec} = f_{sc}$. Cosmology enters via the relation f_{sc}, while the influence of the power spectrum enters via $\sigma(M)$. The corresponding modifications have been shown to lead to considerable improvements in the predictive power of the excursion set formalism describing the mass spectrum of condensed objects [76].

Equation 32 shows massive objects with low $\sigma(M)$ have $f_{ec}(z) \approx f_{sc}(z)$, well described by spherical collapse, whereas less massive objects are increasingly affected by external tidal forces as $\sigma(M)$ rises and M decreases. Critical

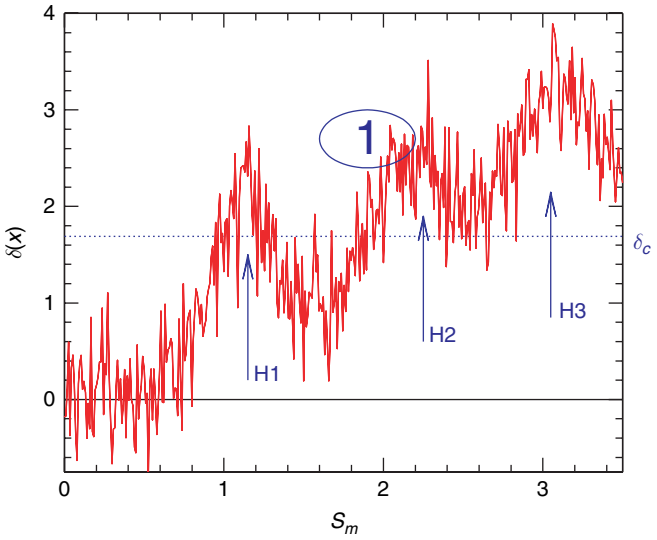

Fig. 7. Excursion Set Formalism, illustrated for the formation of a halo. Random walk exhibited by the average overdensity δ centred on a randomly chosen position in a Gaussian random field, as a function of smoothing scale, parametrized by S_M (large volumes are on the left, small volumes on the right). Dashed horizontal line indicates the collapse barrier f_c. The largest scale (smallest value of S) on which $\delta(S)$ exceeds f_c is an estimate of the mass of the halo which will form around that region. From Sheth & van de Weygaert [77]

thresholds can also be determined for other structural features, such as voids, using 2 thesholds [77] and walls and filaments (Sect. 3.3).

3.4 Halo Excursions

The excursion set formalism, also known as extended Press–Schechter formalism Press & Schechter [67], Peacock & Heavens [61], Bond et al. [16], Sheth [74], evaluates the effects substructure over a range of scales has on the emergence of objects in a cosmic density field. For an early paper on see Epstein [28] and for a recent review see [91].

It elucidates the hierarchical development of structure using just the linear density and tidal fluctuations in combination with the knowledge of their fate once the linear smoothed density exceeds the threshold values f_c we have discussed. The idea is that around a point $\mathbf{r}$, $\delta_L\mathbf{r}, t|R)$ defines a trajectory, starting from zero at very large R to larger values at small R. We have seen that $S(M)$ is a convenient clock increasing from high mass to low, hence we can also consider the smoothed field as a function of $S = \sigma_W^2(R)$: $\delta_L(\mathbf{r}, t|S)$. Further, since $S(R,t) = D^2(t)S(R,t_0)$, where t_0 is the current time, $\delta_L(\mathbf{r}, t|S(t))/sqrtS(t)$ is independent of t, a function only of $S(t_0)$ which acts

like a pseudo-time. For each $\mathbf{r}$, we have a trajectory in resolution S, $\delta_L(S)$. When δ_L reaches the f_c *barrier*, we identify the scale R with the mass of a collapsed object of mass $M(S)$ at that position. The reader will realize that this prescription is unrealistic in that points very near to each other may have their density fields piercing the barrier at different S, hence be indentified with objects of different mass even though they collapse together. At best the prescription can be statistically valid but not a true real space description. That requires a non-local treatment. Further, since small-scale density peaks are embedded within larger regions which may or may not have pierced the critical collapse threshold. If the larger region has collapsed this will have involved the merging of the small scale peak with its neighbouring halos and surrounding matter while it got absorbed into the more massive entity. Consider the sharp-k filter with its $S_M = S(R_k)$ integrated power. If the linear primordial density field is a homogeneous random Gaussian field, the N-point correlation functions are translation invariant and the Fourier components $\hat{\delta}(\mathbf{k})$ are independent, that is uncorrelated in k. Sliding from a resolution S_M to a higher resolution $S_M + \Delta S_M$, the filtering process in essence involves the increment by a random Gaussian variate $\hat{\delta}(\mathbf{k})$.

Figure 7 shows an example of a typical result: a jagged line representing the linear overdensity centered on a randomly chosen position $\mathbf{r}$ in the initial Gaussian random field as a function of the scale S_M. Because of the independence of each of the Gaussian distributed Fourier components, the process turns into that of a *Brownian random walk*. The density threshold f_c for forming bound virialized objects is given by the dashed line, assumed mass independent here hence the line is horizontal. The largest scales, $S_M = 0$, are those of the homogeneous global FRW Universe so that the random walk will start of at $\delta(S = 0) = 0$. In hierarchical models S_M will increase as we zoom in on to an increasingly resolved mass distribution around the chosen position $\mathbf{x}$. As we move to a higher S_M and smaller R fluctuations of an increasing amplitude will get involved.

The distribution of masses of collapsed and/or virialized objects is equated to the distribution of distances S_M which one-dimensional Brownian motion random walks travel before they first cross a barrier of constant height f_c. In other words, one should find the distribution of the *first upcrossing* of the random trajectory, the lowest value of S for which $\delta(\mathbf{r}|S) = f_c$. The rate of first upcrossings at a threshold was calculated by Chandrasekhar (1943). When the random walk is absorbed by the barrier at the first upcrossing at S, the point $\mathbf{r}$ is identified with a collapsed object of mass $M(S)$. Here rate is per unit psuedo-time, or per unit resolution, dS. In the absence of a barrier, the distribution of trajectories with a density value $\delta_L(S)$ at S is the usual Gaussian distribution:

$$\Pi(\delta_L, S) \;=\; \frac{1}{\sqrt{2\pi\, S}}\, \exp\left\{-\frac{\delta_L^2}{2S}\right\} \tag{32}$$

In the presence of a barrier f_c, the probability distribution $\Pi(\delta_L, S|f_c)$ of trajectories which have a density δ_L at resolution S_M but did not cross the boundary at smaller $S < S_M$) follows from solving the Fokker-Planck equation (see Bond et al. [16], Zentner [91]),

$$\frac{\partial \Pi}{\partial S} = \lim_{\Delta S \to 0} \left\{ \frac{\langle (\Delta\delta)^2 \rangle}{2\Delta S} \frac{\partial^2 \Pi}{\partial \delta^2} - \frac{\langle \delta \Delta\delta \rangle}{\Delta S} \frac{\partial \Pi}{\partial \delta} \right\}, \tag{33}$$

where the next step in the trajectory, $\Delta\delta_L(S) = \delta_L(S + \Delta S) - \delta_L(S)$ as we increment the resolution by ΔS. The critical feature of sharp k-filter is that this step is uncorrelated with the prior value, $\langle \delta_L(S) \Delta\delta_L(S) \rangle = 0$, in which case the drift term vanishes and simple diffusion remains,

$$\frac{\partial \Pi}{\partial S} = \frac{1}{2} \frac{\partial^2 \Pi}{\partial \delta^2}. \tag{34}$$

There is a simple graphical way of determining Π. Consider a trajectory which has reached the threshold for some scale $S < S_M$. Its subsequent path is entirely symmetric and at S_M it is equally likely to be found above as well as below the threshold (see Fig. 7). In other words, for each of these trajectories there is an equally likely trajectory that pierced the barrier at the same scale R but whose subsequent path is a reflection in the barrier, ending up below the threshold. The probability Π that the threshold has never been crossed may be obtained by subtracting the reflected distribution from the overall Gaussian distribution (32),

$$\Pi(\delta_L, S_M|f_c) = \frac{1}{\sqrt{2\pi\, S_M}} \left\{ \exp\left(-\frac{\delta_L^2}{2S_m} \right) - \exp\left(-\frac{(\delta_L - 2f_c)^2}{2S_m} \right) \right\}. \tag{35}$$

Integrating this distribution over all values δ_L yields the probability that the threshold has been crossed at least once, and the corresponding probability that the location is enclosed in an object of mass $\leq M$,

$$P_s(S_M|f_c) = 1 - \int \mathrm{d}\delta_L \; \Pi(M|f_c) = 1 - \mathrm{erf}\left\{ \frac{f_c}{\sqrt{2}\sigma(M,t)} \right\} \tag{36}$$

in which $\mathrm{erf}(x)$ is the conventional error function. In an entirely natural fashion this probability takes care of the so-called fudge factor 1/2 which had been missed in the original Press–Schechter result Press & Schechter [67]. They assumed that the fraction of mass in objects of mass $\geq M$ is given by the fraction of mass above the threshold f_c at resolution S_M. This fails to take into account that there are mass fluctuations which did not reach the threshold at mass scale M, yet are part of a collapsed structure on larger mass scale. Indeed, we will see that this is also an essential issue in understanding the development of a *void hierarchy* (see accompanying notes, van de Weygaert & Bond (2005)).

3.5 Halo Mass Distribution

Given the identification of mass, $M(S)$, we may readily infer the number density $n(M)$ of objects of mass M from the mass excursion probability $\Pi(M)$ (35):

$$n(M)\, d\ln M \;=\; \frac{\bar{\rho}_m}{M}\, \left|\frac{\mathrm{d}P_s}{\mathrm{d}S}\right|\, \frac{\mathrm{d}S}{d\ln M} d\ln M \tag{37}$$

which translates into

$$n(M)\,\mathrm{d}M \;=\; \sqrt{\frac{2}{\pi}}\, \frac{\rho_u}{M^2}\, \nu(M)\, \exp\left\{-\frac{\nu(M)^2}{2}\right\}\, \left|\frac{d\ln\sigma(M)}{d\ln M}\right| \tag{38}$$

For a pure power-law power spectrum, $P(k) \propto k^n$, one may readily observe that the mass spectrum of virialized and bound objects in the Universe is a self-similar evolving function

$$n(M)\,\mathrm{d}M \;=\; \sqrt{\frac{1}{2\pi}}\, \left(1+\frac{n}{3}\right)\, \frac{\rho_u}{M^2}\, \left(\frac{M}{M_*}\right)^{(3+n)/6}\, \exp\left\{-\left(\frac{M}{M_*}\right)^{(3+n)/3}\right\}. \tag{39}$$

The self-similar evolution of the mass distribution is specified via the time development of the characteristic mass $M_*(t)$,

$$M_*(t) \;=\; D(t)^{6/(3+n)}\, M_{*,o}\,. \tag{40}$$

whose present-day value is inversely proportional to f_c,

$$M_{*,0} \;=\; \left(\frac{2A}{f_c^2}\right)^{3/(3+n)}\,. \tag{41}$$

For a ΛCDM Universe, with $\Omega_m = 0.3$, Fig. 8 depicts the predicted Press–Schechter halo mass functions at several different redshifts [7]: $z = 0$ (solid curve), $z = 5$ (dotted curve), $z = 10$ (short-dashed curve) and $z = 20$ (long-dashed curve).

3.6 Hierarchical Evolution

Smaller mass condensations may have corresponded with genuine physical objects at an earlier phase, while later they may have been absorbed into a larger mass concentration. It is straightforward and insightful to work out the evolving object distribution within the context of the excursion set formalism.

Returning to the graphical representation in Fig. 7 we may easily appreciate what happens as the mass distribution evolves. The linear growth of fluctuations implies a gradual uniform rise of the whole random walk curve as each mass fluctuations increase by the linear growth factor $D(z)$. Going back in

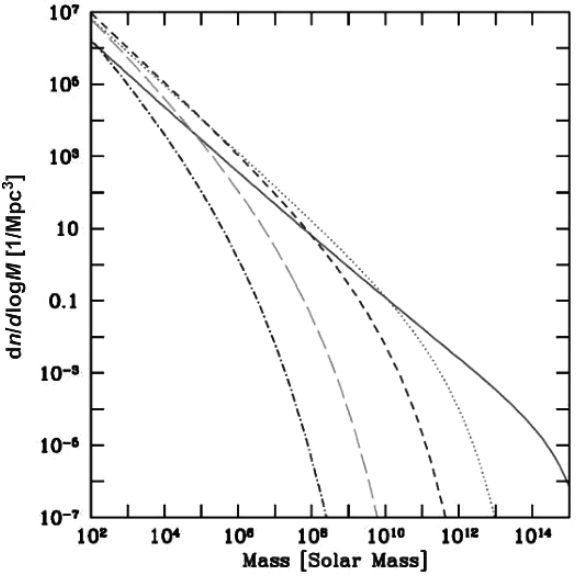

Fig. 8. Press–Schechter halo mass function at several different redshifts: z = 0 (*solid curve*), z = 5 (*dotted curve*), z = 10 (*short-dashed curve*) and z = 20 (*long-dashed curve*). From Barkana & Loeb [7]. Reproduced with permission of Elsevier

time the random walk curve would therefore have had a proportionally smaller amplitude. Linearly translated to the present epoch the density threshold barrier would gradually decrease in amplitude, proportional to $1/D(z)$. Earlier barrier crossings would therefore have occurred at a higher values of $S(R)$, a smaller scale R and a smaller mass M: Location $\mathbf{x}$ would have been incorporated within an object of a correspondingly smaller mass.

As we proceed in time the barrier $f_c(z)$ would descend further. Gradually the random walk path will start to pierce through the barrier at lower S and correspondingly larger values of the mass scale M. The halo into which the point may be embedded will first accrete surrounding matter, thereby gradually growing in mass. Even later the halo may merge with surrounding clumps into a much more massive halo. The corresponding mass scale would reveal itself as the next peak in the random walk. Figure 7 does reveal such behaviour through the presence of three peaks, H1, H2 and H3: H3 corresponds to an early small object that merged with surrounding mass into the more massive peak H2. The latter would merge again with neighbouring peers into the largest clump, object H1.

While the excursion set formalism manages to describe quantitatively the merging and accretion history of halos in a density field, it has opened up the analysis of merging histories of objects in hierarchical scenarios of structure formation [21, 46, 47] and the related construction of the *merger tree* of the population of dark halos [42, 46].

3.7 Extension to the Four Mode Two-Barrier Excursion Set Formalism

We have seen that the hierarchical nature of the cosmic structure formation process plays a prominent role in the nonlinear evolution of and graudal buildup of galaxies, galaxy halos and clusters. In the following sections we will see that it affects all aspects of the nonlinear evolution of large scale structure, including the morphology of filaments and the properties of the void population.

With respect to the void population, we will find that there is a distinct asymmetry between the nonlinear hierarchical evolution of voids and that of haloes (see accompanying review on morphology of the cosmic web). For the evaluation of the hierarchical evolution of voids two processes need to be taken into account: the *void-in-void* process avoids double counting of voids while the *void-in-cloud* process removes voids within encompassing overdensities. What distinguishes voids from their collapsing peers is that clusters will always survive when located within a void, while the reverse is not true: voids within overdense clusters will be rapidly squeezed out of existence.

Sheth & van de Weygaert [77] have shown that the excursion set formalism provides a mathematically properly defined context for describing the asymmetry between void and haloes. The related extension of the formalism to a *two-barrier* formalism culminates in a *four mode* formalism. In this section we summarize these findings, while we refer to [85] for a more proper treatment of the evolution of voids. Figure 9 illustrates the argument. There are four sets of panels. The left-most of each set shows the random walk associated with the initial particle distribution. The two other panels show how the same particles are distributed at two later times.

Cloud-in-Cloud

The first set illustrates the *cloud-in-cloud* process. The mass which makes up the final object (far right) is given by finding that scale within which the linear theory variance has value $S = 0.55$. This mass came from the mergers of the smaller clumps, which themselves had formed at earlier times (centre panel). If we were to center the random walk path on one of these small clumps, it would cross the higher barrier $f_c/D(t) > f_c$ at $S > 0.55$, the value of $D(t)$ representing the linear theory growth factor at the earlier time t.

Cloud-in-Void

The second series of panels shows the *cloud-in-void* process. Here, a low mass clump ($S > 0.85$) virializes at some early time. This clump is embedded in a region which is destined to become a void. The larger void region around it actually becomes a bona-fide void only at the present time, at which time it contains significantly more mass ($S = 0.4$) than is contained in the low mass

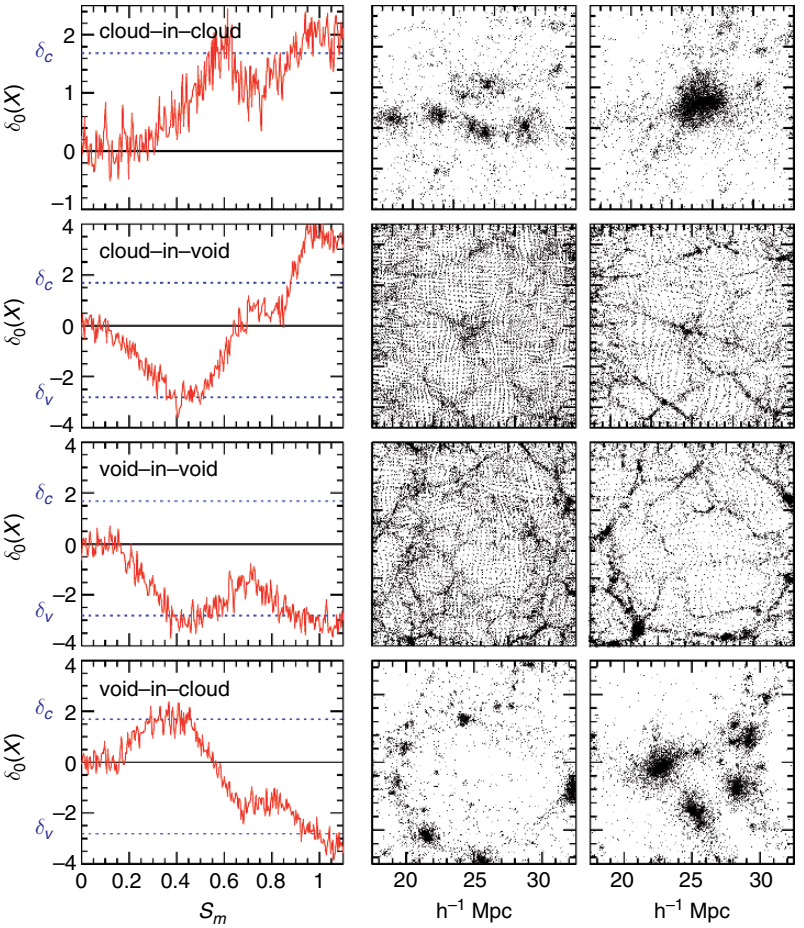

Fig. 9. Four mode two-barrier excursion set formalism. Each row illustrates one of the four basic modes of hierarchical clustering: the *cloud-in-cloud* process, *cloud-in-void* process, *void-in-void* process and *void-in-cloud* process (from **top** to **bottom**). Each mode is illustrated using three frames. Leftmost panels show 'random walks': the local density perturbation $\delta_0(\mathbf{x})$ as a function of (mass) resolution scale S_M (cf. Fig. 7) at an early time in an N-body simulation of cosmic structure formation. In each graph, the dashed horizontal lines indicate the *collapse barrier* f_c and the shell-crossing *void barrier* f_v. The two frames on the right show how the associated particle distribution evolves. Whereas halos within voids may be observable (second row depicts a halo within a larger void), voids within collapsed halos are not (last row depicts a small void which will be squeezed to small size as the surrounding halo collapses). It is this fact which makes the calculation of void sizes qualitatively different from that usually used to estimate the mass function of collapsed halos. From Sheth & van de Weygaert [77]

clump at its centre. Notice that the cloud within the void was not destroyed by the formation of the void; indeed, its mass increased slightly from $S > 0.85$ to $S \sim 0.85$. Such a random walk is a bona-fide representative of $S \sim 0.85$ halos; for estimating halo abundances, the presence of a barrier at f_v is irrelevant. On the other hand, walks such as this one allow us to make some important inferences about the properties of void-galaxies, which we will discussess shortly.

Void-in-Void

The third series of panels shows the formation of a large void by the mergers of smaller voids: the *void-in-void* process. The associated random walk looks very much the inverse of that for the cloud-in-cloud process associated with halo mergers. The associated random walk shows that the void contains more mass at the present time ($S \sim 0.4$) than it did in the past ($S > 0.4$); it is a bona-fide representative of voids of mass $S \sim 0.4$. A random walk path centered on one of these mass elements which make up the filaments within the large void would resemble the cloud-in-void walk shown in the second series of panels. [Note that the height of the barrier associated with voids which are identified at cosmic epoch t scales similarly to the barrier height associated with halo formation: $f_v(t) \equiv f_v/D(t)$.]

Void-in-Cloud

Finally, the fourth series of panels illustrates the *void-in-cloud* process. The particle distribution shows a relatively large void at the early time being squeezed to a much smaller size as the ring of objects around it collapses. A simple inversion of the cloud-in-void argument would have tempted one to count the void as a relatively large object containing mass $S \sim 1$. That this is incorrect can be seen from the fact that, if we were counting halos, we would have counted this as a cloud containing significantly more mass ($S \sim 0.3$), and it does not make sense for a massive virialized halo to host a large void inside.

3.8 Peak Structure

While the extended Press–Schechter excursion set formalism does provide a good description of the mass functions of cosmological objects, it basically involves an intrinsically local description and does not deal with the real internal structure of a genuine collapsed and virialized peak in the mass distribution. Points which would collapse together to form a virialized object of a given mass may be counted as belonging to objects of different mass [16]. Another unappealing aspect is that the derivation of the Press–Schechter formula requires

the unphysical sharp k-filter, a rather unphysical form of density smoothing, and a rather arbitrary mass assignment scheme.

It is the nonlocal *peak-patch* description of Bond & Myers [17] that is able to incorporate a more global description of evolving volume elements.

4 Anisotropic and Weblike Patterns

The second key characteristic of the cosmic matter distribution is that of a *weblike geometry* marked by highly elongated filamentary, flattened planar structures and dense compact clusters surrounding large near-empty void regions (see Fig. 1). In this section we focus on the backbone – or skeleton – of the Cosmic Web defined by these anisotropic filamentary and sheetlike patterns.

The recognition of the *Cosmic Web* as a key aspect in the emergence of structure in the Universe came with early analytical studies and approximations concerning the emergence of structure out of a nearly featureless primordial Universe. In this respect the Zel'dovich formalism [90] played a seminal role. It led to view of structure formation in which planar pancakes form first, draining into filaments which in turn drain into clusters, with the entirety forming a cellular network of sheets. As borne out by a large sequence of N-body computer experiments of cosmic structure formation, weblike patterns in the overall cosmic matter distribution do represent a universal but possibly transient phase in the gravitationally driven emergence and evolution of cosmic structure. The N-body calculations have shown that weblike patterns defined by prominent anisotropic filamentary and planar features – and with characteristic large underdense void regions – are a natural manifestation of the gravitational cosmic structure formation process.

Interestingly, for a considerable amount of time the emphasis on anisotropic collapse as agent for forming and shaping structure was mainly confined the Soviet view of structure formation, Zel'dovich's pancake picture, and was seen as the rival view to the hierarchical clustering picture which dominated the western view. Here we intend to emphasize the succesfull synthesis of both elements on the basis of the peak patch description of Bond & Myers [17]. It forms the most elaborate and sophisticated analytical description for the emergence of walls, filaments and fully collapsed triaxial halos in the cosmic matter distribution. Culminating in the Cosmic Web theory [18] it stresses the dominance of filamentary shaped features instead of the dominance of planar pancakes in the pure Zel'dovich theory. Perhaps even more important is its identification of the intimate dynamical relationship between the filamentary patterns and the compact dense clusters that stand out as the nodes within the cosmic matter distribution: filaments as cluster–cluster bridges. To appreciate the intricacies of the *Cosmic Web* theory we need to understand the relation between gravitational tidal forces and the resulting deformation of the matter distribution.

4.1 Anisotropic Collapse

The existence of the Cosmic Web is a result of this tendency of matter concentrations to contract and evolve into anisotropic, elongated or flattened, structures. It is a manifestation of the generic *anisotropic* nature of gravitational collapse, a reflection of the intrinsic anisotropy of the gravitational force in a random density field.

Anisotropic gravitational collapse is the combined effect of *internal* and *external* tidal forces. The *internal* force field of the structure hangs together with the flattening of the feature itself. It induces an anisotropic collapse along the main axes of the structure. The resulting evolution can be most clearly understood in and around a density maximum (or minimum) δ, to first order corresponding to the collapse of a homogeneous ellipsoid [17, 24, 26, 38, 88]. The *external* 'background' force field is the integrated gravitational influence of all external density features in the Universe, as such a manifestation of the inhomogeneous cosmic matter distribution. For most situations the role of the large scale tidal forces in the early phases of the collapse of a feature – the evolutionary phase in which most elements of the cosmic web reside – may be succesfully described by the Lagrangian Zel'dovich formalism [90].

The *peakpatch* formalism embeds the anisotropic tendency of gravitational collapse within the context of a hierarchical mass distribution. It achieves this by combining the nonlinear internal evolution of a particular region in the cosmic mass distribution, and modelling this by means of the homogeneous ellipsoid model, with a reasonably accurate description of the large-scale external tidal influence in terms of the Zel'dovich approximation [17, 75].

4.2 Force Field and Displacement

For the description of the dynamical evolution of a region in the density field – a *patch*- it is beneficial to make a distinction between large scale "background" fluctuations $\delta_{\rm b}$ and small-scale fluctuations $\delta_{\rm f}$,

$$\delta(\mathbf{x}) \,=\, \delta_{\rm b}(\mathbf{x}) \,+\, \delta_{\rm f}(\mathbf{x})\,, \tag{42}$$

in which

$$\begin{aligned} \delta_{\rm f}(\mathbf{x}) \,&=\, \int \frac{{\rm d}\mathbf{k}}{(2\pi)^3}\, \hat{\delta}(\mathbf{k})\, \hat{W}^*_{\rm f}(\mathbf{k}; R_b) \\ \delta_{\rm b}(\mathbf{x}) \,&=\, \int \frac{{\rm d}\mathbf{k}}{(2\pi)^3}\, \hat{\delta}(\mathbf{k})\, \hat{W}^*_{\rm b}(\mathbf{k}; R_b) \end{aligned} \tag{43}$$

$\hat{W}^*_{\rm f}(\mathbf{k}; R_b)$ is a high-pass filter which filters out spatial wavenumber components lower than $k < 1/R_b$. $\hat{W}^*_{\rm b}(\mathbf{k}; R_b)$ is the compensating low-pass filter. The small-scale fluctuating density field $\delta_{\rm f}$ exclusively contributes to the internal evolution of the patch. Predominantly made up of spatial wavenumber components higher than $1/R_b$, it determines the substructure within the patch,

sets the corresponding merging times while influencing the overall collapse time of the mass element (see Fig. 22). For our picture to remain valid the scale R_b of the smooth large-scale field should be chosen such that it remains (largely) linear, i.e. the r.m.s. density fluctuation amplitude $\sigma_\rho(R_b,t) \lesssim 1$. Note that the smooth large-scale field $\delta_{\rm b}$ also contributes to the total mass content within the patch.

The small-scale local inhomogeneities induce small-scale fluctuations in the gravitational force field, $\mathbf{g}_{\rm f}(\mathbf{x})$. To a good approximation the smoother background gravitational force $\mathbf{g}_{\rm b}(\mathbf{x})$ (see (2) in and around the mass element includes three components (excluding rotational aspects). The *bulk force* $\mathbf{g}_{\rm b}(\mathbf{x}_{pk})$ is responsible for the acceleration of the mass element as a whole. The divergence $(\nabla\cdot\mathbf{g}_{\rm b})$ encapsulates the collapse of the overdensity while the tidal tensor quantifies its deformation,

$$g_{\rm b,i}(\mathbf{x}) \,=\, g_{\rm b,i}(\mathbf{x}_{pk}) \,+\, a\sum_{j=1}^{3}\left\{\frac{1}{3a}(\nabla\cdot\mathbf{g}_{\rm b})(\mathbf{x}_{pk})\,\delta_{\rm ij} \,-\, T_{\rm b,ij}\right\}(x_j - x_{pk,\rm j})\,. \quad (44)$$

The tidal shear force acting over the mass element is represented by the tidal tensor T_{ij},

$$T_{\rm b,ij} \,\equiv\, -\frac{1}{2a}\left\{\frac{\partial g_{{\rm b},i}}{\partial x_i} + \frac{\partial g_{{\rm b},j}}{\partial x_j}\right\} \,+\, \frac{1}{3a}(\nabla\cdot\mathbf{g}_{\rm b})\,\delta_{\rm ij} \quad (45)$$

$$\,=\, \frac{1}{a^2}\,\frac{\partial^2\Phi_b}{\partial x_i\,\partial x_j} \,-\, \frac{3}{2}\,\Omega H^2\,\delta_{\rm b}(\mathbf{x})\,\delta_{\rm ij}\,, \quad (46)$$

in which the trace of the collapsing mass element, proportional to its overdensity δ_b, dictates its contraction (or expansion).

The force field induces displacements of matter in and around the mass element. The resulting displacement $\mathbf{s}(\mathbf{q},t)$ consists of a superposition of the small-scale and smooth large-scale contributions, $\mathbf{s}_f$ and $\mathbf{s}_b$: matter initially at a (Lagrangian) position $\mathbf{q}$ moves to a location $\mathbf{x}(\mathbf{q},t)$,

$$\mathbf{x}(\mathbf{q},t) \,=\, \mathbf{q} \,+\, \mathbf{s}(\mathbf{q},t) \,=\, \mathbf{q} \,+\, \mathbf{s}_{\rm b}(\mathbf{q},t) \,+\, \mathbf{s}_{\rm f}(\mathbf{q},t)\,. \quad (47)$$

The smooth large-scale displacement field $\mathbf{s}_{\rm b}$ in and around the patch includes a *bulk displacement* $\mathbf{s}_{pk}$ and a deforming *strain* $\mathcal{E}_{pk,\rm ij}$,

$$s_{\rm b,i}(\mathbf{q},t) \,\approx\, s_{pk,\rm i} \,+\, \sum_{j=1}^{3}\mathcal{E}_{pk,\rm ij}\,(q_{\rm j} - q_{pk,\rm j})\,, \qquad i=1,\ldots,3\,. \quad (48)$$

The bulk displacement of the (mass) center of the peak

$$\mathbf{s}_{pk} \,\equiv\, \mathbf{s}_{\rm b}(\mathbf{q}_{pk})\,, \quad (49)$$

specifies the movement of the mass element as a whole. The large-scale strain field $\mathcal{E}_{b,ij}$ at the location of the patch, $\mathcal{E}_{pk,\mathrm{ij}} \equiv \mathcal{E}_{b,ij}(\mathbf{q}_{pk})$,

$$\mathcal{E}_{\mathrm{b,ij}}(\mathbf{q}) \equiv \frac{1}{2}\left\{\frac{\partial s_{\mathrm{b,i}}}{\partial q_j} + \frac{\partial s_{\mathrm{b,j}}}{\partial q_i}\right\}(\mathbf{q})\,. \tag{50}$$

embodies the (gravitationally induced) deformation, in volume and shape, of the mass element,

$$\mathcal{E}_{pk,\mathrm{ij}} \equiv \mathcal{E}'_{pk,\mathrm{ij}} + \frac{1}{3a}(\nabla\cdot\mathbf{s}_b)(\mathbf{q}_{pk})\,\delta_{\mathrm{ij}}\,. \tag{51}$$

The peak strain's trace $(\nabla\cdot\mathbf{s}_b)(\mathbf{q}_{pk})$ quantifies the shrinking volume of the mass element while the tensor $\mathcal{E}'_{pk,\mathrm{ij}}$ embodies the - mostly externally induced - anisotropic deformation of the region.

The source for the external deformation $\mathcal{E}'_{\mathrm{st,ij}}$ is the external tidal field $T_{\mathrm{b,ij}}$. In the early phases of gravitational collapse the role of the large scale tidal forces is succesfully framed in terms of the by Zel'dovich formalism [90]. The internally induced deformation, a reaction to the nonspherical shape of the mass element, will rapidly enhance along with the nonlinear collapse of the peak.

4.3 Zel'dovich Approximation

In a seminal contribution Zel'dovich [90] found by means of a Lagrangian perturbation analysis that to first order – typifying early evolutionary phases – the reaction of cosmic patches of matter to the corresponding peculiar gravity field would be surprisingly simple. The *Zel'dovich approximation* is based upon the first-order truncation of the Lagrangian perturbation series of the trajectories of mass elements,

$$\mathbf{x}(\mathbf{q},t) = \mathbf{q} + \mathbf{x}^{(1)}(\mathbf{q},t) + \mathbf{x}^{(2)}(\mathbf{q},t) + \ldots\,, \tag{52}$$

in which the successive terms $\mathbf{x}^m$ correspond to successive terms of the relative displacement $|\partial(\mathbf{x}-\mathbf{q})/\partial\mathbf{q}|$,

$$1 \gg \left|\frac{\partial\mathbf{x}^{(1)}}{\partial\mathbf{q}}\right| \gg \left|\frac{\partial\mathbf{x}^{(2)}}{\partial\mathbf{q}}\right| \gg \left|\frac{\partial\mathbf{x}^{(3)}}{\partial\mathbf{q}}\right| \gg \ldots\,, \tag{53}$$

and embodies the solution of the Lagrangian equations for small density perturbations ($\delta^2 \ll 1$). Assuming *irrotational motion*, in accordance with linear gravitational instability, and restricting the solution to the *growing mode* leads to the plain ballistic linear displacement of the Zel'dovich approximation,

$$\mathbf{x} = \mathbf{q} - D(t)\,\boldsymbol{\nabla}\Psi(\mathbf{q}) = \mathbf{q} - D(t)\,\boldsymbol{\psi}(\mathbf{q})\,. \tag{54}$$

dictated by the Lagrangian *displacement potential* $\Psi(\mathbf{q})$ and its gradient, the Zel'dovich deformation tensor $\boldsymbol{\psi}_{\mathrm{mn}}$. The path's time evolution is specified by

the linear density growth factor $D(a)$ [62] (14). An essential aspect of the Zel'dovich approximation is the $1-1$ relation between the *displacement potential* $\Psi(\mathbf{q})$ and the (primordial, linearly extrapolated) gravitational potential $\tilde{\Phi}(\mathbf{q},t)$

$$\Psi(\mathbf{q}) \;=\; \frac{2}{3\,D\,a^2H^2\,\Omega}\;\tilde{\Phi}(\mathbf{q},t) \;=\; \frac{2}{3\,H_0^2\,\Omega_0}\;\tilde{\Phi}_0(\mathbf{q})\,, \tag{55}$$

where $\tilde{\Phi}_0$ is the linearly extrapolated gravitational potential at the current epoch ($\mathrm{a}=1$). The tensor ψ_{mn}, directly related to the strain tensor $\mathcal{E}_{\mathrm{mn}} = D(t)\psi_{\mathrm{mn}}$, describes the deformation of the mass element,

$$\begin{aligned}\psi_{\mathrm{mn}} \;=\; \frac{2}{3a^3\Omega H^2}\;\frac{\partial^2\tilde{\Phi}}{\partial q_m\,\partial q_n} \;&=\; \frac{2}{3\Omega H^2 a}\Big(\;\tilde{T}_{\mathrm{mn}} \;+\; \frac{1}{2}\Omega H^2\;\tilde{\delta}\,\delta_{\mathrm{mn}}\;\Big) \\ &=\; \frac{2}{3\Omega_0 H_0^2}\,\tilde{T}_{\mathrm{mn},0} \;+\; \frac{1}{3}\tilde{\delta}_0\,\delta_{\mathrm{mn}}\end{aligned} \tag{56}$$

The relation establishes the intimate connection between the deformation of an object and the *tidal shear field* T_{mn}, expressed in terms of the *linearly extrapolated* primordial values of these quantities, $\tilde{T}_{\mathrm{mn}}$ and $\tilde{\delta}$. These evolve according to $\tilde{\delta}(t) \propto D(t)$ and $\tilde{T}_{\mathrm{mn}} \propto D/a^3$. On the basis of this relation we immediately see that the (linearly extrapolated) tidal shear field $\tilde{T}_{\mathrm{mn}}$ is directly related to the traceless strain tensor $\mathcal{E}'_{\mathrm{mn}}$,

$$\tilde{T}_{\mathrm{mn}}(t) \;=\; 4\pi G\rho_{\mathrm{u}}(t)\,\left\{\mathcal{E}_{\mathrm{mn}} - \frac{1}{3}\tilde{\delta}\,\delta_{\mathrm{mn}}\right\} \;=\; 4\pi G\rho_{\mathrm{u}}(t)\,\mathcal{E}'_{\mathrm{mn}}\,. \tag{57}$$

Anisotropic Zel'dovich Collapse

The resulting (mildly nonlinear) local density evolution is entirely determined by the eigenvalues λ_1, λ_2 and λ_3 of the deformation tensor ψ_{mn}, ordered by $\lambda_3 \geq \lambda_2 \geq \lambda_1$),

$$\begin{aligned}\frac{\rho(\mathbf{x},t)}{\rho_{\mathrm{u}}} \;=\; \left\|\frac{\partial\mathbf{x}}{\partial\mathbf{q}}\right\|^{-1} \;&=\; \Big\|\delta_{\mathrm{mn}} - D(t)\psi_{\mathrm{mn}}\Big\|^{-1} \\ &=\; \frac{1}{[1-D(t)\lambda_1][1-D(t)\lambda_2][1-D(t)\lambda_3]}\,,\end{aligned} \tag{58}$$

where $\rho(\mathbf{x},t)$ is the local density at time t and $\rho_{\mathrm{u}}(t)$ the global (FRW) cosmic density. Dependent on whether one or more of the eigenvalues $\lambda_i > 0$, the feature will collapse along one or more directions. The collapse will proceed along a sequence of three stages. First, collapse along the direction of the strongest deformation λ_3. If also the second eigenvalue is positive, the object will contract along the second direction. Total collapse will occur only if $\lambda_1 > 0$.

The time sequence of four frames in Fig. 10 portraits the success, and shortcomings, of the Zel'dovich scheme. The four frames reveals the gradual morphological procession along *pancake* and *filamentary* stages. A comparison with the results of full-scale N-body simulations shows that in particular at early structure formation epochs the predicted Zel'dovich configurations are accurately rendering the nonlinear matter configurations. The spatial configurations predicted by the Zel'dovich approximation form a reasonably accurate approximation to the linear and mildly nonlinear phases of structure formation. The approximation breaks down when the orbits of migrating matter elements start to cross. Towards this phase the linearly extrapolated gravitational field configuration no longer forms a reasonable reflection of the genuine nonlinear gravitational field. The self-gravity of the emerging structures becomes so strong that the initial "ballistic" motion of the mass elements will get seriously altered, redirected and slowed down.

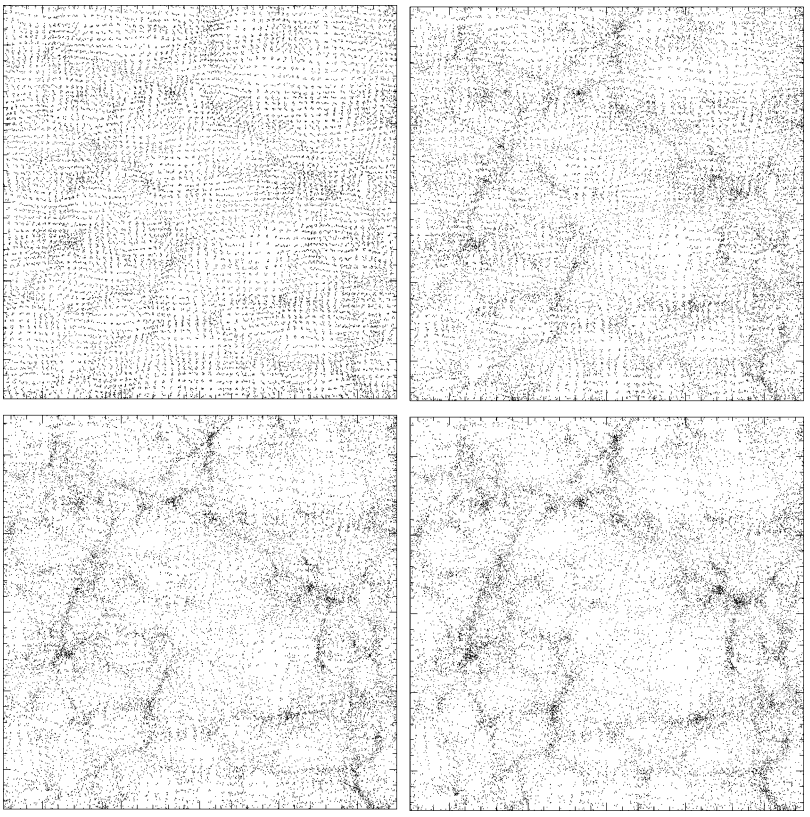

Fig. 10. Zel'dovich displaced particle distributions inferred from a unconstrained random realization of a primordial matter distribution for a SCDM cosmological scenario in a $50\,h^{-1}\,\mathrm{Mpc}$. Time sequence from top left to bottom right, frames corresponding to cosmic epochs $a = 0.10, 0.15, 0.20$ and 0.25

4.4 Ellipsoidal Collapse

Full-scale gravitational N-body simulations, and/or more sophisticated approximations, are necessary to deal self-consistently with more advanced nonlinear stages. While the Zel'dovich approximation is relatively accurate in describing the large-scale "background" induced deformation of mass elements, the internal evolution of a mass element quickly assumes a highly nonlinear character and will strongly amplify the externally induced anisotropic shape. Aspects of the subsequent evolution and anisotropic collapse can be reasonably approximated by the *homogeneous ellipsoid model*.

Quintessential is the observation that gravitational instability not only involves the runaway gravitational collapse of any cosmic overdensity, but that it has the additional basic attribute of *inevitably amplifying any slight initial asphericity during the collapse*.

The Ellipsoidal Approximation

The *Homogeneous Ellipsoidal Model* assumes a mass element to be a region with a triaxially symmetric ellipsoidal geometry and a homogeneous interior density, embedded within a uniform background density $\rho_{\rm u}$.

The early work by Icke [37, 38] elucidated the key aspects of the evolution and morphology of homogeneous ellipsoids within an expanding FRW background Universe, in particular the self-amplifying effect of a collapsing and progressively flattening isolated ellipsoidal overdensity. Translating the formalism of Lynden-Bell [54] and Lin et al. [53] to a cosmological context he came to the conclusion that flattened and elongated geometries of large scale features in the Universe should be the norm. White & Silk [88] managed to provide an elegant analytic approximation for the evolution of the ellipsoid that is remarkably accurate. However, these early studies did not reduce, as they should, to the Zel'dovich approximation in the linear regime. Bond & Myers [17], and Eisenstein & Loeb [26] emphasized that this was because they either ignored any external influences or because they did not include the effects of the external tidal (quadrupolar) influences self-consistently. Once these effects are appropriately included the resulting ellipsoidal collapse model is indeed self-consistent (see also the recent detailed study of Desjacques [24] of the environmental influence on ellipsoidal collapse).

For moderately evolved structures such as a Megaparsec (proto)cluster the ellipsoidal model represents a reasonable approximation at and immediately around the density peak. In the case of highly collapsed objects like galaxies and even clusters of galaxies it will be seriously flawed. One dominant aspect it fails to take into account are the all-important small-scale processes related to the hierarchical substructure and origin of these objects. Nonetheless, the concept of homogeneous ellipsoids has proven to be particularly useful when seeking to develop approximate yet advanced descriptions of the distribution

of virialized cosmological objects within hierarchical scenarios of structure formation [17, 72, 75].

In many respects the homogeneous model is a better approximation for underdense regions than it is for overdense ones. Overdense regions contract into more compact and hence steeper density peaks, so that the area in which the ellipsoidal model represents a reasonable approximation will continuously shrink. By contrast, for voids we find that the region where the approximation by a homogeneous ellipsoid is valid grows along with the void's expansion. While voids expand their interior gets drained of matter and develops a flat "bucket-shaped" density profile: the void's natural tendency is to evolve into expanding regions of a nearly uniform density. The approximation is restricted to the interior and fails at the void's outer fringes because of its neglect of the domineering role of surrounding material, such as the sweeping up of matter and the encounter with neighbouring features.

Ellipsoidal Gravitational Potential

The model describes the evolution of a homogeneous ellipsoidal region with a triaxially symmetric geometry, specified by its principal axes $C_1(t)$, $C_2(t)$ and $C_3(t)$. The ellipsoid has a uniform matter density $\rho(t)$, and density excess $\delta(t)$.

In the presence of an external potential contribution the total gravitational potential $\Phi^{(\mathrm{tot})}(\mathbf{r})$ at a location $\mathbf{r} = (r_1, r_2, r_3)$ in the interior of a homogeneous ellipsoid may be decomposed into three separate (quadratic) contributions,

$$\Phi^{(\mathrm{tot})}(\mathbf{r}) \;=\; \Phi_u(\mathbf{r}) \;+\Phi^{(\mathrm{int})}(\mathbf{r}) \;+\Phi^{(\mathrm{ext})}(\mathbf{r})\,. \tag{59}$$

A necessary condition for the ellipsoidal formalism to remain self-consistent is that each of the three separate contributions retains a quadratic form. Higher order contributions, also of the external potential, are ignored. The three separate contributions are:

- *Homogeneous Cosmic Background*

The potential contribution of the homogeneous background with universal density $\rho_{\mathrm{u}}(t)$,

$$\Phi_u(\mathbf{r}) \;=\; \frac{2}{3}\pi G\rho_{\mathrm{u}}\,(r_1^2 + r_2^2 + r_3^2)\;. \tag{60}$$

- *Internal Ellipsoidal Potential*

The interior ellipsoidal potential $\Phi^{(\mathrm{int})}(\mathbf{r})$, superimposed onto the homogeneous background,

$$\Phi^{(\mathrm{int})}(\mathbf{r}) \;=\; \frac{2}{3}\pi G\rho_{\mathrm{u}}\,\delta(t)\,(r_1^2 + r_2^2 + r_3^2) \;+\; \frac{1}{2}\sum_{m,n} T^{(\mathrm{int})}_{\mathrm{mn}}\, r_m r_n\,,$$

in which $T^{(\mathrm{int})}_{\mathrm{mn}}$ are the elements of the traceless internal tidal shear tensor. The quadratic expression for $\Phi^{(\mathrm{int})}$ assumes a simplified form in the coordinate system defined by the principal axes of the ellipsoid.

$$\Phi^{(\rm int)}(\mathbf{r}) \;=\; \pi G\rho_{\rm u}\,\delta\,\sum_m \alpha_{\rm m} r_{\rm m}^2\,, \tag{61}$$

where the coefficients $\alpha_{\rm m}(t)$ are

$$\alpha_{\rm m}(t) \;=\; \mathcal{R}_1(t)\mathcal{R}_2(t)\mathcal{R}_3(t)\int_0^\infty \frac{{\rm d}\lambda}{(\mathcal{R}_{\rm m}^2(t)+\lambda)\prod_{n=1}^3\left(\mathcal{R}_{\rm n}^2(t)+\lambda\right)^{1/2}}\,. \tag{62}$$

The Poisson equation implies the α_m's obey the constraint $\sum_{m=1}^3 \alpha_m = 2$. In the case of a spherical perturbation all three α_m's are equal to $2/3$, reproducing the well-known fact that it does involve a vanishing internal tidal tensor contribution,

$$T^{(\rm int)}_{\rm mn} \;=\; \frac{\partial^2\Phi^{(\rm int)}}{\partial r_m\,\partial r_n} - \frac{1}{3}\nabla^2\Phi^{(\rm int)}\;\delta_{\rm mn} \;=\; 2\pi G\,\rho_{\rm u}\,\delta(t)\,\left(\alpha_m - \frac{2}{3}\right)\,\delta_{\rm mn}\,.$$

- *External Tidal Influence*

The external gravitational potential $\Phi^{(\rm ext)}$. Assuming that the external tidal field does not vary greatly over the expanse of the ellipsoidal mass element, we may limit the external contribution to its quadrupolar components,

$$\Phi^{(\rm ext)}(\mathbf{r}) \;=\; \frac{1}{2}\sum_{m,n} T^{(\rm ext)}_{\rm mn}\,r_m r_n\,. \tag{63}$$

$T^{(\rm ext)}_{mn}$ are the components of the external (traceless) tidal shear tensor. By default the latter is limited to its traceless contribtuion, the corresponding (background) density is implicitly included in the (total) internal density, $\rho_u(t)(1+\delta(t))$.

The external field is taken to be the smooth large-scale tidal field $T_{\rm b,mn}$. The latter is directly related to the traceless large scale (background) strain tensor (57), with eigenvalues $\tau_{\rm m}$ given by (see (71)),

$$\tau_{\rm m} \;=\; 4\pi G\rho_{\rm u}(t)\,\lambda'_{\rm vm}(t)\,. \tag{64}$$

where λ'_{vm} are the eigenvalues of the background anisotropic strain tensor $\mathcal{E}'_{pk,\rm ij}$ at the location of the mass peak.

Ellipsoidal Evolution

The anisotropy of an initially spherically symmetric matter element in the primordial cosmic matter distribution is a direct effect of the external tidal force field. As a result the principal axes of the configuration are the ones defined by the external tidal tensor $T^{(\rm ext)}_{\rm mn}$. Both the external large-scale tidal forces inducing the anisotropic collapse and the resulting internal one do strongly enhance the anisotropic shape of the ellipsoid.

The evolution of the ellipsoid is specified by three scale factors $\mathcal{R}_{\rm i}$, one for each of the three principal axes. The boundary of the ellipsoid and the overdensity evolve as

$$C_i(t) \,=\, \mathcal{R}_{\rm i}(t)\, R_{pk}\,, \qquad \delta(t) \,=\, \frac{a^3}{\mathcal{R}_1\mathcal{R}_2\mathcal{R}_3} \,-\, 1\,. \tag{65}$$

in terms of the initial (Lagrangian) radius R_{pk}. The evolution of the scale factors $\mathcal{R}_{\rm i}$ are determined by the gravitational acceleration along each of the principal axes (see (59)). Including the influence of the cosmological constant Λ, this translates into

$$\frac{d^2\mathcal{R}_{\rm m}}{{\rm d}t^2} \,=\, -4\pi G\rho_{\rm u}(t)\,\left[\frac{1+\delta}{3} \,+\, \frac{1}{2}\,\left(\alpha_m - \frac{2}{3}\right)\,\delta\right]\,\mathcal{R}_{\rm m} \,-\, \tau_{\rm m}\,\mathcal{R}_{\rm m} \,+\, \Lambda R_m\,. \tag{66}$$

with $\alpha_{\rm m}(t)$ the ellipsoidal coefficients specified by the integral (62) and τ_m the eigenvalue of the external (large-scale) tidal shear tensor $T^{\rm (ext)}_{\rm mn}$.

The collapse of the three axes of the ellipsoid will happen at different times. The shortest axis will collapse first, followed by the intermediate axis and finally by the longest axis. The shortest axis will collapse considerably faster than that of the equivalent spherically evolving perturbation while full collapse along all three axis will be slower as the longest axis takes more time to reach collapse. In fact, the longest axis may not collapse at all. An illustration of this behaviour can be found in Fig. 11. It shows the evolution of a slightly overdense *isolated* ellipsoid, with initial axis ratios $a_1 : a_2 : a_3 = 1 : 0.9 : 0.8$, embedded in a background Einstein-de Sitter Universe. Quantitatively the expansion and subsequent contraction of each of the three axes can be followed in Fig. 12. The superimposed blue curve represents the evolution of the equivalent spherical overdensity. The righthand frame shows that this development involves a continuous decrease of both axis ratios.

4.5 Ellipsoidal Collapse and External Influences

In order to properly model the nonlinear collapse of the features in the *Cosmic Web* it is essential to embed the nonlinear anisotropic collapse of mass elements within the large-scale environment. A proper approximation, following Bond & Myers [17], is that of assuming the large-scale tidal influence to be largely linear and assuring that the initial conditions for the ellipsoid asymptotically approach the Zel'dovich equation,

$$\begin{aligned} \mathcal{R}_{\rm m}(t_{\rm i}) \,&=\, a(t_{\rm i})\,\{1 \,-\, D(t_i)\lambda_{\rm m}\}\,, \\ \frac{{\rm d}\mathcal{R}_{\rm m}}{{\rm d}t}(t_{\rm i}) \,&=\, H(t_{\rm i})\mathcal{R}_{\rm m}(t_{\rm i}) \,-\, a(t_{\rm i})H(t_{\rm i})f(\Omega_{\rm i})\,D(t_{\rm i})\lambda_{\rm m}\,, \end{aligned} \tag{67}$$

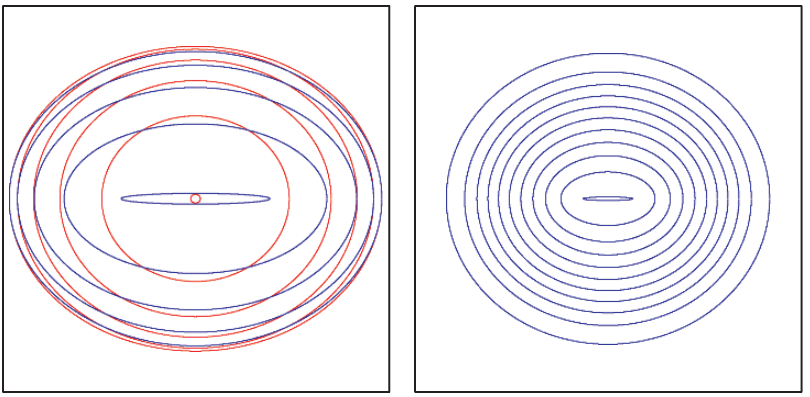

Fig. 11. The evolution of an overdense homogeneous ellipsoid, with initial axis ratio $a_1 : a_2 : a_3 = 1.0 : 0.9 : 0.9$, embedded in an Einstein-de-Sitter background Universe. The two frames show a time sequel of the ellipsoidal configurations attained by the object, starting from a near-spherical shape, initially trailing the global cosmic expansion, and after reaching a maximum expansion turning around and proceeding inexorably towards ultimate collapse as a highly elongated ellipsoid. **Left:** the evolution depicted in physical coordinates. Red contours represent the stages of expansion, blue those of the subsequent collapse after turn-around. **Right:** the evolution of the same object in comoving coordinates, a monologous procession through ever more compact and more elongated configurations

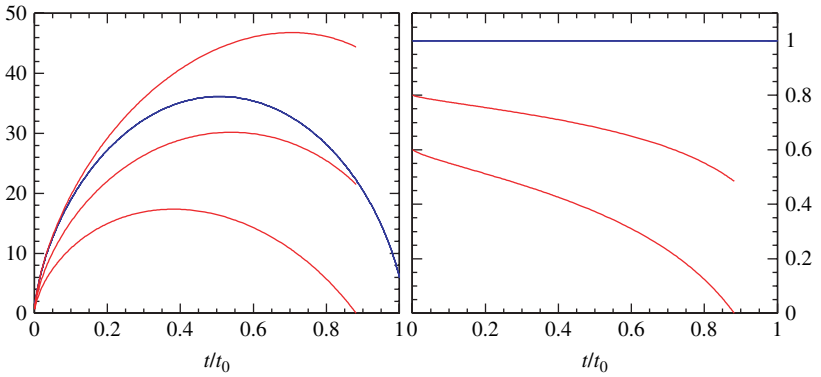

Fig. 12. The evolution of an overdense homogeneous ellipsoid, with initial axis ratio $a_1 : a_2 : a_3 = 1.0 : 0.8 : 0.6$, in an Einstein-de-Sitter background Universe. **Left:** expansion factors for each individual axis; **Right:** axis ratios a_2/a_1 and a_3/a_1. The ellipsoid axes are depicted as red curves. For comparison, in blue, the evolution of an equivalent homogenous spherical overdensity

in which $\lambda_{\rm m}$ are the eigenvalues of the Zel'dovich deformation tensor $\psi_{\rm mn}$, and $D(t)$ is the linear density growth factor and $f(\Omega)$ the corresponding linear velocity factor [62].

By using the implied relation between the eigenvalues of the external tidal tensor $\tau_{\rm m}$ and the large-scale tidal strain tensor $\mathcal{E}_{mn}$ (64) the following equation of motion is obtained,

$$\frac{d^2\mathcal{R}_{\rm m}}{{\rm d}t^2} \;=\; -4\pi G\rho_{\rm u}(t)\,\left[\frac{1+\delta}{3} \;+\; \frac{1}{2}\,(\alpha_m - \frac{2}{3})\,\delta \;+\; \lambda'_{\rm vm}\right]\mathcal{R}_{\rm m} \;+\; \Lambda R_m. \quad (68)$$

While the smooth large-scale tidal field induces the anisotropic collapse of the mass element, the subsequent nonlinear evolution differs increasingly from the predictions of the linear Zel'dovich formalism (58). As can be seen in Fig. 13 for nearly all conceivable (external) tidal shear ellipticities the nonlinear ellipsoidal collapse involves a considerably faster collapse along all three axes of an ellipsoid than that following from the Zel'dovich approximation (58). Only for extremely anisotropic tidal configurations the Zel'dovich formalism would find the same collapse time for the longest axis of the mass element.

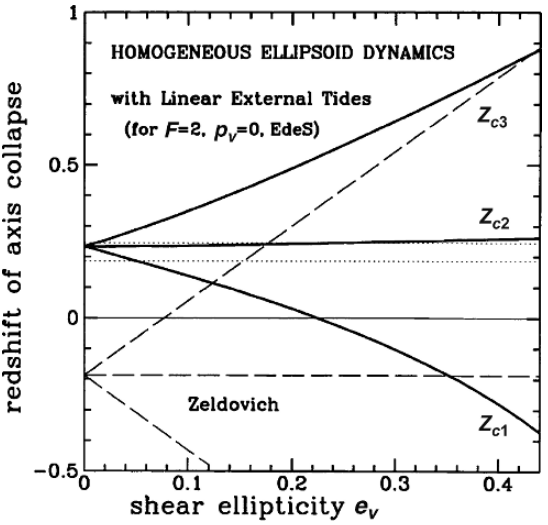

Fig. 13. The collapse redshifts for the three ellipsoidal axes of the initial external tidal shear ellipticity e_v, assuming zero prolaticity p_v, a linear extrapolated density $\delta_0 = 2$ and a linear external tide approximation (68). The dashed curve shows how poorly the Zel'dovich approximation fares: only for the extreme elongations does it get the collapse redshift along the third axis right, while it is far off for the other two directions. Also shown, by dotted lines, are the redshifts at which an equivalent spherical overdensity reaches overdensity 170 (*upper dotted line*) and complete collapse (*lower dotted line*). From Bond & Myers [17]. Reproduced with permission of AAS

4.6 Primordial Structural Morphology

The values of the (Zel'dovich) deformation eigenvalues λ_{v1}, λ_{v2} and λ_{v3} basically determine the (asymptotic) morphology of the resulting features, roughly along the lines specified in Table 1: they function as cosmic shape parameters.

To get insight into the prevailing morphology in the cosmic matter distribution it is necessary to assess the statistical and spatial distribution of the shear eigenvalues. This will determine the overall morphology and geometry of the cosmic density field at the "quasi-linear" stage – i.e. the prominence of mutually interconnected flattened structures, denser elongated filaments and dense compact clumps.

The first assessment of the statistical properties of the deformation tensor in a primordial Gaussian random density fluctuation field is the seminal study by Doroshkevich [25]. He derived the (unconditional) pdf for the eigenvalues λ_1, λ_2 and λ_3,

$$P(\lambda_1,\lambda_2,\lambda_3) \;\sim\; (\lambda_1-\lambda_2)(\lambda_1-\lambda_3)(\lambda_2-\lambda_3) \times\; \exp\left\{-\frac{15}{2\sigma^2}\left[\lambda_1^2+\lambda_2^2+\lambda_3^2-\frac{1}{2}(\lambda_1\lambda_2+\lambda_1\lambda_3+\lambda_2\lambda_3)\right]\right\}. \tag{69}$$

This yields a probability of 8% that all of the eigenvalues are negative, $\lambda_1 < \lambda_2 < \lambda_3 < 0$, predisposing the formation of a void. The probability that matter elements have one or more positive eigenvalues is filament-dominated weblike morphology is the generic outcome during the moderate quasi-linear evolutionary phase for any scenario with primordial Gaussian perturbations marked by relatively strong perturbations on large scales. The signs of the eigenvalues will determine the (asymptotic) local geometry along the lines specified in Table 1.

For the purpose of understanding the geometry of large scale structure we also should take note of the fact that the values of the deformation tensor eigenvalues are directly constrained by the local density,

Table 1. Asymptotic morphology: deformation eigenvalue conditions for different asymptotic structural morphologies in the Cosmic Web

Structure	Eigenvalue signatures
Peak	$\lambda_1>0\ ;\ \lambda_2>0\ ;\ \lambda_3>0$
Filament	$\lambda_1>0\ ;\ \lambda_2>0\ ;\ \lambda_3<0$
Sheet	$\lambda_1>0\ ;\ \lambda_2<0\ ;\ \lambda_3<0$
Void	$\lambda_1<0\ ;\ \lambda_2<0\ ;\ \lambda_3<0$

$$\tilde{\delta} \;=\; (\lambda_{v1} + \lambda_{v2} + \lambda_{v3})\,, \tag{70}$$

in which $\tilde{\delta}$ is the (linearly extrapolated) initial density contrast. In other words, when we see a supercluster or other interesting feature we should assess the *conditional* probability of the shape parameters for the relevant range of density values. To this end it is helpful to introduce the shear ellipticity e_v and shear prolateness p_v (see Bardeen et al. [6], Bond & Myers [17] 1996a),

$$e_v \;=\; \frac{\lambda_{v1} - \lambda_{v3}}{2\sum_i \lambda_{vi}}\,, \qquad\qquad p_v \;=\; \frac{\lambda_{v1} - 2\lambda_{v2} + \lambda_{v3}}{2\sum_i \lambda_{vi}}\,. \tag{71}$$

By implication e_v and p_v are constrained to $e_v \geq 0$ and $-e_v \leq p_v \leq e_v$. The evolution of a patch is spherically symmetric when the shear is isotropic ($\lambda_{v3} = \lambda_{v2} = \lambda_{v1}$), i.e. when $e_v = p_v = 0$. When the collapse is predominantly along one axis ($\lambda_{v3} > 0, \lambda_{v2} \sim \lambda_{v1} < 0$), the initial evolution is towards a classical pancake by $e_v = p_v$. When a second axis is also collapsing ($\lambda_{v3} \sim \lambda_{v2} > 0, \lambda_{v1} < 0$) the result is filamentary, $e_v = -p_v$. In other words, extreme sheet-like structures would have $p_v \approx e_v$, extreme filaments $p_v \approx -e_v$.

Via the quantities e_v and p_v we may get an idea of the prominence of filamentary and sheetlike structures in the cosmic matter distribution by assessing their conditional distribution in the primordial density field for a given $\delta = \nu_f\sigma$. The combined statistical distribution $P(e_v, p_v|\nu_f)$ of e_v and p_v and of the prolaticity, $P(p_v|\nu_f)$, at an arbitrary field location with density are Wadsley & Bond [87] and Bond [14],

$$\begin{aligned} P(\{\lambda_{v1}, \lambda_{v2}, \lambda_{v3}\}|\nu_f) \;&=\; P(e_v, p_v|\nu_f) \\ &=\; \frac{225\sqrt{5}}{\sqrt{2\pi}}\, e_v(e_v^2 - p_v^2)\, \nu_f^3\, e^{-15(\nu_f e_v)^2/2 \,-\, 5(\nu_f p_v)^2/2}\; \mathrm{d}e_v\; \mathrm{d}p_v\,. \end{aligned} \tag{72}$$

Figure 14 shows the iso probability contours of $P(e_{\rm v}, p_{\rm v}|\nu_f)$ for a set of 6 different ν_f values. It manifestly demonstrates the distinct tendency of overdense regions, in particularly those of moderate density, to be *filamentary*: $p_{\rm v} < 0$ or, equivalently, eigenvalue signature $(\lambda_1, \lambda_2, \lambda_3) = (- + +)$. The figure also underlines the fact that higher peaks tend to be more spherical. This may be quantitatively appreciated from the corresponding expectation values for the the ellipticity and prolaticity of an arbitary field patch with local density $\delta = \nu_f\sigma$ [14],

$$\begin{aligned} \langle e_v|\nu_f, \mathrm{field}\rangle \;&\approx\; 0.54\nu_f^{-1}\,; \qquad \Delta e_v \;\approx\; 0.18\nu_f^{-1}\,, \\ \langle |p_v||\nu_f, \mathrm{field}\rangle \;&\approx\; 0.18\nu_f^{-1}\,; \qquad \Delta p_v \;\approx\; 0.22\nu_f^{-1}\,, \end{aligned} \tag{73}$$

which express the strongly declining nature of ellipticity and prolateness as a function of patch density.

The gross properties of the Cosmic Web may therefore already be found in the primordial density field. In this light it is particularly illuminating to study

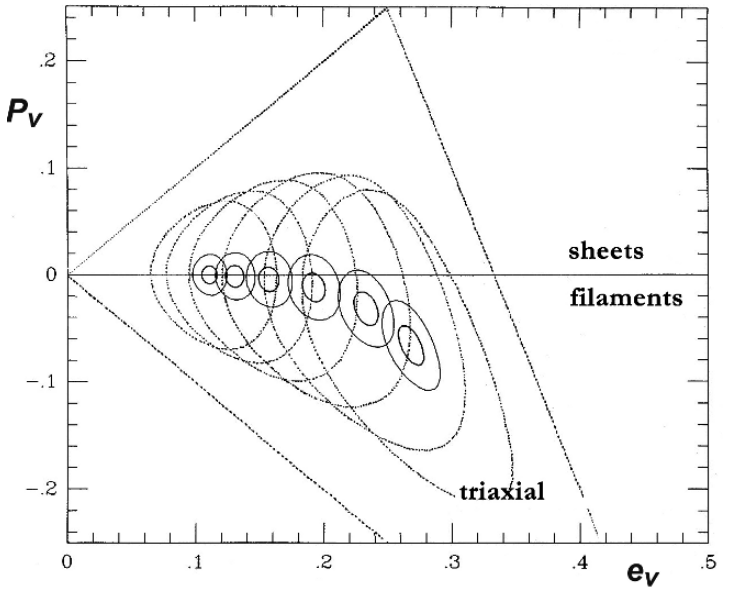

Fig. 14. The 95, 90 and 50% contours of the conditional probability for ellipticity e_v and prolateness p_v subject to the constraint of a given field density value $\nu = \delta/\sigma$. The figure demonstrates that even for high ν the shapes are triaxial and that for lower density values there is a tendency towards filamentary configurations

the distribution of the deformation eigenvalue signatures as a function of density threshold $\nu_f = \delta_f/\sigma$. Figure 15 looks at two aspects of this question [66]. The dependence of structural morphology on the density threshold is given by the probability of the eigenvalue signature on the threshold $\delta = \nu\sigma$, $P(\text{sign}|\delta)$. The left panel of Fig. 15 shows that for Gaussian fields at overdensties above a critical $\delta = 1.56\sigma$ one encounters predominantly spherical-like mass concentrations $(+++)$. By contrast, at lower density contrast $0 < \delta < 1.56\sigma$, most of the initial density enhancements are in elongated filamentary bridges $(-++)$. Planar configurations $(--+)$ are less likely for any positive overdensities $\delta > 0$. The related quantity $P(\delta|\text{sign})$ gives us the density distribution within different types of structure. While the average density of the filaments in the initial configuration is equal to $\delta = 0.6\sigma$, it is the $\delta \sim 1.5 - 2\sigma$ excursions which are precursors of the rare prominent filaments. By contrast, rare planar membrane-like configurations are expected only at lower overdensities of $\delta \sim 0.5 - 1\sigma$. Mean densities for the given shear signatures are $\langle\delta\rangle \approx 1.66\sigma\,, 0.6\sigma\,, -0.6\sigma$, with dispersion $\Delta\delta \approx 0.55\sigma$.

4.7 Evolving Filamentary Morphology

Evidently, the primordial density field analysis only provides a superficial impression of the emerging morphology of the Cosmic Web. What it does

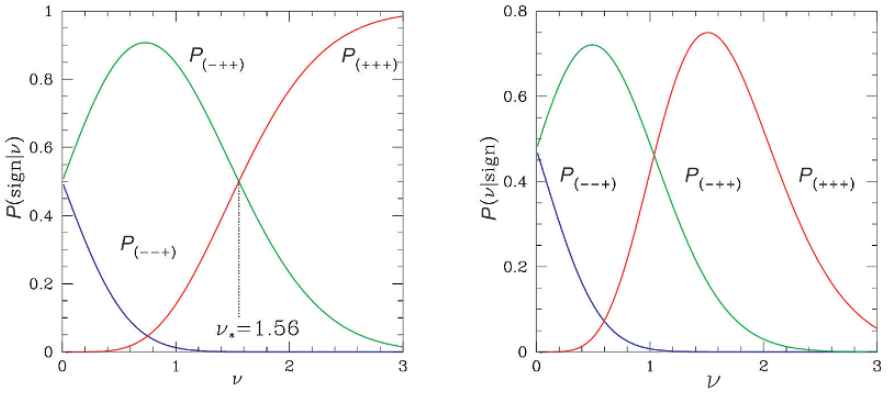

Fig. 15. Left panel: probability of the eigenvalue signature given the overdensity threshold $P(\text{sign}|\nu)$, $\nu = \delta/\sigma$. **Right panel:** density distribution given the signature type of shear tensor, $P(\nu|\text{sign})$. From: Pogosyan et al. [66]

emphasize, and strongly so, is the prevalence of proto-filaments and proto-clusters in the primordial density field.

This impression will only become more pronounced as nonlinear evolution sets in. The salient filamentary nature of the nonlinear mass distribution seen in large N-body simulations (see e.g. Fig. 1) can already be noticed when following the early nonlinear evolution by means of the Zel'dovich mapping (54). A telling illustration of this can be seen in Fig. 16. The left panel shows an initial linear CDM overdensity field δ_L smoothed on a Gaussian scale $R_b = 3.5\,\mathrm{h}^{-1}\,\mathrm{Mpc}$, with $\sigma_\rho = 0.65$. The chosen density threshold is $\delta_L = 1\sigma_\rho$, the level at which $\delta_L(\mathbf{r})$ percolates. The right panel shows $\delta_Z(\mathbf{r}, t)$, the overdensity of the resulting Zel'dovich map at a contour threshold $\delta_Z = 2$, just above where percolation occurs.

The Zel'dovich map in Fig. 16, evolved to $\sigma_8 = 0.7$, clearly shows the dominant filamentary morphology. It disproves the conventional tenet of pancakes representing the dominant overdensity features. Also, it underlines the observation that the prominent filaments already existed in an embryonic – and fattened – form in the initial conditions. As the nonlinear evolution proceeds the cluster regions will collapse even further and occupy even less volume. This will enhance the filamentary character of the cosmic matter distribution even further.

Having argued and illustrated the principal filamentary nature of the Cosmic Web, largely on the basis of a local evaluation of the deformation eigenvalues, we need to assess the apparent coherence of these weblike structures and their mutual relationship. Their overall geometry and topology can be understood by adressing the relationship between the local values of the deformation tensor, responsible for the local morphology, and the global density field.

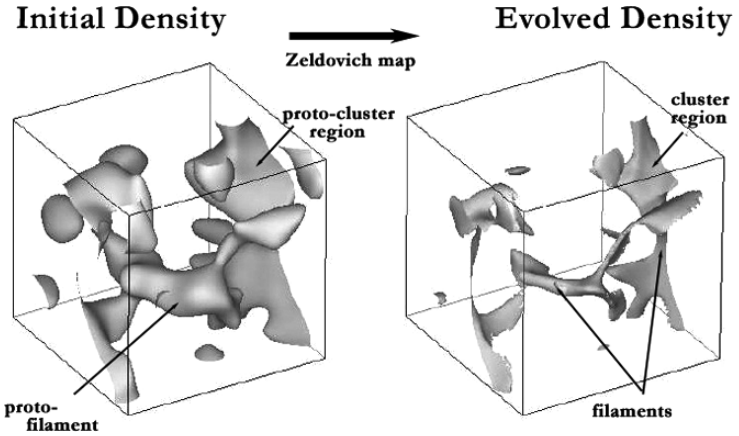

Fig. 16. Cosmic Web and Clusters. (Mean) constrained density field reconstructions $\langle \delta_L | 20peaks \rangle$ on the basis of the 20 most massive cluster peaks (patches) in a CDM density field in a $(50\,\mathrm{h}^{-1}\,\mathrm{Mpc})^3$ box with periodic boundary conditions. **Lefthand:** initial linear CDM overdensity field $\delta_L(\mathbf{r})$, smoothed on a Gaussian scale $R_G = 3.5\,\mathrm{h}^{-1}\,\mathrm{Mpc}$ with (iso)density threshold level $\delta_L = 1\sigma_\rho$, with $\sigma_\rho = 0.65$, the level at which δ_L percolates. The location, size and shape of the cluster patches is indicated by means of the black ellipsoids, whose size is proportional to the peak scale R_{pk} and orientation defined by the shear tensor orientation. **Righthand:** the corresponding Zel'dovich map density field δ_Z of the smoothed initial conditions at a contour threshold $\delta_Z = 2$. Based on Bond et al. [18]. Reproduced with permission of Nature

This makes it necessary to turn to the concept of conditional multi-point correlation functions in Lagrangian space (also see Bond [15]), i.e. the statistically averaged density and displacement fields subject to various constraint on the (tidal) shear at multiple points in the cosmic volume. The mathematical language needed for evaluating the implied "protoweb" in the initial density field is that of *constrained random field* theory, first introduced by Bertschinger [10]. In the next Sect. 4.8 we will describe this formalism in some necessary detail.

4.8 Constrained Random Field Formalism

A major virtue of the *constrained random field* construction technique [10, 35, 73, 84] is that it offers the instrument for translating locally specified quantities to the corresponding implied global matter distribution.

Bertschinger [10] described how a set Γ of functional field constraints $C_i[f] = c_i$, $(i = 1, \ldots, M)$ of a Gaussian random field $f(\mathbf{r}, t)$ would translate into field configurations for which these constraints would have the specified values c_i. Any such *constrained field realization* f_c can be written as the sum of a *mean field* $\bar{f}(\mathbf{x}) = \langle f(\mathbf{x}) | \Gamma \rangle$, the ensemble average of all field realizations obeying the constraints, and a *residual field* $F(\mathbf{x})$, embodying the field

fluctuations characterized and specified by the power spectrum $P(k)$ of the particular cosmological scenario at hand,

$$f_c(\mathbf{x}) \;=\; \bar{f}(\mathbf{x}) \;+\; F(\mathbf{x}) \tag{74}$$

Bertschinger [10] showed the specific dependence of the mean field on the *nature* $C_i[f]$ of the constraints as well as their *values* c_i. In essence the mean field can be seen as the weighted sum of the field-constraint correlation functions $\xi_i(\mathbf{x})$,

$$\xi_i(\mathbf{x}) \;\equiv\; \langle f\, C_i \rangle \tag{75}$$

(where we follow the notation of Hoffman & Ribak [35]). Each field-constraint correlation function encapsulates the repercussion of a specific constraint $C_i[f]$ for a field $f(\mathbf{x})$ throughout the sample volume $\mathcal{V}_s$. For example, the field-constraint correlation function for a constraint on the peculiar velocity or gravity is a dipolar pattern, while a tidal constraint T_{ij} effects a quadrupolar configuration (see van de Weygaert & Bertschinger [84]). The weights for each of the relevant $\xi_i(\mathbf{x})$ are determined by the value of the constraints, c_m, and their mutual cross-correlation $\xi_{mn} \equiv \langle C_m C_n \rangle$,

$$\bar{f}(\mathbf{x}) \;=\; \xi_i(\mathbf{x})\, \xi_{ij}^{-1}\, c_j \,. \tag{76}$$

In practice, it is usually beneficial to evaluate the constraint correlation function $\xi_i(\mathbf{r}$, ξ_{ij} and the mean field in Fourier space. For a linear cosmological density field with power spectrum $P(k)$ we have

$$\begin{aligned} \xi_i(\mathbf{r}) \;&=\; \int \frac{\mathrm{d}\mathbf{k}}{(2\pi)^3}\, \hat{H}_i(\mathbf{k})\, P(k)\, e^{-i\mathbf{k}\cdot\mathbf{x}} \\ \xi_{ij} \;&=\; \int \frac{\mathrm{d}\mathbf{k}}{(2\pi)^3}\, \hat{H}_i^*(\mathbf{k})\, \hat{H}_j(\mathbf{k})\, P(k) \end{aligned} \tag{77}$$

with $\hat{H}_i(\mathbf{k})$ the constraint i's kernel (the Fourier transform of constraint $C_i[f]$) and c_j the value of this constraint.

The additional generation of the residual field F is a nontrivial exercise: the specified constraints translate into locally fixed phase correlations. This renders a straightforward random phase Gaussian field generation procedure unfeasible: the amplitude of the residual field is modified by the local correlation with the specified constraints. Hoffman & Ribak [35] pointed out that for a Gaussian random field the sampling is straightforward and direct, which greatly facilitated the application of CRFs to cosmological circumstances. This greatly facilitated the application of CRFs to complex cosmological issues [44, 55, 69].

Van de Weygaert & Bertschinger [84], following the Hoffman–Ribak formalism, worked out the specific CRF application for the circumstance of sets of local density peak (shape, orientation, profile) and gravity field constraints.

With most calculations set in Fourier space, the constrained field realization for a linear cosmological density field with power spectrum $P(k)$ follows from the computation of the Fourier integral

$$f(\mathbf{x}) \;=\; \int \frac{\mathrm{d}\mathbf{k}}{(2\pi)^3} \left[\hat{\tilde{f}}(\mathbf{k}) + P(k)\, \hat{H}_i(\mathbf{k})\, \xi_{ij}^{-1}\, (c_j - \tilde{c}_j) \right] \mathrm{e}^{-\mathrm{i}\mathbf{k}\cdot\mathbf{x}} \qquad (78)$$

where the tilde indicates it concerns a regular unconstrained field realization $\tilde{f}$.

One of the major virtues of the *constrained random field* construction technique is that it offers the instrument for translating locally specified quantities into the corresponding implied global matter distributions for a given structure formation scenario. In principle the choice of possible implied matter distribution configurations is infinite. Nonetheless, it gets substantially curtailed by the local matter configuration. The influence of local constraints is set by the coherence scale of matter fluctuations, a function of the power spectrum of fluctuations.

While the CRF formalism is rather straightforward for idealized linear constraints reality is less forthcoming. If the constraints are based on measured data these will in general be noisy, sparse and incomplete. Wiener filtering will be able to deal with such a situation and reconstruct the implied *mean field*, at the cost of losing signal proportional to the loss in data quality (see e.g. Zaroubi et al. [89]). A major practical limitation concerns the condition that the constrained field is Gaussian. For more generic nonlinear clustering situations the formalism is in need of additional modifications. For specific situations this may be feasible [73], but for more generic circumstances this is less obvious (however, see Jones & van de Weygaert 2008).

4.9 Shear Constraints

The Megaparsec scale tidal shear pattern is the main agent for the contraction of matter into the filaments which trace out the cosmic web (see Figs. 18 and 19). For a cosmological matter distribution the close connection between local force field and global matter distribution follows from the expression of the tidal tensor in terms of the generating cosmic matter density fluctuation distribution $\delta(\mathbf{r})$ [84]:

$$T_{ij}(\mathbf{r}) = \frac{3\Omega H^2}{8\pi} \int \mathrm{d}\mathbf{r}'\, \delta(\mathbf{r}') \left\{ \frac{3(r'_i - r_i)(r'_j - r_j) - |\mathbf{r}' - \mathbf{r}|^2\, \delta_{ij}}{|\mathbf{r}' - \mathbf{r}|^5} \right\} - \frac{1}{2}\Omega H^2\, \delta(\mathbf{r}, t)\, \delta_{ij}.$$

Constrained random field realizations immediately reveal the nature of the density field realizations $\delta(\mathbf{r})$ that would generate a tidal field T_{ij} at particular location $\mathbf{r}_0$. The effect of the local shear constraints on the density profile around a position r_0 may be seen in Fig. 17. The shape of the density contours

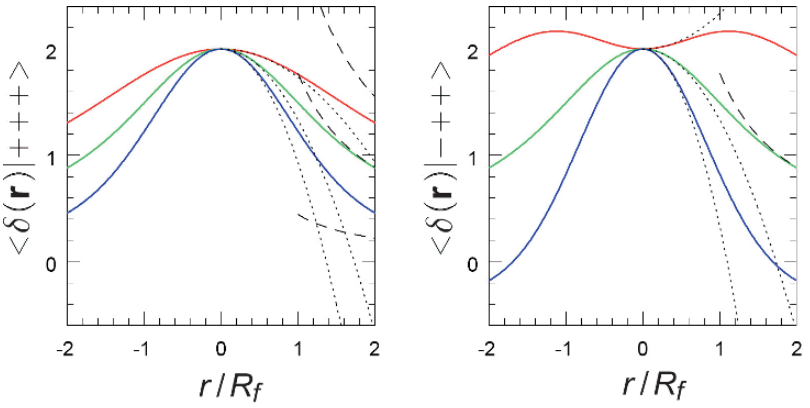

Fig. 17. Constrained primordial density field $\langle\delta(\mathbf{r})|\lambda_1,\lambda_2,\lambda_3\rangle$ as a function of distance $\mathbf{r}$ in units of the filter scale R_f, in the three eigendirections. **Left frame:** shear constraint signature $(+++)$. **Right frame:** shear constraint signature $(-++)$. The "filamentary" behaviour of the density in the neighbourhood of the point manifests itself particularly in the density profile along the x-direction (*top curve*). From: Pogosyan et al. [66]

clearly depends on the signature of the eigenvalues. The righthand frame does reveal an increase in the density along one axis while falling off along the remaining two. This is symptomatic of filamentary bridges that connect the higher density regions where the shape of the density profile is more spherical. In effect, the local shear signature defines the curvature of the density isocontours up to a distance of several filter radii R_f[2].

Pursuing the filamentary configuration implied by the specified $(-++)$ signature tidal shear, the 3-D density distribution around the location of the specified constraint is shown in Fig. 19. The specified shear tensor is oriented along the box axes. The field is Gaussian filtered on a (rather arbitrary) scale of $2\,\mathrm{h}^{-1}\,\mathrm{Mpc}$. The implied *mean field* $\bar{f}$ is shown in the 3 top panels. Each panel looks along one of the main axes. The constraint clearly works out into perfect global quadrupolar mass distribution. A representative realization of a quadrupolar (CDM) cosmic matter distribution which would induce the specified shear is shown in the second row of panels.

The corresponding maps of the tidal shear in the same region are shown in the bottom row. Included are contour maps of the total tidal field strength. Also we include bars indicating the direction and strength of the tide's compressional component[3]. Along the full length of the filament in Fig. 19

[2] The information contained in the density curvature tensor itself is much more local and less representative of the density behaviour at large distances from the constraint point.

[3] On the basis of the effect of a tidal field, we may distinguish at any one location between "compressional" and "dilational" components. Along the direction of a

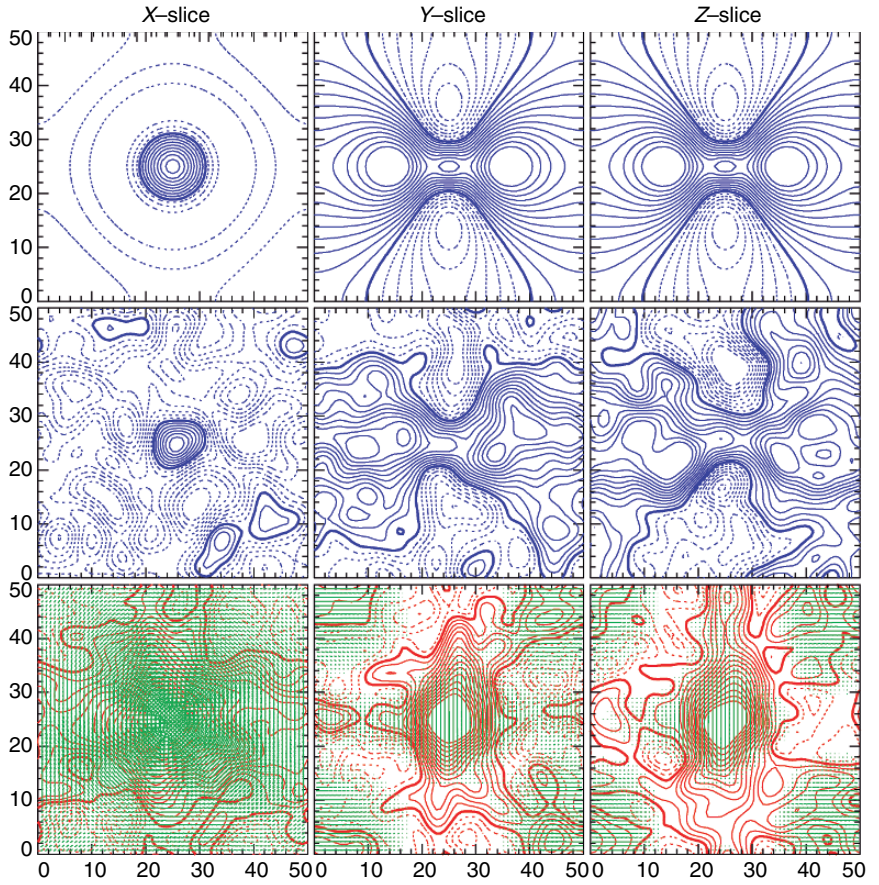

Fig. 18. Constrained field construction of initial quadrupolar density pattern in a SCDM cosmological scenario. The tidal shear constraint is specified at the box centre location, issued on a Gaussian scale of $R_G = 2\,\mathrm{h}^{-1}\,\mathrm{Mpc}$ and includes a stretching tidal component along the x- and y-axis acting on a small density peak at the centre. Its ramifications are illustrated by means of three mutually perpendicular slices through the centre. **Top row:** the "mean" field density pattern, the pure signal implied by the specified constraint. Notice the clear quadrupolar pattern in the y- and z-slice,directed along the x- and y-axis, and the corresponding compact circular density contours in the x-slice: the precursor of a filament. **Central row:** the full constrained field realization, including a realization of appropriately added SCDM density perturbations. **Bottom row:** the corresponding tidal field pattern in the same three slices. The (red) contours depict the run of the tidal field strenght $|T|$, while the (green) tidal bars represent direction and magnitude of the *compressional* tidal component in each slice (scale: $R_G = 2\,\mathrm{h}^{-1}\,\mathrm{Mpc}$). From van de Weygaert [83]

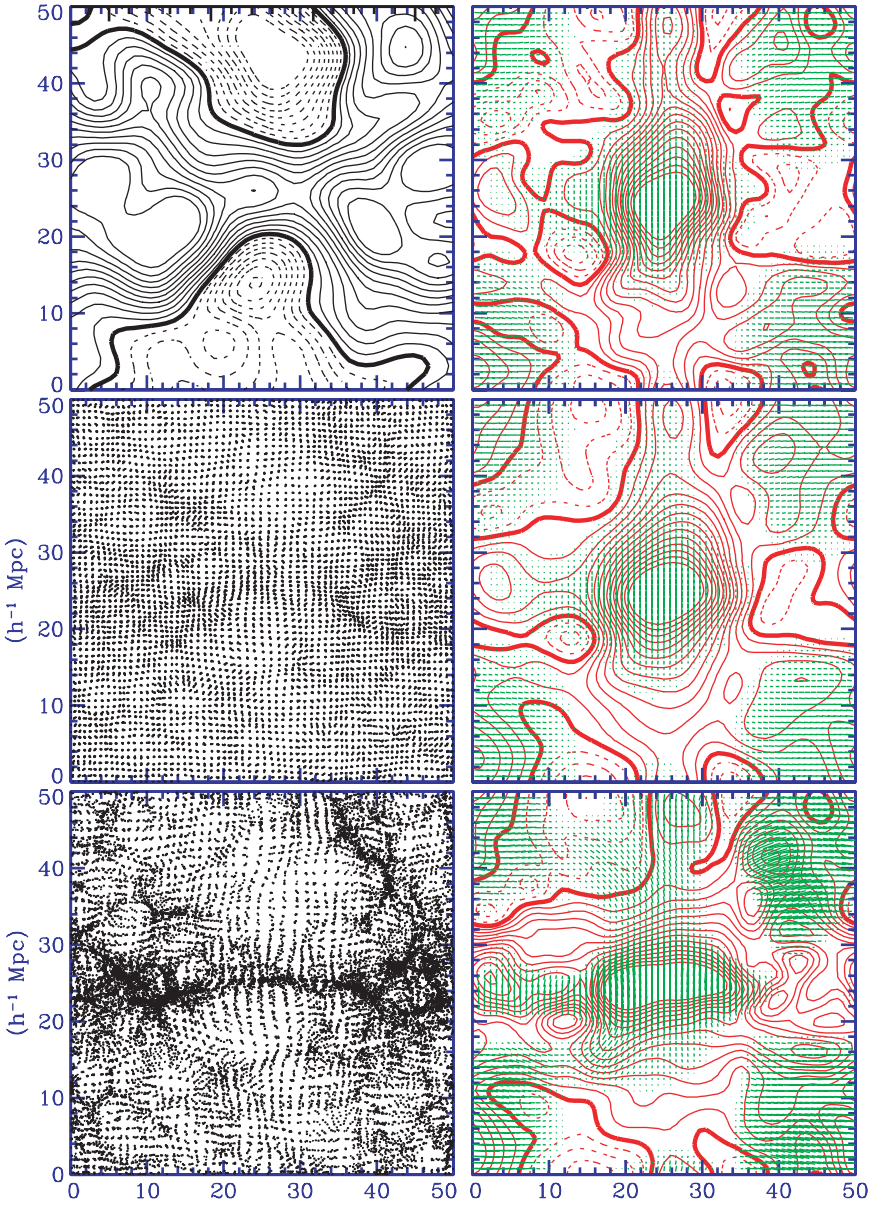

Fig. 19. The emergence of a filament in an SCDM structure formation scenario. **Lefthand column:** density/particle distribution in z-slice through the centre of the simulation box. **Righthand column:** the corresponding tidal field configurations, represented through the full tidal field strength $|T|$ contour maps (red), as well as the corresponding compressional tidal bars (scale: $R_G = 2\,\mathrm{h}^{-1}\,\mathrm{Mpc}$). From top to bottom: primordial field, $a = 0.2$ (visible emergence filament), present epoch. Note the formation of the filament at the site where the tidal forces peaked in strength, with a tidal pattern whose topology remains roughly similar. From van de Weygaert [83]

we observe a coherent pattern of strong compressional forces perpendicular to its axis.

Filaments and Peaks

The dynamical evolution in and around the (proto) filament is depicted in Fig. 19. It shows the emergence of a (CDM) filament with the density/particle distribution along the spine of the emerging filament (lefthand column) and the corresponding tidal configuration (righthand column). The top row corresponds to the primordial cosmic conditions, the central row to $a = 0.2$ and the bottom row to $a = 0.8$. At $a = 0.2$ we recognize the first vestiges of an emerging filament, at $a = 0.8$ it has indeed condensed as the most salient feature in the mass distribution. Also, we see that the filament forms along the ridge seemingly predestined by the primordial tidal configuration (Figs. 19 and 20).

The figure also clarifies the essence of the link between filaments and clusters. At the tip of the evolving filament we observe the emergence of massive cluster patches. They naturally arise in and around the overdense peaks in the primordial quadrupolar mass distribution implied by the tidal shear constraint. These overdense protoclusters were the source of the specified shear. A quadrupolar matter configuration will almost by default evolve into the canonical *cluster-filament-cluster* configuration so prominently recognizable in the observed Cosmic Web.

The two main conclusion from these observations are the embryonic presence of the weblike features in the primordial density field and the intimate link between the cluster distribution and the filigree of filaments as most outstanding structural aspect of the Cosmic Web (see Fig. 20).

4.10 Nodes of the Cosmic Web: Peak Patches

Clusters represent the rare events in the cosmic matter distribution. In the above we have established that they are the ultimate source for the anisotropic contraction of filaments and form the nodes that weave the cosmic web throughout the Universe.

The study of local one-point shear constraints has lead to the conclusion that filaments are indeed the naturally dominant structural feature in the cosmic matter distribution. The remarkable size of the filaments is not, however,

"compressional" tidal component T_c (for which $T_c < 0.0$) the resulting force field will lead to contraction, pulling together the matter currents. The "dilational" (or "stretching") tidal component T_d, on the other hand, represents the direction along which matter currents tend to get stretched as $T_d > 0$. Note that within a plane, cutting through the 3-D tidal "ellipsoid", the tidal field can consist of two compressional components, two dilational ones or – the most frequently encountered situation – of one dilational and one compressional component.

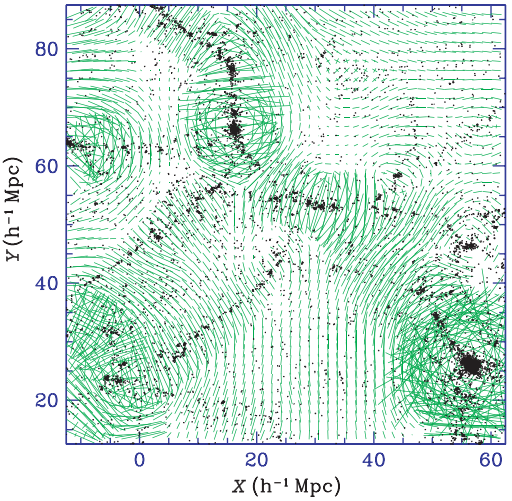

Fig. 20. The relation between the *cosmic web*, the clusters at the nodes in this network and the corresponding compressional tidal field pattern. It shows the matter distribution at the present cosmic epoch, along with the (compressional component) tidal field bars in a slice through a simulation box containing a realization of cosmic structure formed in an open, $\Omega_o = 0.3$, Universe for a CDM structure formation scenario (scale: $R_G = 2\,h^{-1}\,Mpc$). The frame shows structure in a $5\,h^{-1}\,Mpc$ thin central slice, on which the related tidal bar configuration is superimposed. The matter distribution, displaying a pronounced weblike geometry, is clearly intimately linked with a characteristic coherent compressional tidal bar pattern. From: van de Weygaert [83]

derivable from constraints at a given single point. To learn more about the strength, structure and connections of the weblike features we need to investigate their dependence on the location, nature and structure of clusters. For this we need to turn to correlations constrained by at least two rare peak-patches. In order to fully grasp their impact on the overall morphology of the cosmic web we first need to delve into their internal structure.

Clusters at any cosmic epoch are the product of a hierarchical buildup of structure in and around the primordial protocluster, peaks in the primordial mass distribution. In Sect. 3.3 we have discussed in some detail how the anisotropic nature of collapse of (sub)clumps can be included by means of a *moving collapse barrier* in a local extended Press–Schechter description of hierarchical evolution. A more physical image would also try to take into account the matter distribution in and around the primordial peak. This is achieved by the *peak patch* formalism of Bond & Myers [17].

The *peak-patch* formalism exploits the full potential of the peaks formalism [6] by using adaptive spatial information on both small and large scales to construct the hierarchical evolution of collapsing protocluster *peak patches*.

The entire patch moves with a bulk peculiar velocity and is acted upon by external tidal fields, determined by long-wavelength components of the density field.

Peak Patch: Hierarchical & Anisotropic Collapse

The formation of a cluster around an overdensity is approximated as the combination of the linear evolution of a smooth large-scale background field and the coupled nonlinear evolution of the mass element itself, and its substructure. Clusters are identified with the peaks in the primordial Gaussian field on an appropriately large smoothing scale R_G. This scale is determined by filtering the field around a particular peak's location over a range of radii. By means of the ellipsoidal collapse model, including the influence of the external tidal field, the collapse time of the ellipsoidal configuration is determined. At any one cosmic epoch the peak's scale R_{pk} is identified with the largest scale $R_{\rm b}$ on which, according to the homogeneous ellipsoidal model, it has collapsed along all three dimensions.

The mass of the peak is

$$M_{pk} \;=\; \frac{4}{3}\pi\rho_{\rm u}a^3\,R_{pk}^3\,. \tag{79}$$

Because the formalism works within the spatial mass distribution itself it allows the identification and dissection of overlapping (collapsed) peak patches. Usually this concerns peaks of a different scale. Small-scale peaks may be absorbed/merged with larger peaks with which they largely overlap (*half-exclusions*). If they only partially overlap, with their centers outside each others range, one may seek to define a proper prescription to divide up the corresponding mass (*binary exclusion/reduction*). The resulting mass spectrum of clumps adheres closely to the predictions of the extended Press–Schechter formalism and to the results of N-body simulations.

A major virtue of the peak-patch formalism is that the spatial distribution of the patches may be followed in time. Upon having identified the patches at their original Lagrangian location, they are subsequently displaced towards their Eulerian position (most conveniently by means of the Zel'dovich formalism). A typical result is shown in Fig. 21 (from Platen et al. [64]), a nice illustration of how narrowly collapsed peaks trace the cosmic web.

Anatomy of a Peak

Following the differentiation between nonlinearly evolving short wavelength contributions $\delta_{\rm f}(\mathbf{x})$ and linearly evolving long-wavelength contributions $\delta_{\rm b}(\mathbf{x})$ (see (42)), we can distinguish three contributions to a peak's structure and dynamics,

$$\begin{aligned}\delta(\mathbf{x}) \;&=\; \bar{\delta}_{\rm b}(\mathbf{x}) \;+\; F_{\rm b}(\mathbf{x}) \;+\; F_{\rm f}(\mathbf{x}) \\ &=\; \bar{\delta}_{\rm b}(\mathbf{x}) \;+\; F_{\rm b}(\mathbf{x}) \;+\; \delta_{\rm f}(\mathbf{x})\end{aligned} \tag{80}$$

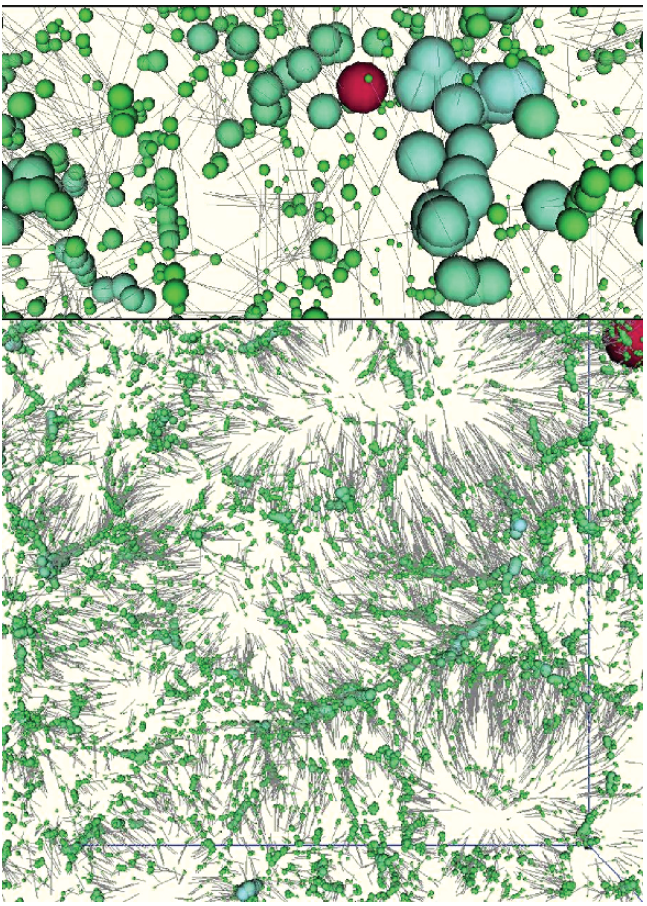

Fig. 21. The distribution of peak patches for a realization of a SCDM density field in a $100\,\mathrm{h}^{-1}$ Mpc box. The lefthand image is a slice through the 3-D matter distribution. The blobs are collapsed peaks, their size related to their spatial extent/mass. Each patch is moved from its Lagrangian position by means of the Zel'dovich formalism. The gray edges are the paths followed by each of the patches. The bottom insert zooms in on one of the regions, offering a more distinct impression of the size of each of the patches. Image courtesy of Erwin Platen

One concerns the *mean field* structure $\bar{\delta}_{\mathrm{b}}(\mathbf{x})$ of the cluster peak specified on a scale R_b and formally corresponds to the ensemble average of all peaks with the specified properties. Because the peak is embedded within a fluctuating (large-scale) field, there is also a *residual* fluctuating large-scale contribution $F_{\mathrm{b}}(\mathbf{x})$. In and around the peak the latter is heavily affected by the peak's presence in that it is hardly existent or at least extremely quiescent in its neighbourhood. The internal substructure of the peak patch mainly consists of the short wavelength contribution $\delta_{\mathrm{f}}(\mathbf{x})$. The latter is hardly affected by the

presence of the peak. While formally constrained by the peak's presence, the resulting *residual* contribution $F_{\rm f}(\mathbf{x})$ is mostly a pure unconstrained Gaussian random field.

The individual components contributing to the total density field around a primordial cluster peak are shown in Fig. 22 (from Bond & Myers [17]). The structure of the peak on a is shown by means of density field contours and peculiar velocity field vectors. The peak's structure was specified on a Gaussian scale of $R_G = 5\,{\rm h}^{-1}\,{\rm Mpc}$. The solid circle indicates the corresponding peak scale $R_{pk} = 10\,{\rm h}^{-1}\,{\rm Mpc}$. The overall triaxial structure of the peak is determined by the bakcground mean field shown in the top lefthand panel. The

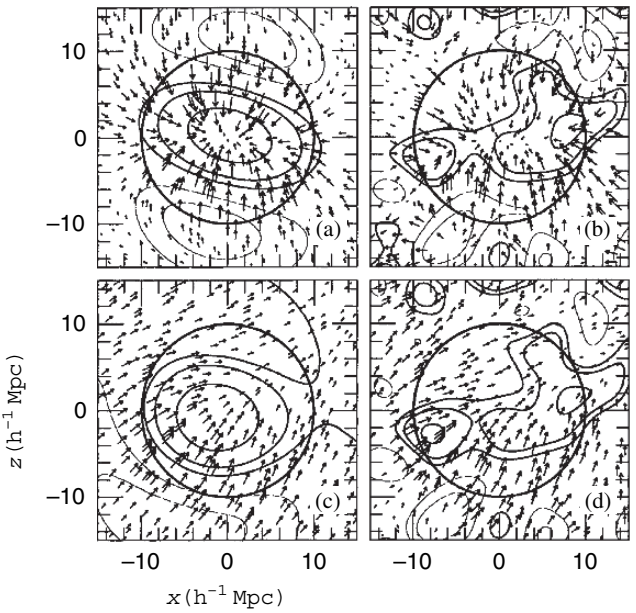

Fig. 22. The individual contributions to the structure (*density field contours*) and peculiar velocity field (*arrows*) in and around a density peak. The first three panels show the (**a**) large-scale mean field $\delta_{\rm b}$, (**b**) the large-scale variance field $F_{\rm b}$, which is extremely quiescent in the neighbourhood of a peak, and (**c**) the small-scale field $\delta_{\rm f}$ responsible for subclumps within the medium. Adding them altogether produces (**d**) the total field around the density peak. In (**a**) and (**b**) the contours increase by factors of 2 from the minimum contour at $f_c/2$, where $f_c = 1.69$ is the critical contour for spherical tophat collapse. The displacement arrows are scaled for appearance, and only one in 12 are sampled. Panels (**c**) and (**d**) start at the f_c contour level for positive densities and at $2f_c$ for negative ones. The peak was constrained to have $\nu_{\rm pk} = 2.45$, $e_{\rm v,pk} = 0.14$ and $v_{\rm 1,pk} = 0.46\sigma_v$ on a Gaussian smoothing scale of $R_G = 5\,{\rm h}^{-1}\,{\rm Mpc}$. The circle at at $10\,{\rm h}^{-1}\,{\rm Mpc}$ is the average $R_{\rm pk}$ associated with Gaussian peaks at this filter scale. From: Bond & Myers [17]. Reproduced with permission of AAS

velocity vectors delineate the expected shear flow around the peak. Because the specified peak constraints essentially fully specify the structure of the peak on the smoothing scale the background variance field $F_{\rm b}(\mathbf{x})$ is extremely quiescent (top righthand frame). The small-scale residual field (bottom lefthand frame) includes two subclumps, one of them rather extended. Adding all components together yields the total structure in and around the peak (bottom righthand frame).

The small-scale structure in and around the peak may vary considerably from one realization to another even though the cluster's large scale structure remains the same. The global history and fate of the peak, however, are largely specified by the large-scale anisotropic tidal shear and bulk flow.

4.11 Molecular View of the Cosmic Web

In the observed galaxy distribution "superclusters" are often filamentary cluster-cluster bridges and the most pronounced ones will be found between clusters of galaxies that are close together and which are aligned with each other. Very pronounced galaxy filaments of which the Pisces-Perseus supercluster chain is a telling example are almost inescapably tied in with a high concentration of rich galaxy clusters. The Cosmic Web theory expands the observation of the intimate link between clusters and filaments, described in some detail in Sect. 4.9, to a complete framework for weaving the cosmic web in between the clusters in the cosmic matter distribution.

The Cosmic Web Theory

In the language of the crf formalism discussed in Sect. 4.8 the filamentary bridges in between two peak patches should be regarded as "correlation" bridges. The implied constraint correlation function (or mean field) $\xi_i(\mathbf{r}) = \langle\delta|2{\rm pks}\rangle$ defines a protofilament, along the lines seen in Fig. 18. These correlation bridges will be stronger and more coherent as clusters are nearer than the mean cluster separation. Because clusters are strongly clusters and statistically biased [7, 40] there are many cluster pairs evoking strong filamtary bridges.

The filament bridge will break if the separation of the clusters is too large, due to diminishing amplitude of the correlation $\xi_i(\mathbf{r}) = \langle\delta|2{\rm pks}\rangle$. Such clusters will be isolated from each other, unless there is a cluster in between to which both have extended their filamentary bridges. As a result, the typical scale of a segment of the filamentary network in a CDM type scenario will be in the order of $\sim 30\,{\rm h}^{-1}\,{\rm Mpc}$.

This brings us to the aspect of establishing the weblike network characterizing the observed galaxy distribution and matter distribution in computer simulations. Consider laying down the rare cluster peaks in the cosmic matter distribution according to the clustering pattern of peak-patches which become clusters when they evolve dynamically. The correlation bridges arche

from cluster to cluster in much of the domain, and tehse dynamically evolve to filaments, creating the network and containing the bulk of the mass.

The order in which the physically significant structures arise is basically the inverse of that in the classical pancake picture: first, high-density peaks, then filaments between them and, possibly, afterwards the walls. The latter should be seen as the rest of the mass between the voids.

Outlining the Web

Figure 23 convincingly demonstrates the viability of the cosmic web theory by illustrating the excellent reconstruction of the primordial density field implied by the presence of a set of selected protocluster peaks. The figure concerns a CDM scenario realization within a comoving region of $50\,\mathrm{h}^{-1}\,\mathrm{Mpc}$ (the same box as in Fig. 16). Within this volume the peak patches are identified and rank-ordered in mass.

Of each peak patch the value of the overdensity, the shear tensor $\mathcal{E}_{b,ij}$ and displacement $\mathbf{s}_b$ are measured, at their location $\mathbf{r}_{pk}$ and averaged over the peak-patch size R_{pk}. In addition to the in total $9N$ constraints for N peak patches, the extremum requirement of a vanishing density gradient $\nabla\delta_b = 0$ at $\mathbf{r}_{pk}$ adds a further $3N$ constraints. On the basis of the selection of the N rarest and most massive peak patches the mean (primordial) field realization is determined following the constrained field formalism outlined in Sect. 4.8. The $12N$ peak constraints and the locations of the N peaks result in a mean initial field $\langle\delta_L|N\mathrm{peaks}\rangle$ (76).

We compare the mean field realizations implied by the 5 most massive peak patches, that by the 10 most massive peaks and for the 20 most peaks. In the boxes in the lefthand column of Fig. 23 we have indicated their locations by black ellipsoids of overall size proportional to R_{pk} and shape defined by the shear tensor orientation, with the shortest axis corresponding to the highest shear eigenvalue. The corresponding mean field density field is represented by isodensity contours at a level $\delta_L = 1\sigma_\rho$, where δ_L is smoothed on a scale of $3.5\,\mathrm{h}^{-1}\,\mathrm{Mpc}$. The righthand frames show the Zel'dovich maps of these smoothed initial conditions.

A comparison with Fig. 16 shows the excellent reconstruction obtained by adding in the 20 most massive peaks. Also we see that the reconstruction improves continuously as more and more peaks are added. Some strong bridges seen in the 20 peak reconstruction $\langle\delta_L|20\mathrm{pks}\rangle$ are not as evident in the $\langle\delta_L|10\mathrm{pks}\rangle$ field, although they emerge at lower thresholds.

Web Bridges: Shear, Distance and Orientation

The observations discussed above show that a list of rank-ordered peak-patches is a powerful way to maximally compress the information stored in the initial conditions. They also show what is essential for defining structures on the basis of a modest set of local measurements. That the specification

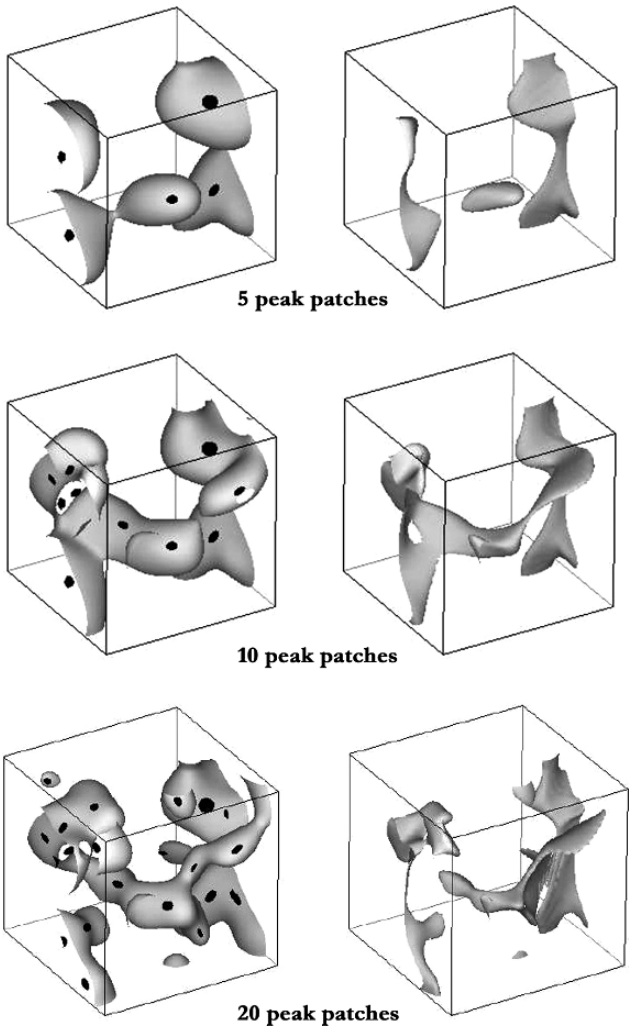

Fig. 23. Building the Cosmic Web with clusters. How adding clusters gradually defines the details of the Cosmic Web. (Mean) Constrained density field reconstructions $\langle \delta_L | Npeaks \rangle$ on the basis of the N most massive cluster peaks (patches) in a CDM model of cosmic structure formation. The volume is a $(50\,\mathrm{h}^{-1}\,\mathrm{Mpc})^3$ box with periodic boundary conditions. The lefthand column frames contain the initial linear CDM overdensity field $\delta_L(\mathbf{r})$, smoothed on a Gaussian scale $R_G = 3.5\,\mathrm{h}^{-1}\,\mathrm{Mpc}$ with (iso)density threshold level $\delta_L = 1\sigma_\rho$, with $\sigma_\rho = 0.65$, the level at which δ_L percolates. The location, size and shape of the cluster patches are indicated by means of the black ellipsoids, whose size is proportional to the peak scale R_{pk} and orientation defined by the shear tensor orientation. The righthand column contain the corresponding Zel'dovich map density field δ_Z of the smoothed initial conditions at a contour threshold $\delta_Z = 2$. **Top row:** the constrained field $\langle \delta_L | 5peaks \rangle$ for 5 peaks, $\langle \delta_L | 10peaks \rangle$ for 10 peaks and $\langle \delta_L | 20peaks \rangle$ for 20 peaks. Based on Bond et al. [18]. Reproduced with permission of Nature

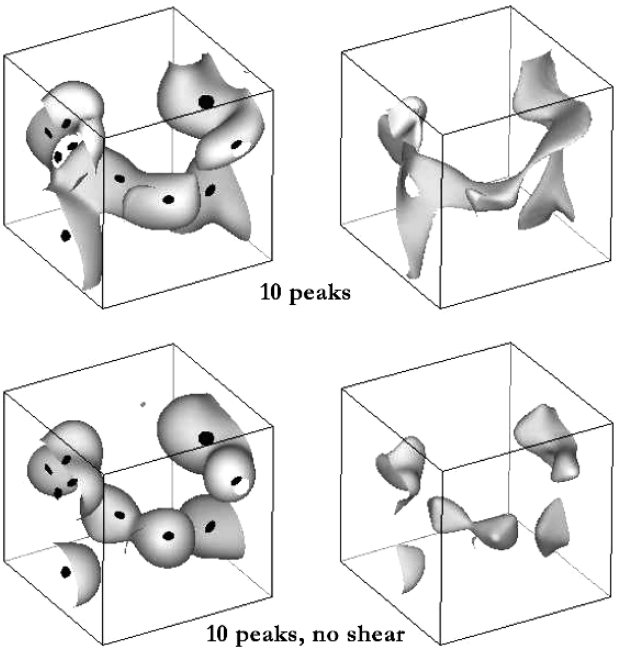

Fig. 24. Cluster Shear and the Cosmic Web. How cluster tidal shear defines the filigree of the Cosmic Web. Comparison between a (mean) cosmic density field generated by the 10 most massive cluster peaks with shear constraints (**top show**) and without shear constraints (**bottom row**), for a CDM simulation in a $(50\,\mathrm{h}^{-1}\,\mathrm{Mpc})^3$ box with periodic boundary conditions. Left row: isodensity contours of the linear CDM overdensity field $\delta_L(\mathbf{r})$, smoothed on a Gaussian scale $R_G = 3.5\,\mathrm{h}^{-1}\,\mathrm{Mpc}$ with (iso)density threshold level $\delta_L = 1\sigma_\rho$, with $\sigma_\rho = 0.65$. The location, size and shape of the cluster patches are indicated by means of the black ellipsoids, whose size is proportional to the peak scale R_{pk} and orinetation defined by the shear tensor orientation. The righthand column contain the corresponding Zel'dovich map density field δ_Z of the smoothed initial conditions at a contour threshold $\delta_Z = 2$. Both initial density field and Zel'dovich map for the non-shear constraint situation (**bottom row**) do have a more bloblike character, and does hardly contain the matter bridges characterizing the Cosmic Web. Based on Bond et al. [18]. Reproduced with permission of Nature

of the tidal shear at the peak patches is of fundamental importance for the succesfull reconstruction of the Cosmic Web may be appreciated from Figs. 23 and 24. By discarding the tidal shear measurements at the peak patches and only taking into account their overdensity and velocity the implied mean field loses its spatial coherence. Instead of being marked by strong filamentary bridges the mean field will have a more patchy character. It demonstrates our earlier arguments that the tidal shear evoked by the inhomogeneous cosmic mass distribution is of crucial and fundamental importance in defining the Cosmic Web.

The strength and the coherence of the correlation bridges depend strongly on the mutual distance of the clusters and their alignment. The strongest filaments are between close peaks whose tidal tensors are nearly aligned. This may be inferred from the illustration of the 2-point correlation function in Fig. 25: a binary molecule image with oriented peak-patches as the atoms. The initial conditions in this figure have been smoothed and Zel'dovich mapped, producing a telling illustration of the *molecular* picture of large scale structure.

The bridge between two clusters will gradually weaken as the separation between the clusters increases. Strong filaments extend only over a few Lagrangian radii of the peaks they connect. It is in the nonlinear mass distribution that they occur so visually impressive because the peaks have collapsed by about a factor 5 in radius, leaving the long bridge between them, which themselves have also gained more contrast because of the decreases in its transverse dimension.

Another important factor influencing the coherence and strength of the connecting filamentary bridges are the mutual alignments between the shear tensors of the cluster peaks. When we vary the shear orientation from perfect alignment towards misalignment the strong correlation bridge between two clusters will weaken accordingly. The top two panels of Fig. 25 show the difference as two peaks, of equal mass and orientation, are oriented differently. In the lefthand panel they are perfectly aligned, evoking a strong filamentary bridge in between them. When the same clusters are somewhat misaligned, each by $\pm 30^\circ$ with respect to their connecting axis, the bridge severely weakens. The bridge would break at an isodensity level of $\delta_l = 1$, althougn it would remain connected at a lower level, for a misalignment of $\approx \pm 45^\circ$. In the most extreme situation of a misalignment by $\pm 90^\circ$ the bridge would be fully broken, no filament would have emerged between the two clusters. The reason for the strong filaments between aligned peaks is that the high degree of constructive interference of the density waves required to make the rare peak-patches, and to preferentially orient them along their connecting axis leads to a slower decoherence along that axis than along the other axes. This in turn corresponds to a higher density.

Important for the overall weblike structure in the matter distribution is the fact that there is a distinct tendency of clusters to be aligned with each other. The alignment of the orientations of galaxy haloes and clusters with larger scale structures such as clusters, filaments and superclusters have been the subject of numerous studies (see e.g. Binggeli [12], Bond [13], Rhee et al. [68], Plionis & Basilakos [65], Basilakos et al. [8], Trujillo et al. [82], Aragón-Calvo et al. [2], Lee & Evrard [50], Park & Lee [60], Lee et al. [52]). The peak-patch theory [17] offers a natural explanation for these alignments by showing that it is statistically likely that, given a specific orientation of the shear tensor for a cluster peak, neighbouring cluster peaks will be aligned preferentially along its axis and have shear tensors aligned with it.

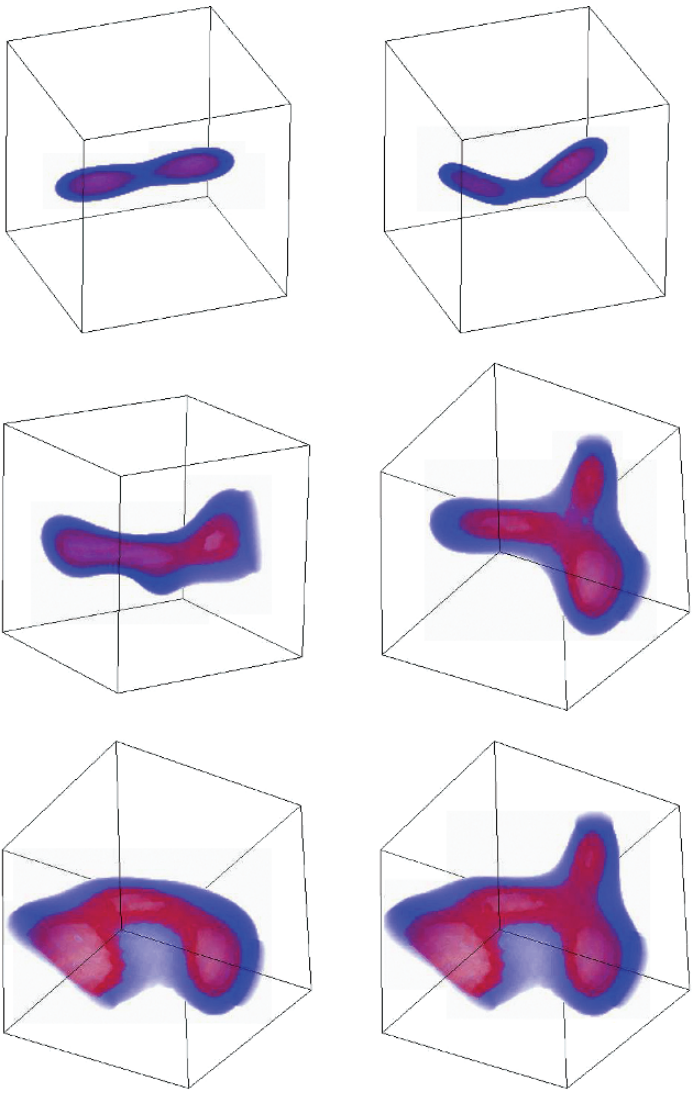

Fig. 25. The molecular picture of large scale structure: "bonds" bridging clusters. Shown are isodensity contours of the Zel'dovich map of the smoothed initial density field. The upper panels show a two-point mean (constrained) field $\langle \delta_L | 2peaks \rangle$ constrained by two oriented clusters separated by $40\,\mathrm{h}^{-1}$ Mpc. Left one is fully aligned, the right pair is partially aligned. The next four panels show three-point (**middle row**) and four-point mean fields for different peak-patch orientations taken from the simulation. Notice the lower density contrast webbing between the filaments. From Bond et al. [19]

Walls and Voids

Upon expanding our inspection in Fig. 25 from 2-peak correlations to three-point and four-point mean fields we see the emergence of low density contrast webbing between the filaments, membrane-like sheets. Stronger membranes will be seen in the regions between the filaments when a number of clusters is close together. Although these are sheetlike structures they are not the classical pancakes. In the molecular view of cosmic structure formation the walls are a mere secondary product.

Voids also do play a significant role in the cosmic web. The formalism is similar, be it reversed, when concentrating on the voids. Void patch constraints create high mean field regions in between them, just where less rare peak patches reside. However, using voids are not as precise a way to get the filamentary structure evoked by the peaks. An upcoming study (Platen et al. [64]) adresses their role and structure in considerably more detail.

Cosmic Scenario

Overall, it is the highly clustered and mutually aligned nature of the cluster distribution which ascertains the salient and coherent weblike nature of the cosmic matter distribution. In turn, this suggests a dependence of the morphology and structure of the cosmic web on the cosmological scenario.

Its pattern and prominence does indeed depend upon the shape of the primordial power spectrum, in particular on the power spectrum index $n(k) = \mathrm{d}\ln P(k)/\mathrm{d}\ln k$. The examples which are shown in the figures concern a CDM spectrum with $n_{\mathrm{eff}} \approx -1.2$ on cluster scales. When the spectrum is steepened clusters become less clustered and the coherence of the web is lost. Although some filaments will remain they will be weaker and shorter. On the other hand, when we flatten the spectrum to $n(k) < -2$, the clusters become more clustered, so that the coherence is more pronounced and the filaments are both strengthened and widened.

4.12 Hierarchical Filament Assembly

In the previous sections we have delved in great depth into the nature and origin of filamentary and sheetlike features in the cosmic web. We have not yet paid a lot of attention to their hierarchical development. In the reality of the nonlinear world the collapse and formation of weblike patterns is considerably more complex. Taking the specific example of an emerging filament, its formation will involve the gradual assembly of small-scale filaments and virialized low mass clumps into a coherent elongated feature.

Figure 26 gives an impression of the intricacies of filament formation Aragón-Calvo [1]. It involves a ΛCDM scenario. The initial configuration consists of a myriad of small-scale filaments, with a large scatter in orientation. As time proceeds these small filaments start to merge into larger filaments,

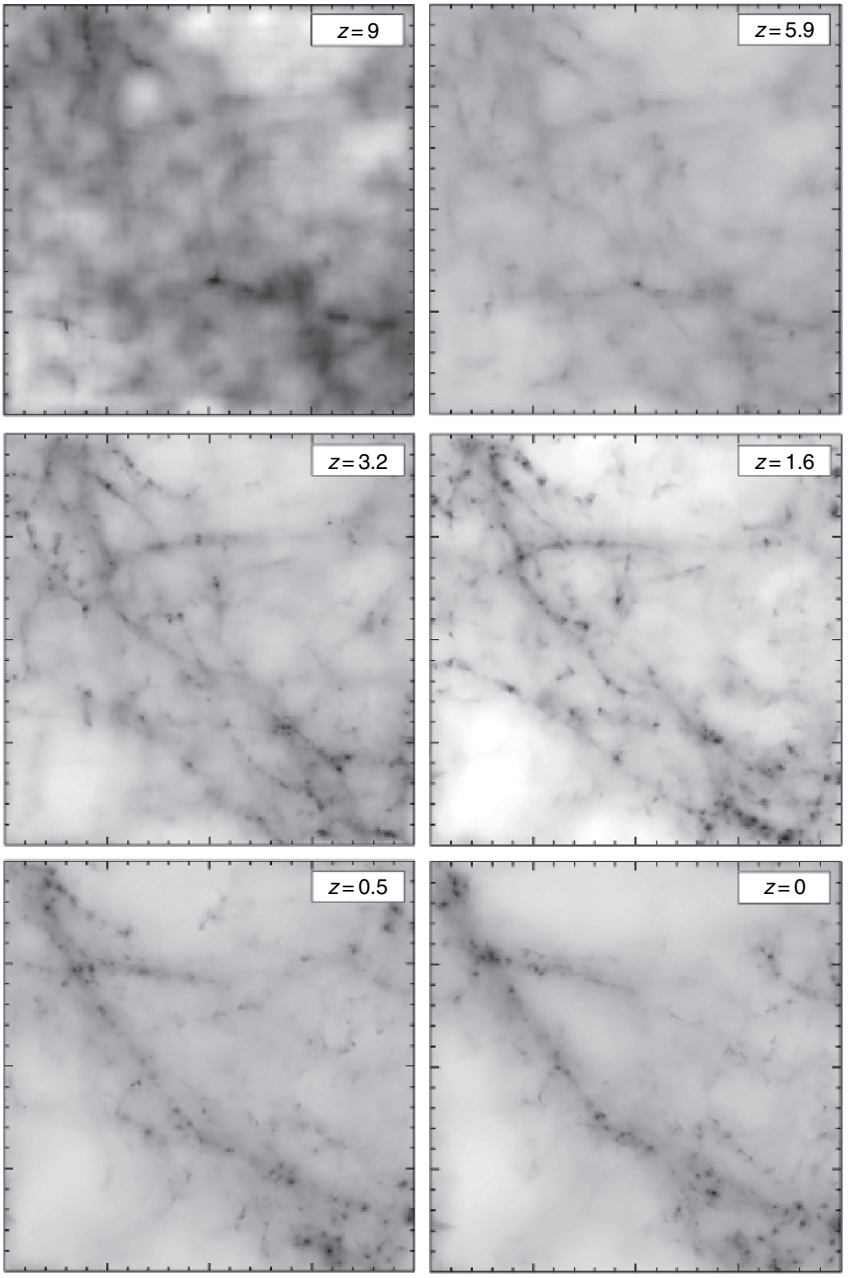

Fig. 26. The hierarchical evolution of weblike features: the formation of a filament in an N-body simulation of structure formation in a LCDM Universe. Following the emergence of small-scale filaments, we observe the gradual merging into ever larger entities, culminating in a large massive and dense filament running along the diagonal of the simulation box. Image courtesy of Miguel Aragón-Calvo

preceded by a gradual change of orientation along that of the gradually unfolding large-scale elongated mass concentration running along the diagonal of the box. Finally, all structure ends up in the massive filamentary feature that emerged out of the initially merely faintly visible large-scale overdensity. The figure not only shows the hierarchical character of the process, but also the dominant tidal influence of the large-scale filament which first appears to orient substructures along its main axis before gradually absorbing them. It illustrates the tendency of matter to contract into a sharp filamentary network already defined in the primordial tidal shear field.

The morphology of the emerging filaments strongly depend on the generalized power spectrum slope $n(k)$ at the corresponding mass scale (also see Sect. 4.11). For high values $n \approx -0.5$ – i.e. for subgalactic scales within the ΛCDM scenario – a rather grainy feature will emerge. Many small scale clumps will have fully collapsed and virialized before they get absorbed into the larger contracting filament. In a scenario with $n(k) = -2$, on the other hand, the contracting filament will be collapsing while the small scale objects within its realm may not yet have fully settled. Often these have not yet even fully virialized and may still reside in a stage with a pronounced anisotropic geometry. Such scenarios will produce a *coherent large-scale filaments* in which the internall small-scale structure will not have a pronounced appearance. Most dramatic will be the situation for $n(k) = -3$, the asymptotic situation in which fluctuations over the full range of scale will undergo contraction and collapse at the same time.

The morphology of filaments, as well as sheets, will also be influenced by an additional effect, that of the *diffusion* of relative dynamical timescales between different mass scales. Anisotropic collapse will involve a speeding up of the one-dimensional collapse of an object, and even often a faster collapse along the medium axis as the object contracts into a filament, but a considerably slower formation time in terms of full three-dimensional collapse and virialization. This will bring the formation time of halos closer to that of the embedding elongated filaments. As a result, the latter will appear to be more coherent than a simple hierarchical analysis on the basis of clump formation would imply.

Finally, the morphology of filaments will also be considerably affected by nonlinear effects. The (extended) Press–Schechter type descriptions involve highly idealized local approximations. They discard the nonlinear interactions between the features forming at different scales.

One particular aspect is that of the consequence of alignments between peaks and the surroundings. The primordial alignments get significantly amplified by the subsequent infall of clumps from the surroundings. A few nonlinear effects may be identified. The filaments act like transport channels of the emerging cosmic web: matter and clumps of matter migrate along the axis of filaments towards highly compact clusters at the nodes of the web. The morphology and nature of filaments – strong, dominating, large and coherent or having the appearance of short, weak, and erratic hairlike extensions

connected to nearby peaks – will be of decisive influence over aspects like the angular distribution of clumps which fall into a cluster. van Haarlem & van de Weygaert [86] found that clusters appear to orient themselves towards the direction along which the last substantial clumps fell in. The exclusive and continuous infall of clumps along the spine of dominating filament will therefore induce a strong alignment of cluster orientation, its substructure and the surroundings.

4.13 Anisotropic Excursions

Some aspects of the hierarchical assembly of filaments may be understood within the context of the *excursion set* formalism described above (Sect. 3.4). Shen et al. [72] did seek to extend the excursion formalism to filamentary and planar structures by defining critical density thresholds for the collapse of filaments and walls. In this they invoked the *moving barrier* description for nonspherical collapse of ellipsoidal halos that was introduced by Sheth et al. [75] (see (32)).

Their description invokes the homogeneous ellipsoid model to obtain estimates for the collapse times of walls and filaments. In addition to the full three-dimensional ellipsoidal collapse of halos this involves the specification of collapse times and barriers for the one-dimensional collapse of sheets and two-dimensional filaments. Collapse along the shortest axis of an ellipsoid proceeds more rapidly than the equivalent spherical collapse [38, 88]. The corresponding moving barrier for the formation of a sheet does reflect this in involving the lowest density threshold values (see Fig. 27). The threshold would decrease towards smaller masses, implying the rapid formation of low mass sheetlike objects. By contrast the barrier for filament formation would almost be constant over a sizeable range of mass while the barrier for full three-dimensional collapse does reflect the strong influence of tidal influences for small mass halos: with respect to their higher mass peers they form relatively late (see Fig. 27).

$$
\begin{aligned}
f_{ec,w}(\sigma,z) &\approx f_{sc}(z)\left\{1-0.56\left[\frac{\sigma^2(M)}{f_{sc}^2(z)}\right]^{0.55}\right\} \\
f_{ec,f}(\sigma,z) &\approx f_{sc}(z)\left\{1-0.012\left[\frac{\sigma^2(M)}{f_{sc}^2(z)}\right]^{0.28}\right\} \approx f_{sc}(z)\,, \\
f_{ec,f}(\sigma,z) &\approx f_{sc}(z)\left\{1+0.45\left[\frac{\sigma^2(M)}{f_{sc}^2(z)}\right]^{0.61}\right\}
\end{aligned}
\tag{81}
$$

Although this description may provide a reasonable impression of the hierarchical buildup of the cosmic web, it almost certainly involves a strong

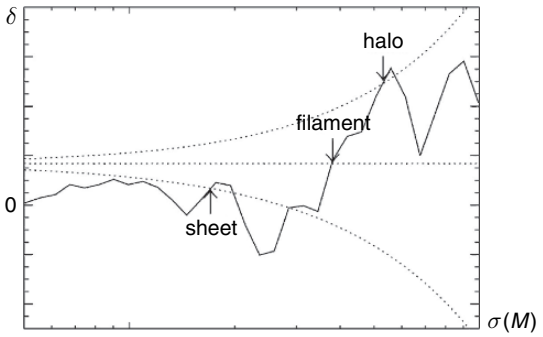

Fig. 27. Example of an excursion random walk (*solid curve*) crossing the barriers (*dotted curves*) associated with sheets, filaments and haloes (bottom to top, see (82)). Plotted is the density perturbation $\delta(M)$ on a mass scale M versus the corresponding $\sigma(M)$ (recall that $\sigma(M)$ is a decreasing function of mass M). The fraction of walks that first cross the lowest (sheet) barrier at $\sigma(M_s)$, then first cross the filament barrier at $\sigma(M_f)$ and finally cross the highest (halo) barrier at $\sigma(M_h)$ represents the mass fraction in halos of mass M_h that are embedded in filaments of mass $M_f > M_h$, which themselves populate sheets of mass $M_s > M_f$. The precise barrier shapes depend on the collapse model. From Shen et al. 2006. Reproduced with permission of AAS

oversimplification. The implicit local description of the excursion set formalism may break down for features whose collapse is thoroughly influenced by the surrounding matter distribution, so strongly emphasized by the *Cosmic Web*. Also the strong nonlinear effects that play a role in the shaping of filamentary features van Haarlem & van de Weygaert [86] may not be sufficiently included in this description. Finally, recent work has shown that a definition of filaments on the basis of density arguments is hazardous: filaments have a considerable range of densities, at least in the present day universe Aragón-Calvo [1], Aragón-Calvo et al. [3], Hahn et al. [31]. An analytical framework that implicitly includes nonlocal effects will offer a better understanding of the hierarchical formation of filaments, bringing us back to the *peakpatch* formalism [17].

4.14 Filaments Versus Walls

In N-body simulations as well as in galaxy redshift distributions it are in particular the filaments which stand out as the most prominent feature of the *Cosmic Web*. It even remains unclear whether *walls* are even present at all. Some argue that once nonlinear clustering sets in the stage in which walls form is of a very short duration or does not occur at all: true collapse would proceed along filamentary structures [11, 36, 70]. Indeed, it may be argued that in the primordial density field overdense regions subject to tidal shear constraints are more filamentary than sheetlike, and become even more so in the

quasi-linear regime [18]. There is also a practical problem in identifying them: walls have a considerably lower surface density than filaments. This is exacerbated by the lack of available objective feature detection techniques. Very recent, the analysis of an N-body simulation by means of the new Multiscale Morphology Filter technique did manage to identify walls in abundance [2]. Another indication is that the dissipative gaseous matter within the cosmic web partially aggregates in walls with low overdensities [41]. This argues for the presence of moderate potential wells tied in with dark matter walls.

5 Conclusion: Clusters and the Cosmic Web

In these notes we have reviewed the theoretical framework for the formation of the Cosmic Web in hierarchical scenarios of structure formation. Particular attention was given to the crucial role of clusters within defining the weblike network. They are the main source for the tidal shear field responsible for the spatial outline and dynamical evolution of the prominent filaments and their less pronounced peers, sheetlike membranes.

We wish to conclude our exposé on the connection between the Cosmic Web and the spatial distribution with the quote from Bond & Myers [17] summarizing the essence of what the intrinsic role and identity of clusters is:

> "flowing peak patches at which grand constructive interferences in density and velocity waves mark out the sites of collapse. ... radiating outward from the peak-patch core are filaments and sheets that too are rare. The structure may finally fade into the root-mean-square fluctuations in the medium as coherence in the phases fades into randomness. Or the structure may blend into another peak patch, for rare constructive interferences tend to be clustered."

6 Acknowledgments

We wish to thank Manolis Plionis and Omar López-Cruz for their invitation and the wonderful weeks in Mexico, and for their almost infinite patience regarding our shifting deadlines. RvdW is most grateful to the hospitality of the Canadian Institute for Astrophysics, where we commenced the project leading to these notes. Both authors thank Max-Planck-Institut für Astrophysik in Garching for providing the hospitality and facilities allowing the completion of these lecture notes. In particular we are indebted to Jacqueline van Gorkom, Hans Böhringer and George Rhee. Without their encouragement and the more than helpful assistance and understanding of Sonja Japenga of Springer Verlag we would not have managed to bring these notes to completion. To them we owe a major share of our gratitude ! RvdW is grateful to

Miguel Aragón-Calvo for his permission to use and manipulate various figures from his Ph.D. thesis. He also acknowledges him and Erwin Platen for many inspiring discussions and their contributions towards obtaining insight into the evolution of the Cosmic Web. Most fondly we wish to thank Bernard Jones, for his enthusiastic and crucial support and inspiration, the many original ideas over the years and for his support in completing this manuscript hours past midnight ...

References

1. Aragón-Calvo, M.A.: Morphology and dynamics of the cosmic web. Ph.D. thesis, Groningen University (2007)
2. Aragón-Calvo, M.A., Jones, B.J.T., van de Weygaert, R., van der Hulst, J.M.: Astrophys. J. **655**, L5 (2007)
3. Aragón-Calvo, M.A., Jones, B.J.T., van de Weygaert, R., van der Hulst, J.M.: Mon. Not. R. Astron. Soc., subm. (2007)
4. Audit, E., Teyssier, R., Alimi, J.-M.: Astron. Astrophys. **325**, 439 (1997)
5. Balbus, S.A., Hawley, J.F.: Revs. Mod. Phys. **70**, 1 (1998)
6. Bardeen, J.M., Bond, J.R., Kaiser, N., Szalay, A.S.: Astrophys. J. **304**, 15 (1986)
7. Barkana, R., Loeb, A.: Phys. Rep. **349**, 125 (2001)
8. Basilakos, S., Plionis, M., Yepes, G., Gottlöber, S., Turchaninov, V.: Mon. Not. R. Astron. Soc. **365**, 539 (2006)
9. Bennett, C.L., et al.: Astrophys. J. Suppl. **148**, 1 (2003)
10. Bertschinger, E.: Astrophys. J. **323**, L103 (1987)
11. Bertschinger, E., Jain, B.: Astrophys. J. **431**, 486 (1994)
12. Binggeli, B.: Astron. Astrophys. **107**, 338 (1982)
13. Bond, J.R. Testing Cosmic Fluctuation Spectra. In: Faber, S. (ed.) Nearly Normal Galaxies. Springer, New York, p. 388 (1987)
14. Bond, J.R.: Astrophys. J. preprint (2008)
15. Bond, J.R.: Astrophys. J. preprint (2006)
16. Bond, J.R., Cole, S., Efstathiou, G., Kaiser, N.: Astrophys. J. **379**, 440 (1991)
17. Bond, J.R., Myers, S.T.: Astrophys. J. Suppl. **103**, 1 (1996)
18. Bond, J.R., Kofman, L., Pogosyan, D.Yu.: Nature **380**, 603 (1996)
19. Bond, J.R., Kofman, L., Pogosyan, D.Yu., Wadsley, J.: Theoretical tools for large scale structure. In: Colombi, S., Mellier, Y., (eds.) Wide Field Surveys in Cosmology, 14th IAP meeting. Editions Frontieres, Paris, p. 17 (1998)
20. Bond, J.R., Contaldi, C.R., Kofman, L., Vaudrevange, P.M.: preprint (2008)
21. Bower, R.G.: Mon. Not. R. Astron. Soc. **248**, 332 (1991)
22. Bryan, G.L., Norman, M.L.: Astrophys. J. **495**, 80 (1998)
23. Chandrasekhar, S.: Revs. Mod. Phys. **15**, 1 (1943)
24. Desjacques, V.: Mon. Not. R. Astron. Soc., in press (2008) (`astroph/0707.4670`)
25. Doroshkevich, A.G.: Astrophysics **6**, 320 (1970)
26. Eisenstein, D.J., Loeb, A.: Astrophys. J. **439**, 520 (1995)
27. Eke, V.R., Cole, S., Frenk, C.S.: Mon. Not. R. Astron. Soc. **282**, 263 (1996)
28. Epstein, R.I.: Mon. Not. R. Astron. Soc. **205**, 207 (1983)
29. Freeman, K., Bland-Hawthorn, J.: Ann. Rev. Astron. Astrophys. **40**, 487 (2002)
30. Gunn, J.E., Gott, J.R.: Astrophys. J. **176**, 1 (1972)

31. Hahn, O., Porciani, C., Carollo, M., Dekel, A.: Mon. Not. R. Astron. Soc. **375**, 489 (2007)
32. Hamilton, A.J.S.: Mon. Not. R. Astron. Soc. **322**, 419 (2001)
33. Heath, D.J.: Mon. Not. R. Astron. Soc. **179**, 351 (1977)
34. Helmi, A., White S.D.M.: Mon. Not. R. Astron. Soc. **307**, 495 (1999)
35. Hoffman, Y., Ribak, E.: Astrophys. J. **380**, L5 (1991)
36. Hui, L., Bertschinger, E.: Astrophys. J. **471**, 1 (1996)
37. Icke, V.: Formation of galaxies inside clusters. Ph.D. thesis, Leiden University (1972)
38. Icke, V.: Astron. Astrophys. **27**, 1 (1973)
39. Jones, B.J.T., van de Weygaert, R.: Mon. Not. R. Astron. Soc., to be subm. (2008)
40. Kaiser, N.: Astrophys. J. **284**, 9 (1984)
41. Kang, H., Ryu, D., Cen, R., Song, D.: Astrophys. J. **620**, 21 (2005)
42. Kauffmann, G., White, S.D.M.: Mon. Not. R. Astron. Soc. **261**, 921 (1993)
43. Kitayama, T., Suto, Y.: Astrophys. J. **469**, 480 (1996)
44. Klypin, A., Hoffman, Y., Kravtsov, A., Gottlöber, S.: Astrophys. J. **596**, 19 (2003)
45. Kuo et al.: Astrophys. J. **664**, 687 (2007)
46. Lacey, C., Cole, S.: Mon. Not. R. Astron. Soc. **262**, 627 (1993)
47. Lacey, C., Cole, S.: Mon. Not. R. Astron. Soc. **271**, 676 (1994)
48. Lahav, O., Lilje, P.B., Primack, J.R., Rees, M.: Mon. Not. R. Astron. Soc. **251**, 136 (1991)
49. Lahav, O., Suto, Y.: Living Rev. Relat. **7**, 82 (2004)
50. Lee, J., Evrard, A.E.: Astrophys. J. **657**, 30 (2007)
51. Lee, J., Shandarin, S.F.: Astrophys. J. **500**, 14 (1998)
52. Lee, J., Springel, V., Pen, U-L., Lemson, G.: arXiv0709.1106 (2007)
53. Lin, C.C., Mestel, L., Shu, F.H.: Astrophys. J. **142**, 1431 (1965)
54. Lynden-Bell, D.: Astrophys. J. **139**, 1195 (1964)
55. Mathis, H., White, S.D.M.: Mon. Not. R. Astron. Soc. **337**, 1193 (2002)
56. Monaco, P.: Astrophys. J. **447**, 23 (1995)
57. Monaco, P.: Mon. Not. R. Astron. Soc. **287**, 753 (1997)
58. Monaco, P.: Mon. Not. R. Astron. Soc. **290**, 439 (1997)
59. Neumann, D.M., Lumb, D.H., Pratt, G.W., Briel, U.G.: Astron. Astrophys. **400**, 811 (2003)
60. Park, D., Lee, J.: Astrophys. J. **665**, 96 (2007)
61. Peacock, J.A., Heavens, A.F.: Mon. Not. R. Astron. Soc. **243**, 133 (1990)
62. Peebles, P.J.E.: The Large-Scale Structure of the Universe, Princeton University Press, New York (1980)
63. Percival, W.J.: Astron. Astrophys. **443**, 819 (2005)
64. Platen, E., van de Weygaert, R., Jones, B.J.T.: Mon. Not. R. Astron. Soc., in prep. (2008)
65. Plionis, M., Basilakos, S.: Mon. Not. R. Astron. Soc. **329**, L47 (2002)
66. Pogosyan, D.Yu, Bond, J.R., Kofman, L., Wadsley, J.: Cosmic web: origin and observables. In: Colombi, S., Mellier, Y., (eds.) Wide Field Surveys in Cosmology, 14th IAP meeting. Editions Frontieres, Paris, p. 61 (1998)
67. Press, W.H., Schechter, P.: Astrophys. J. **187**, 425 (1974)
68. Rhee, G., van Haarlem, M., Katgert, P.: Astron. J. **103**, 6 (1991)
69. Romano-Díaz, E., Hoffman, Y., Heller, C., Faltenbacher, A., Jones, D., Shlosman, I.: Astrophys. J. **657**, 56 (2007)

70. Sathyaprakash, B.S., Sahni, V., Shandarin, S.F.: Astrophys. J. **462**, L5 (1996)
71. Schücker, P., Böhringer, H., Reiprich, T.H., Feretti, L.: Astron. Astrophys. **378**, 408 (2001)
72. Shen, J., Abel, T., Mo, H.J., Sheth, R.K.: Astrophys. J. **645**, 783 (2006)
73. Sheth, R.K.: Mon. Not. R. Astron. Soc. **277**, 933 (1995)
74. Sheth, R.K.: Mon. Not. R. Astron. Soc. **300**, 1057 (1998)
75. Sheth, R.K., Mo, H.J., Tormen, G.: Mon. Not. R. Astron. Soc. **323**, 1 (2001)
76. Sheth, R.K., Tormen, G.: Mon. Not. R. Astron. Soc. **329**, 61 (2002)
77. Sheth, R.K., van de Weygaert, R.: Mon. Not. R. Astron. Soc. **350**, 517 (2004)
78. Smoot, G.F., et al.: Astrophys. J. **396**, L1 (1992)
79. Spergel, D.N., Bean, R., Doré, O., Nolta, M.R., Bennett, C.L., Hinshaw, G., Jarosik, N., Komatsu, E., Page, L., Peiris, H.V., Verde, L., Barnes, C., Halpern, M., Hill, R.S., Kogut, A., Limon, M., Meyer, S.S., Odegard, N., Tucker, G.S., Weiland, J.L., Wollack, E., Wright, E.L.: Astrophys. J. Suppl. **170**, 377 (2007)
80. Springel, V., White, S.D.M., Jenkins, A., Frenk, C.S., Yoshida, N., Gao, L., Navarro, J., Thacker, R., Croton, D., Helly, J., Peacock, J.A., Cole, S., Thomas, P., Couchman, H., Evrard, A., Colberg, J.M., Pearce, F.: Nature **435**, 629 (2005)
81. Sugiyama, N.: Astrophys. J. Suppl. **100**, 281 (1995)
82. Trujillo, I.,Carretero, C., Patiri, S.G.: Astrophys. J. **640**, L111 (2006)
83. van de Weygaert, R.: Froth across the universe, dynamics and stochastic geometry of the cosmic foam. In: Plionis, M., Cotsakis, S., (eds.) Modern Theoretical and Observational Cosmology, Proceedings of the 2nd Hellenic Cosmology Meeting. ASSL **276** Kluwer, Dordrecht, pp. 119–272 (2002)
84. van de Weygaert, R., Bertschinger, E.: Mon. Not. R. Astron. Soc. **281**, 84 (1996)
85. van de Weygaert, R., Bond, J.R.: Observations and morphology of the cosmic web. In: Plionis, M., López-Cruz, O., Hughes, D., (eds.) A Pan-Chromatic View of Clusters of Galaxies and the LSS, Springer New York 2008
86. van Haarlem, M., van de Weygaert, R.: Astrophys. J. **418**, 544 (1993)
87. Wadsley, J.W., Bond, J.R.: preprint (1996)
88. White, S.D.M., Silk, J.: Astrophys. J. **231**, 1 (1979)
89. Zaroubi, S., Hoffman, Y., Fisher, K.B., Lahav, O.: Astrophys. J. **449**, 446 (1995)
90. Zel'dovich, Ya.B.: Astron. Astrophys. **5**, 84 (1970)
91. Zentner, A.R.: IJMPD, **16**, 763 (2007)